

Utah State University

DigitalCommons@USU

---

All Graduate Theses and Dissertations

Graduate Studies

---

12-2022

## Serendipity Shape Function for Hybrid Fluid/Kinetic-PIC Simulations

Trevor V. Taylor  
*Utah State University*

Follow this and additional works at: <https://digitalcommons.usu.edu/etd>



Part of the [Physics Commons](#)

---

### Recommended Citation

Taylor, Trevor V., "Serendipity Shape Function for Hybrid Fluid/Kinetic-PIC Simulations" (2022). *All Graduate Theses and Dissertations*. 8652.  
<https://digitalcommons.usu.edu/etd/8652>

This Dissertation is brought to you for free and open access by the Graduate Studies at DigitalCommons@USU. It has been accepted for inclusion in All Graduate Theses and Dissertations by an authorized administrator of DigitalCommons@USU. For more information, please contact [digitalcommons@usu.edu](mailto:digitalcommons@usu.edu).



SERENDIPITY SHAPE FUNCTION FOR HYBRID FLUID/KINETIC-PIC  
SIMULATIONS

by

Trevor V. Taylor

A dissertation submitted in partial fulfillment  
of the requirements for the degree

of

DOCTOR OF PHILOSOPHY

in

Physics

Approved:

---

Eric D. Held, Ph.D.  
Major Professor

---

Jeong-Young Ji, Ph.D.  
Committee Member

---

Joseph V. Koebbe, Ph.D.  
Committee Member

---

Andrew Spencer, Ph.D.  
Committee Member

---

Oscar Varela, Ph.D.  
Committee Member

---

D. Richard Cutler, Ph.D.  
Vice Provost of Graduate Studies

UTAH STATE UNIVERSITY  
Logan, Utah

2022

Copyright © Trevor V. Taylor 2022

All Rights Reserved

## ABSTRACT

Serendipity Shape Function for Hybrid Fluid/Kinetic-PIC Simulations

by

Trevor V. Taylor, Doctor of Philosophy

Utah State University, 2022

Major Professor: Eric D. Held, Ph.D.

Department: Physics

Wave-particle resonances can have significant effects on magnetically confined plasma stability even in cases of small, resonant sub-populations. In tokamak plasmas, long-wavelength modes interact with energetic particles produced by neutral beams, external radio frequency (RF) sources, or fusion-produced alphas. This leads to uncertainty in plasma stability boundaries and enhanced energetic particle transport. Energetic particle closures based on the particle-in-cell (PIC) algorithm have long been used in extended magnetohydrodynamic (MHD) codes to capture this important physics. The extended MHD code, NIMROD, has  $\delta f$ -PIC drift kinetic closure capability. In the linear  $\delta f$ -PIC approach, large samples (1-20 million) of evolving particle weights are pushed along gyro-averaged drift kinetic orbits in the equilibrium fields of NIMROD's MHD fluid model. Particle weights and velocity vectors are then used to construct the energetic particle anisotropic pressure tensor moment which appears in (closes) NIMROD's equation for the center-of-mass flow evolution. In NIMROD's MHD fluid model, Lagrange or Gauss-Lobatto-Legendre polynomials are traditionally used in the spatial discretization. In this work, a reduced set of Lagrange polynomials called Serendipity basis functions are introduced for the  $\delta f$ -PIC approach where nodal locations coincide with each other. This allows for a convenient communication between NIMROD's finite-element fluid and  $\delta f$ -PIC code when pushing the particles. These

Serendipity basis functions are introduced into the  $\delta f$ -PIC drift kinetic approach to increase the accuracy while maintaining the efficiency and keeping the memory footprint small. Up to sixth order of Serendipity basis functions have been implemented in the  $\delta f$ -PIC drift kinetic approach in an attempt to provide more accurate integration of particle trajectories. Such an approach may be vital for accurate integration near the separatrix (the boundary between closed and open magnetic flux surfaces) of a diverted tokamak and for preserving the second-adiabatic invariant. Often, lowest-order bilinear basis functions are used in NIMROD's PIC simulations. Therefore, a careful comparison is made of the performance of Serendipity basis functions against the bilinear and the full 2D Lagrange polynomials. We present the improvements in accuracy, efficiency, and memory reduction when using the Serendipity basis functions. Performance of Serendipity shape functions in test application, sawtooth instability, is also presented.

(146 pages)

## PUBLIC ABSTRACT

## Serendipity Shape Function for Hybrid Fluid/Kinetic-PIC Simulations

Trevor V. Taylor

The Sun in our solar system and stars are capable of generating enormous amounts of energy. The process by which these gaseous, celestial bodies are able to produce such large amounts of energy is called thermonuclear fusion. Fusion happens when particles collide with one another at energy levels high enough to overcome the Coulomb force and then release vast amounts of energy. Plasma, the fourth state of matter, is the natural state of stars. Plasma is an ionized gas that consists of negatively and positively charged particles. Stars, which have immense mass, can confine the plasma through their gravity to sustain the fusion process. Laboratory plasma cannot be confined by gravity. Magnetic fields can be used instead. For the past 70 years, scientists and engineers have been working on harnessing energy from magnetized thermonuclear fusion. Current research contributes to creating a device capable of supporting fusion reactions and producing a clean sustainable energy source.

Sustaining a burning or ignited plasma through fusion reactions is not an easy task. These complex systems can result in many instabilities that limit plasma temperatures and densities and prevent significant thermonuclear fusion from taking place. An important piece of the physics puzzle that either stabilizes or destabilizes the plasma is the interaction of energetic particles with the bulk plasma. This is called the wave-particle interaction or energetic particle interaction with magnetohydrodynamic (MHD) modes. Another example of this would be the solar wind from the sun (energetic particles) interacting with Earth's magnetosphere (bulk plasma).

This thesis focuses on an approach to more accurately and efficiently resolve the energetic particle motions using a computer code. This thesis will also compare two very

different approaches to wave-plasma interaction problem by looking at the grow-rate of an instability that has been used to benchmark several computer codes used by the magnetic fusion energy community.

To my loving wife

Zoe Taylor



## ACKNOWLEDGMENTS

This thesis and my academic development would not have been possible without the help and encouragement of so many. First and foremost, I am grateful for my major professor, Eric Held, for his countless hours of mentoring and encouragement. His concern for me extended beyond academics, allowing me to pursue my goals and ambitions. His selflessness has given me a brighter future, for which I am truly thankful. I am grateful for Jeong-Young Ji who spent hours teaching me physics. He always encouraged me to gain a deep understanding of the fundamentals, which I hope to continue to do throughout my life. I am grateful for the meaningful insights I received from Andrew Spencer. His thoughtful explanations and suggestions helped me grow as a physicist and gave me the encouragement to pursue it even further. I am thankful to Oscar Varela. Taking his class on General Relativity and the help I received from him was insightful and valuable. I am thankful to Joseph Koebbe for the encouragement and valuable advice. This thesis would not have been possible without my committee members.

I appreciate all those who have helped in my academic development and given me valuable advice. I am grateful for Karalee Ransom and Vanessa Chambers who have been there since day one of graduate school. Without their invaluable help, this accomplishment would not have been possible. I am grateful for the Utah State University, Physics department and all those who have contributed to my academic development. I am grateful for the NIMROD team allowing me to use the NIMROD code for my thesis. This project and my Research Assistantship (RA) was supported by the Department of Energy, Office of Fusion Energy Sciences (DOE-OFES). This research used resources of the National Energy Research Scientific Computing Center (NERSC), a U.S. Department of Energy Office of Science User Facility located at Lawrence Berkeley National Laboratory, operated under Contract No. DE-AC02-05CH11231 using NERSC award ERCAP0013952.

I thank my parents for encouraging me in pursuing my dreams and their endless support. They have taught me to pursue my curiosity. I am truly in debt to the selfless

sacrifices they made. Lastly, I am especially grateful to my wife. She brings me joy every day and without her support I would not have achieved my Ph.D.

Trevor V. Taylor

## CONTENTS

	Page
ABSTRACT .....	iii
PUBLIC ABSTRACT .....	v
ACKNOWLEDGMENTS .....	viii
LIST OF FIGURES .....	xii
1 INTRODUCTION .....	1
2 PRELIMINARIES TO PLASMA PHYSICS .....	10
2.1 Lagrangian and Hamiltonian Mechanics .....	10
2.1.1 Lagrangian for a Particle in an Electromagnetic Field .....	11
2.1.2 Hamiltonian for a Particle in Electromagnetic Field .....	13
2.1.3 Non-canonical Mechanics .....	14
2.2 Classical Statistical Mechanics .....	17
2.2.1 Single Particle Distribution Function .....	20
2.2.2 The Vlasov Equation .....	22
2.2.3 The Drift Kinetic Equation .....	25
2.3 Axisymmetric Magnetic Field Configuration .....	27
2.3.1 Axisymmetric Toroidal Magnetic Field .....	29
3 SINGLE PARTICLE MOTION .....	32
3.1 Motion in a Static Uniform Magnetic Field .....	32
3.2 Magnetic Moment in Static Uniform Magnetic Field .....	34
3.3 Motion in Static Uniform Electric and Magnetic Fields .....	35
3.4 Motion in Slowly Varying Magnetic Field: Guiding Center Motion .....	37
3.4.1 Gyro-frequency in Slowly Varying Magnetic Field .....	37
3.4.2 Gyro-average .....	39
3.4.3 Guiding Center Motion .....	40
3.5 Motion in Axisymmetric Tokamak .....	43
3.5.1 Trapped/Passing Condition .....	44
3.5.2 Banana Orbit .....	46
3.6 Numerical Results for Motion in Axisymmetric Tokamak .....	52
4 SERENDIPITY SHAPE FUNCTIONS IN NIMROD's PARTICLE SIMULATION .....	57
4.1 Gathering and Scattering of Particles on the Finite Element Grid .....	59
4.1.1 Bilinear Shape Functions .....	63
4.2 Serendipity Shape Functions .....	65
4.2.1 Construction of the Biquartic Serendipity Shape Functions .....	69
4.3 Numerical Results for Serendipity Basis Functions .....	73
4.4 The Method of Least Squares .....	80

5	THE $\delta f$ -PIC APPROACH IN NIMROD	83
5.1	Initial Setup: Particle Load onto Computational Domain	85
5.2	The $\delta f$ -PIC Approach in NIMROD	88
5.2.1	Deposition of Energetic Particle Pressure Tensor	92
5.3	Numerical Results from NIMROD PIC Simulations	95
6	CONCLUSION AND FUTURE WORK	105
	REFERENCES	109
	APPENDICES	112
A	The Dirac Delta Function in Curvilinear Coordinates	113
B	Particle in Magnetic Field: Non-canonical Variables	115
C	Derivation of Guiding Center Velocity	119
D	Trapped/Passing Particle: Orbit Period	121
E	Serendipity Shape Functions	123
	CURRICULUM VITAE	126

## LIST OF FIGURES

	Page
<p>Figure 1.1 An energetic particle orbit in Earth’s magnetic dipole field is indicated by the dashed line. (a) Projection onto the North-South (poloidal) plane, where the gyro-motion, bounce motion and the poloidal angle are shown. (b) Shows the view from above the North Pole. The azimuthal precession motion from East to West is shown. The color red through violet shows the trajectory advancing in time. The figure was taken from Heidbrink and White (2020). . . . .</p>	2
<p>Figure 1.2 Typical bouncing particle motion in a tokamak. The dotted line shows the guiding center motion along the toroidal direction. When the particle “feels” a stronger magnetic field, it bounces. Note that this bounce behavior can be projected onto the poloidal (<math>R, Z</math>) plane. Some projections of the guiding center motion into the poloidal plane are shown in Fig. 1.3. Shown for part of the trajectory is the gyro-motion where the particle travels in a helix about the magnetic field line. The East-West (azimuthal) precession in Fig. 1.1(b) manifests when the bounce tips (where two dotted curves come together) moves in toroidal angle <math>\varphi</math>. . . . .</p>	3
<p>Figure 1.3 A contour plot of normalized poloidal magnetic flux <math>\bar{\psi}_p</math> is plotted and overlaid by three different particle orbits. The innermost orbit (1) is called a barely trapped particle, the middle orbit (2) is a passing particle since it circumnavigates the entire flux surface, and the outermost orbit (3) is a deeply trapped particle. This shows the poloidal projection of these particle’s guiding center trajectories. . . . .</p>	4
<p>Figure 1.4 Data from DIII-D experiment, discharge #96043. (a) Time at which the neutral beam and the RF wave were injected into the plasma. (b) Electron central temperature and neutron reaction rate vs. time. (c) Plasma density and plasma stored energy given as functions of time. The figure was taken from Choi et al. (2007) . . . . .</p>	5
<p>Figure 2.1 The major radius <math>R_0</math> points from the origin to the magnetic axis. The minor radius <math>a</math> is the radius of the last closed magnetic flux surface. The dotted line indicates flux surfaces that are within the minor radius. The angles <math>\theta</math> and <math>\varphi</math> are referred to as the poloidal and toroidal angles, respectively. . . . .</p>	28
<p>Figure 2.2 The helical magnetic field, due to the poloidal and toroidal components, wraps around the flux surfaces. . . . .</p>	29

Figure 3.1 Gyro-motion in the plane perpendicular to the static uniform magnetic field where the magnetic field is pointing into the page. . . . .	33
Figure 3.2 Guiding center motion, particle gyrating about the magnetic field line.	38
Figure 3.3 Potential energy for a particle in a magnetic mirror field. This mirror field is realized in tokamaks as particles travel radially inwards (in major radius $R$ ) to stronger magnetic field (see Eq. (2.64)), causing particles with not enough parallel kinetic energy to be trapped inside the magnetic potential.	43
Figure 3.4 Depending on the initial parallel velocity, a particle in an axisymmetric field (an ion is depicted here) will bounce inward or outward due to the magnetic curvature and gradient drifts. . . . .	47
Figure 3.5 Trapped (banana) and passing orbits on the poloidal plane. . . . .	50
Figure 3.6 NIMROD uses a left-hand cylindrical coordinate system. The magnetic flux $\psi$ is plotted as the contours and the particles are pushed in the equilibrium fields only. The $\mathbf{v}_c$ and $\mathbf{v}_{\nabla B}$ drifts point in the negative $Z$ -direction causing the ion with initial negative parallel velocity to bounce outward off its starting flux surface and the ion with the positive initial parallel velocity to bounce inward from the same starting point. . . . .	52
Figure 3.7 A contour plot of normalized poloidal magnetic flux $\bar{\psi}_p$ is overlaid by three different particle orbits. The innermost orbit (1) is barely trapped, the middle orbit (2) is passing since it circumnavigates the entire flux surface, and the outermost orbit (3) is deeply trapped. . . . .	53
Figure 3.8 Figure (a) shows the orbit of barely trapped (1) and deeply trapped (3) particles overlaid on a contour plot of $\bar{\psi}_p$ . Figure (b) shows the corresponding safety factor $q_s$ where the value of $q_s$ is shown for orbits 1 and 3 at their initial flux surfaces. . . . .	54
Figure 4.1 Figure (a) shows the logical grid that the fields are defined on in terms of either the 2D Lagrange or Serendipity basis sets. Figure (b) shows the physical grid for DIII-D geometry. Here computational domain is divided up amongst 16 different processors. The magnetic axis indicated by a black dot on the physical grid corresponds to the $\eta$ -axis ( $\xi = 0$ ) on the logical grid.	58
Figure 4.2 The top two cells are the node location for the Serendipity sets (left: bicubic and right: biquartic) while the bottom two cells are the node locations for the Lagrange sets (left: bicubic and right: biquartic). The nodal locations for both are the same except the Serendipity has fewer nodes in the center of the finite element cell. . . . .	59

Figure 4.3	A square finite element cell with a bilinear decomposition consists of 4 vertex node locations at the corners of the cell. The finite element cell is defined on the interval $[-1, 1]$ for both $\xi$ and $\eta$ . The center of the cell is placed at the location $(0, 0)$ . The locations of the nodes are indicated by dots.	64
Figure 4.4	Terms that are included in $\mathcal{P}_4^2$ are shown in red.	66
Figure 4.5	Terms that are included in $\mathcal{S}_4^2$ are shown in red. Notice the extra two terms $\{\xi^4\eta, \xi\eta^4\}$ that were added to the set.	67
Figure 4.6	Terms that are included in $\mathcal{R}_4^2$ are shown in red. Notice that the two terms $\{\xi^4\eta, \xi\eta^4\}$ are still included in the set but the term $\{\xi^2\eta^2\}$ , which results in an interior node, is removed.	68
Figure 4.7	A square finite element cell with complete fourth-order (biquartic) Serendipity decomposition consists of 17 node locations with one in the middle of the cell. The center of the cell is placed at the location $(0, 0)$ . The location of the nodes are indicated by dots.	70
Figure 4.8	A linear combination of the adjacent mid-side nodes and the center node is subtracted from the bilinear Lagrange polynomial $L_1^1(\xi, \eta)$ to make the Serendipity biquartic polynomial $S_1^4(\xi, \eta)$ . This insures that these Serendipity polynomials satisfies the conditions stated in Eqs. (4.24) and (4.25). Note that an example for node $k = 1$ is shown.	72
Figure 4.9	From left to right, the nodal representations are: bilinear, Serendipity biquadratic, Serendipity biquartic, and 2D Lagrange biquartic ("exact"). The circle around the nodes indicates the coinciding nodes from the previous representation. Thus for example, when running the Serendipity biquartic case, the 2D Lagrange coefficients at the circled nodes are directly used in the Serendipity basis representation.	74
Figure 4.10	The error $\epsilon_D$ between the different representations (see Eq. (4.37)) is shown. The three errors relative to the "exact" 2D Lagrange are: bilinear (biline), Serendipity biquadratic (biquad), and the reduced Serendipity biquartic (biquar). Note that the $y$ -axis is log-scaled.	75
Figure 4.11	The error $\epsilon_D$ for the reduced Serendipity biquartic case does worse than the biquadratic case. However, both are still more accurate than the bilinear (biline) approach.	76
Figure 4.12	Average error in the physical $R$ (m) coordinate for all Serendipity (complete/reduced) sets compared against the "exact" 2D Lagrange polynomials. The errors were averaged over $\sim 30000$ particles. The cases were run for 35, 350, and 3500 time steps with each time step $\Delta t = 2.0 \times 10^{-8}$ seconds. The results shown are for bilinear (biline), biquadratic (biquad), bicubic (bicube), reduced biquartic (biquar), biquartic (cmplt4), reduced biquintic (biquin), and reduced bisextic (bisext).	77

Figure 4.13 Average error in the parallel velocity  $v_{\parallel}$  (m/s) for all Serendipity (complete/reduced) sets compared against the “exact” 2D Lagrange polynomials. The errors were averaged over  $\sim 30000$  particles. The cases were run for 35, 350, and 3500 time steps with each time step  $\Delta t = 2.0 \times 10^{-8}$  seconds. The results shown are for bilinear (biline), biquadratic (biquad), bicubic (bicube), reduced biquartic (biquar), biquartic (cmplt4), reduced biquintic (biquin), and reduced bisextic (bisext). Note that the biquartic case with the central node (cmplt4) outperforms the fifth and sixth order representations. . . . . 78

Figure 4.14 The total memory used for each representation is plotted as a function of polynomial degree. The Serendipity (complete or reduced) cases use much less memory than the full 2D Lagrange polynomials. Memory is given in Megabits (Mb). Roughly 30000 particles were used, thus the memory used will increase with more particles, but the overall trend between different cases will remain similar. The total memory consists of the basis functions  $N_k^p$ , the global field array, and the computational particle structure that stores the particle information. . . . . 79

Figure 4.15 Comparing the total run-time (s) for different representations as a function of polynomial degree. The data points with  $\blacktriangledown$  indicates the load-balanced and  $\bullet$  indicates the non-load-balanced cases. Note that  $y$ -axis is given in log-scale. . . . . 80

Figure 5.1 Figure (a) shows the equilibrium pressure  $P_0$  and the normalized safety factor  $q_s$  vs. the normalized poloidal flux  $\bar{\psi}_p$ . Portion of the plasma where  $q_s < 1$  (roughly at  $\bar{\psi}_p < 0.168$ ) undergoes the 1/1 kink. Figure (b) shows the magnetic flux surface geometry for DIII-D (value decreases from green to red). 87

Figure 5.2 (Left) shows data from DIII-D experiment, discharge #96043. (a) Time at which the neutral beam and the RF wave were injected into the plasma. (b) Electron central temperature and neutron reaction rate vs. time. (c) Plasma density and plasma stored energy given as functions of time. (Right) shows the energy dependence of the energetic particle distribution function. It shows the energetic slowing down distribution function  $f_{\text{slow}}$  with  $E_{\text{crit}} = 50$  keV and the more energetic tail  $f_{\text{tail}}$  driven by RF waves. Here the injection energy of the neutral beam,  $E_{\text{inj}} = 80$  keV. The left figure figure was taken from Choi et al. (2007). . . . . 96

Figure 5.3 Shows the growth rate vs. time graph for the ideal fluid only calculation. Polynomial degree 1 (green) has a growth rate of  $\gamma = 35,344$  Hz, polynomial degree 2 (blue under pink) has a growth rate of  $\gamma = 32,810$  Hz, and polynomial degree 4 (pink) has growth rate of  $\gamma = 32,809$  Hz. . . . . 97

Figure 5.4 Shows the error in divergence of magnetic field (div(B)) vs. time graph, *i.e.* div(B) diagnostic plot. The polynomial degree 1 (green) case has much greater error associated with the converged eigenfunction. The polynomial degree 2 (blue) and 4 (green) do a better job preserving  $\nabla \cdot \mathbf{B} = 0$  condition beyond  $10^{-4}$  seconds. . . . . 98



- Figure 5.5 (Top left) Contour plot of  $V_R$  for polynomial degree 1 case. (Top right) Contour plot of  $T_e$  for polynomial degree 1 case. (Bottom left) Contour plot of  $V_R$  for polynomial degree 4 case. (Bottom right) Contour plot of  $T_e$  for polynomial degree 4 case. . . . . 99
- Figure 5.6 Figure (a) shows the growth rate of four different calculations. Figure (b) shows the blow up of the converged part of the growth rate plot. The fluid only calculation (pink) is given as a reference to show that with energetic particles present the growth rate is slightly lower. This shows increased stabilization using a slowing down distribution with  $\beta_{\text{frac}} = 0.20$ . Note that with increasing particle number for the simulation the noise of the particle simulation goes down (blue, green, and teal). . . . . 100
- Figure 5.7 Figure (a) shows the load-balanced case. Particle distribution among processors is uniform where the processor with the maximum number of particles has 41,766 and the processor with the minimum number of particles has 41,574. Figure (b) shows the not load-balanced case. We can see that the outer, low pressure region has very few particles while the core with the highest pressure has the most particle per processor. At the 1/1 surface, the particle per processor amount drops due to the smaller finite element cells used combined with the technique of importance sampling. For both cases 8 million particles were used. . . . . 100
- Figure 5.8 Compares the growth rates for the PiC and newpart routines. The top most pink line (above 30,000 Hz) is the growth rate for fluid only calculation. The two calculations right below 30,000 Hz are the growth rates for PiC (green) and newpart (blue) for  $\beta_{\text{frac}} = 0.2$ . The two calculations right above 20,000 Hz are the growth rates for PiC (green) and newpart (purple) for  $\beta_{\text{frac}} = 0.4$ . Finally, the two calculations right above 10,000 Hz are the growth rates for PiC (teal) and newpart (magenta) for  $\beta_{\text{frac}} = 0.6$ . . . . . 101
- Figure 5.9 Pressure contour plots for the newpart using a representation in the push (evaluation of fields) and find (mapping from real to logical coordinates). (Top left) Contour plot of  $\delta P_{\perp}$  for newpart bilinear. (Top right) Contour plot of  $\delta P_{\text{ani}}$  for newpart bilinear. (Bottom left) Contour plot of  $\delta P_{\perp}$  for PiC bilinear. (Bottom right) Contour plot of  $\delta P_{\text{ani}}$  for PiC bilinear. The contour plots were taken at 4000 time steps and show similar structure. . . . . 102
- Figure 5.10 Contour plots of the anisotropic part of the pressure tensor,  $\delta P_{\text{ani}}$ , 4000, 5000, 6000, 7000, and 8000 time steps indicate a propagating mode with the anisotropic pressure contours rotating in a counter-clockwise direction in the poloidal plane. . . . . 102
- Figure 5.11 Shows the blow up of the growth rate for fluid only (green), bilinear (purple), biquadratic (magenta), and complete biquartic (teal). The higher-order bases do not have an effect on the 1/1 internal kink mode. . . . . 103

Figure 6.1 Figure (a) shows growth rates for NIMROD's  $\delta f$ -continuum and  $\delta f$ -PIC approaches where  $E_{\text{crit}} = 50$  keV and  $E_{\text{inj}} = 80$  keV were used for the calculation. Figure (b) also shows growth rates for  $\delta f$ -continuum and  $\delta f$ -PIC approaches but with  $E_{\text{crit}} = 28$  keV and  $E_{\text{inj}} = 227$  keV. Need RF tail in NIMROD's PIC routine to resolve the higher  $\beta$  cases. . . . . 107

## CHAPTER 1

### INTRODUCTION

In magnetized fusion experiments such as tokamaks, an extremely high temperature ( $\sim 1.5 \times 10^8$  K) plasma is confined using magnetic fields. Since plasma consists of negatively (electrons) and positively (ions) charged particles and these particles follow the magnetic field lines in a helical trajectory, magnetic confinement is possible. Through magnetic confinement, the high temperature plasma does not come in contact with the walls of the device. If it did, the walls of the tokamak would melt or even evaporate from the extreme heat load. Extreme temperatures are needed for thermonuclear fusion to occur in these devices for net positive output of energy (Ongena et al., 2016). That being said, magnetic confinement is not an easy task. This complex system gives rise to many instabilities from many different sources. Energetic particles introduced through fusion reaction or from neutral beams impinging on the plasma alter the stability properties.

Although all particles in plasma can be considered energetic, what we mean by energetic particles are those with energies much greater than the bulk plasma temperature. For example, when the energetic plasma from the solar wind hits the Earth's colder magnetosphere, *i.e.* plasma, we have interaction between the bulk plasma and the energetic particles. In laboratory plasma, such as ITER, energetic particles are produced by neutral beams (Stix, 1972), external radio-frequency (RF) sources (Stix, 1975), or  $\alpha$ -particles created by fusion reactions between deuterium and tritium (Ongena et al., 2016). These sub-populations of energetic particles can resonate with long-wavelength MHD modes and can have significant effect on plasma stability and particle transport.

In Earth's magnetosphere, regions of energetic particles originating from the Sun's solar wind are called the Van Allen radiation belt. The motion of energetic particles in the Earth's magnetic dipole field has three main components: (i) fast gyro-motion about the magnetic field line, (ii) slower bounce motion in the North-South plane, and (iii) slowest

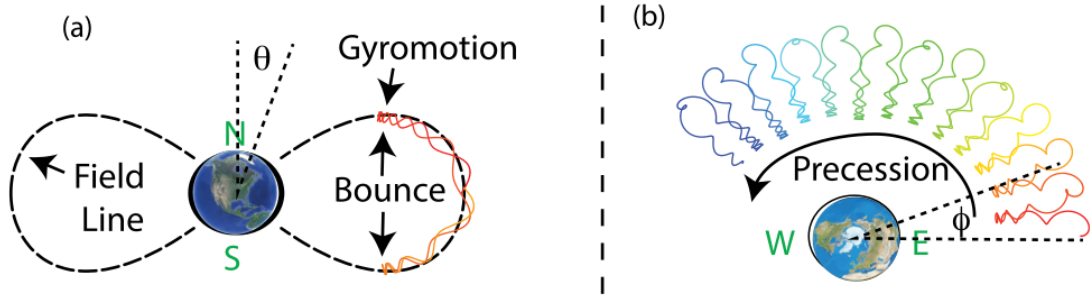


**Figure 1.1:** An energetic particle orbit in Earth’s magnetic dipole field is indicated by the dashed line. (a) Projection onto the North-South (poloidal) plane, where the gyro-motion, bounce motion and the poloidal angle are shown. (b) Shows the view from above the North Pole. The azimuthal precession motion from East to West is shown. The color red through violet shows the trajectory advancing in time. The figure was taken from [Heidbrink and White \(2020\)](#).

azimuthal precession motion in the East-West plane (see Fig. 1.1). The gyro-motion is characterized by the gyro-frequency  $\Omega = qB/m$ , where  $q$  is the charge of the particle,  $m$  the mass of the particle, and  $B$  the magnetic field strength. The bounce motion arises from the magnetic field gradient that exists along field lines in the North-South plane. A particle with inadequate parallel energy (with respect to the magnetic field) will bounce and change directions when it reaches a region of stronger magnetic field. This motion is typically characterized in the poloidal  $(R, Z)$  plane by the bounce frequency  $\omega_\theta$ . Finally, the azimuthal precession motion, which is the slow East-West precession of the particle around the Earth, is typically characterized by the toroidal angle  $\varphi$  with a frequency  $\omega_\varphi$ . These types of orbits exist in tokamaks as well (see Fig. 1.2). The gyro-motion sets the fastest timescale,  $1/\Omega \sim 2 \times 10^{-8}$  s, of these energetic particles. The bounce period,  $\tau_b \sim 5 \times 10^{-5}$  s, describes the motion projected onto the poloidal plane. The motion in the precessing toroidal direction is characterized by a timescale  $\tau_\varphi \sim 2 \times 10^{-4}$  s. These motions are associated with the first, second, and third adiabatic invariants (respectively) in plasma physics.

From Hamiltonian mechanics, nearly periodic systems with slowly varying parameters have associated, approximate constants of motion ([Landau and Lifshitz, 1976](#)) called adia-

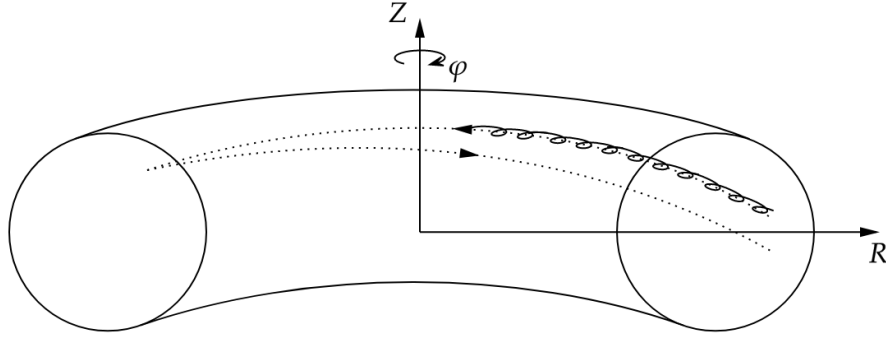


**Figure 1.2:** Typical bouncing particle motion in a tokamak. The dotted line shows the guiding center motion along the toroidal direction. When the particle “feels” a stronger magnetic field, it bounces. Note that this bounce behavior can be projected onto the poloidal  $(R, Z)$  plane. Some projections of the guiding center motion into the poloidal plane are shown in Fig. 1.3. Shown for part of the trajectory is the gyro-motion where the particle travels in a helix about the magnetic field line. The East-West (azimuthal) procession in Fig. 1.1(b) manifests when the bounce tips (where two dotted curves come together) moves in toroidal angle  $\varphi$ .

batic invariants. Hence, from each degree of freedom that exhibits periodicity, an adiabatic invariant can be formulated. In plasma physics, three main adiabatic invariants, related to the particle motions mentioned above, are introduced (Gurnett and Bhattacharjee, 2017). The first is associated with the fast gyro-motion about a magnetic field line, which is related to the approximately conserved magnetic moment  $\mu$ . The second is associated with the parallel (with respect to the magnetic field) periodic motion, *i.e.* the bounce motion which is projected in the poloidal plane in Fig. 1.3. The third is associated with the azimuthal drift motion due to the magnetic gradient drift and the magnetic curvature drift. The third adiabatic invariant states that the magnetic flux through the locus of points created by the azimuthal drift is constant. Besides the adiabatic invariants, when considering energetic ions, we have the exact invariant of energy for these particles. Often binary collisions of energetic ions with themselves or the background plasma can be neglected. Also, if the kinetic energy is much greater than the potential energy, we can assume that the kinetic energy (hence the total energy) of these ions is constant. In this thesis, we push particles in equilibrium axisymmetric tokamak fields and assume that the lowest order electric field

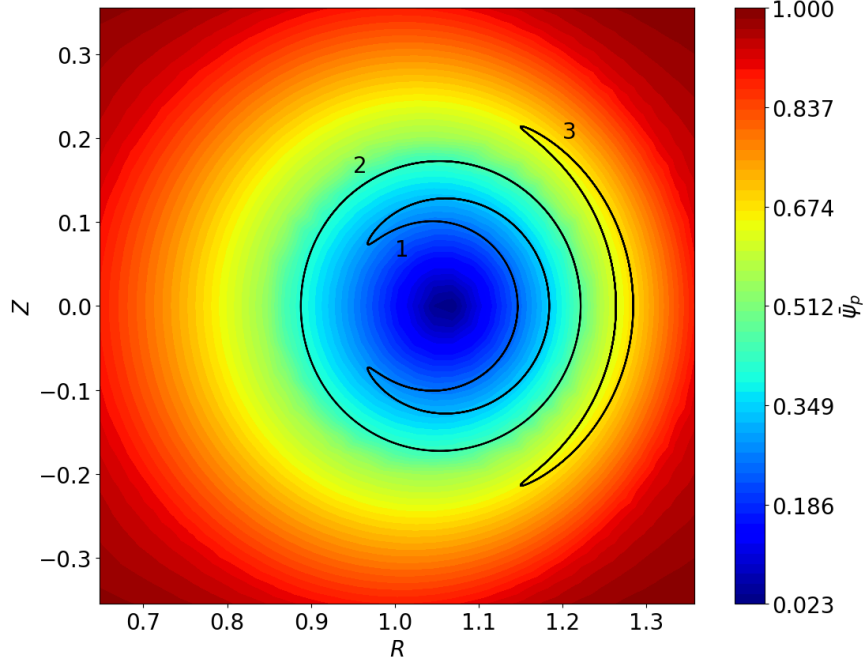


**Figure 1.3:** A contour plot of normalized poloidal magnetic flux  $\bar{\psi}_p$  is plotted and overlaid by three different particle orbits. The innermost orbit (1) is called a barely trapped particle, the middle orbit (2) is a passing particle since it circumnavigates the entire flux surface, and the outermost orbit (3) is a deeply trapped particle. This shows the poloidal projection of these particle's guiding center trajectories.

vanishes. Kinetic energy conservation is exact for this case. It is also worth mentioning that in axisymmetric tokamaks, the toroidal canonical momentum is another exact invariant that gives greater insight into the physics of these energetic ions.

Why are we interested in energetic ion physics and the single particle picture? The interaction between energetic ions and the bulk, MHD plasma requires the details of the ion orbits. The energetic ions interact with the MHD modes to either stabilize or destabilize the plasma as a whole. One example is the so-called giant sawtooth discharge (Choi et al., 2007) which was observed (Heidbrink et al., 1999) in the DIII-D tokamak (Luxon et al., 2005; Luxon, 2002). In magnetic confinement schemes such as the tokamak, neutral beams are used to impart toroidal momentum which can help in plasma confinement by inducing plasma rotation (Hopf et al., 2021). When the neutral beam comes in contact with the

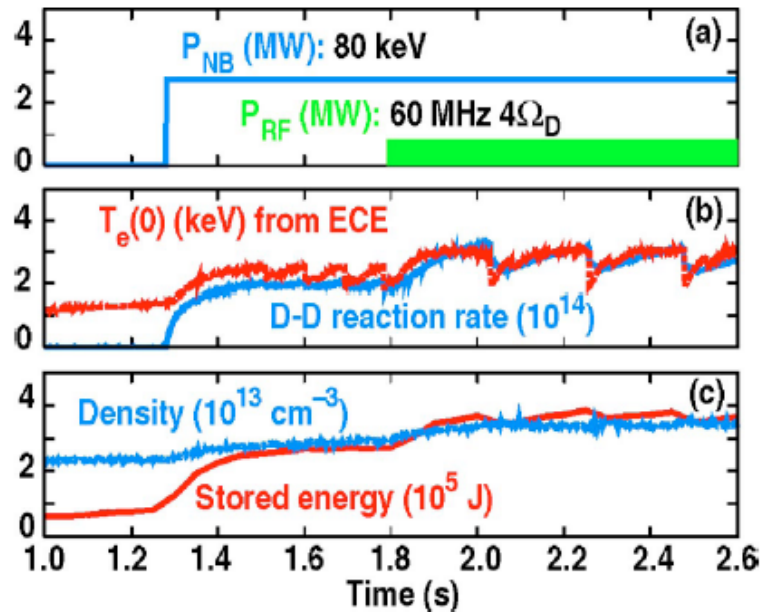


**Figure 1.4:** Data from DIII-D experiment, discharge #96043. (a) Time at which the neutral beam and the RF wave were injected into the plasma. (b) Electron central temperature and neutron reaction rate vs. time. (c) Plasma density and plasma stored energy given as functions of time. The figure was taken from [Choi et al. \(2007\)](#)

plasma in the fusion device, it is ionized, thereby introducing an energetic ion population. Typical injection energies are on the order of 100 keV. It is possible to increase the energy of these ions further to roughly 600 keV by using RF waves that resonate with the energetic ions. This can help stabilize the plasma against an instability known as the internal kink. It is speculated that the conservation of the third adiabatic invariant of these energetic ions, after the use of RF waves, is the stabilizing factor of the internal kink or sawtooth mode. Figure. 1.4 shows an increase in the electron temperature after the neutral beam is injected into the plasma. Once the electron temperature reaches a certain value it starts to drop and climb exhibiting small sawtooth behavior due to the internal kink modes, a kinking of the plasma column inside the hot core. The RF waves help stabilize these small sawteeth by driving a high energy tail in the energetic ion population. It is believed that the conservation of the third adiabatic invariant is responsible for this stabilization. But, eventually another instability takes place which results in giant sawteeth. Understanding

the behavior of energetic ions and how they interact with MHD modes so instabilities such as the giant sawtooth can be better understood and accounted for is imperative to improving tokamak confinement.

Inter-species collisions between a diffuse population of energetic ions are rare and often can be neglected. This implies that the collisionless Vlasov equation can be used. This is due to the high energy and the typical low density of these populations. The result is a small population of energetic particles does not obey the Maxwellian distribution; therefore, a fluid approach cannot be used for these particles. This means that kinetic theory needs to be employed. We consider timescales of several wave periods, which is less than the timescale over which collisions cause the distribution to evolve. The distribution function of energetic particles can have complex dependence on energy and direction. Also, small differences in a particle's velocity can yield very different trajectories ([Heidbrink and White, 2020](#)).

The task when considering energetic particle effects on the bulk plasma, is to first predict their motion and then couple them into the fluid MHD equations via velocity moments of the energetic particle distribution function. This is referred to as closing the MHD equations. The approach is called the hybrid kinetic-MHD model ([Cheng, 1991](#); [Cheng and Johnson, 1999](#)). This is not an easy task and requires sophisticated analytical and numerical techniques. Two main approaches exist when considering the interaction between the bulk plasma and the sub-population of energetic particles: the (i) current-coupling scheme and the (ii) pressure-coupling scheme ([Tronci et al., 2014](#)). The current-coupling scheme is more general and uses the energetic particle momentum and the density to introduce these energetic particles into the MHD equations. The pressure-coupling scheme only applies in cases where the energetic population is small enough that the inertia of these particles does not have to be considered. This requires the density of the energetic particles to be much less than the density of the bulk plasma ( $n_{\text{hot}} \ll n_{\text{MHD}}$ ). Their energy, however, can be high enough so that they have a significant anisotropic pressure moment that alters the center-of-mass flow evolution for the bulk plasma.



The bulk plasma is described by the MHD fluid equations and the energetic particles are introduced into the flow evolution equation as an energetic particle pressure tensor moment. NIMROD specifically uses the  $\delta f$  approach for the PIC method (Kim, 2008). The  $\delta f$ -PIC is a control variates method (Aydemir, 1994), where the distribution function for the energetic particles is separated into a larger time-independent equilibrium part and a small time-dependent perturbation. The control variates method tends to lower the noise for PIC simulations, since the larger portion of the distribution function, *i.e.* the equilibrium portion, is specifically chosen so that it can be integrated fairly easily either numerically or sometimes even analytically. The perturbed part of the energetic distribution function, *i.e.* the particle weights, is evolved in time (Parker and Lee, 1993). Information from the perturbed part is used in the update of the center-of-mass flow evolution equation in the form of the energetic particle pressure tensor moment.

There are two approaches that are implemented in NIMROD to solve the kinetic equation and close the MHD fluid equations—(i) a continuum approach and (ii) the particle-in-cell (PIC) method. The continuum approach (Held et al., 2015) directly solves the kinetic equation using a discretization of the two-dimensional (2D) velocity space. For the PIC approach, which is the main concern for this thesis, computational particles with associated weights are pushed along the equilibrium fields. The particle weights and the velocity vectors are then used to construct the energetic particle pressure tensor moment, which then closes the MHD equation by appearing in the center-of-mass flow evolution equation (Kim, 2008). Note that in both cases the pressure-coupling scheme, discussed previously, is used.

NIMROD (Non-Ideal Magnetohydrodynamics with Rotation—Open Discussion) solves the extended MHD equations by using 2D finite elements in the poloidal plane and a Fourier decomposition in the periodic toroidal direction (Sovinec et al., 2004). For the time advance of the MHD equations, NIMROD has both semi-implicit and implicit time discretization for various terms. Higher order, 2D Lagrange polynomials are utilized in the poloidal plane for the 2D finite element discretization. This and the semi-implicit time advance, helps resolve the complex, extended MHD equations.

We begin in Chapter 2 by discussing some preliminaries of plasma physics. A brief discussion of Lagrangian and Hamiltonian mechanics is given. In some situations, a crude understanding of non-canonical mechanics is useful, thus we briefly discuss that as well. A distribution function is constructed using the particle position and momentum or velocity for non-relativistic particles. These also can be non-canonical variables, *e.g.*, with magnetic field present the particle momentum is no longer the canonical momentum. Therefore, we build Liouville's equation using non-canonical notation. Once Liouville's equation is presented with the non-canonical notation, we can easily simplify it to the more convenient and familiar form. From Liouville's equation, the evolution for a single particle distribution function can be obtained. We then present conditions that allow us to drop the collisional term, which gives us the Vlasov equation. The Vlasov equation is further reduced to the drift kinetic equation by averaging out the gyro-motion of the particles. Finally, an axisymmetric magnetic field configuration is briefly mentioned. This will be used in Chapter 3 to discuss the analytical results of single particle motion in axisymmetric tokamak geometry.

In Chapter 3, we consider single particle motion both analytically and numerically. We start from the most simple case of a static, uniform magnetic field and then build up to deriving the guiding center velocity. The two main orbit types, passing and trapped, are considered. The analytical form for the banana width and the bounce period are derived. The analytical results are compared to the numerical results from NIMROD's PIC algorithm with the computational particles pushed along the equilibrium fields for an axisymmetric tokamak case.

Chapter 4 introduces Serendipity basis sets. These basis sets are subsets of the 2D Lagrange polynomials already implemented in NIMROD. Up to sixth order for the Serendipity basis are implemented for testing. The Serendipity bases in NIMROD's PIC algorithm are used for the particle gather and scatter in the hopes of obtaining more accurate particle trajectories while still keeping a small memory footprint and run-time. The Serendipity bases are compared to the 2D Lagrange polynomials, and the results for accuracy, efficiency, and memory footprint are presented.

Chapter 5 discusses the initial sampling of energetic ion population using importance sampling (Birdsall and Langdon, 2018; Hammersley and Handscomb, 1964). We discuss sampling from a slowing down distribution function and the application of the  $\delta f$ -PIC method implemented in NIMROD. The energetic particle information is dumped onto the finite element grid via the energetic particle pressure tensor, a process known as deposition. We consider, carefully, the deposition process. Also, the numerical results of the Serendipity basis sets are presented in how well they resolve the growth rate of 1/1 internal kink mode.

Finally, in Chapter 6 we conclude this thesis and suggest future work. Many improvements can be made to the  $\delta f$ -PIC approach implemented in NIMROD. One such improvement would be to extend this work to allow for non-linear simulations as was discussed by Parker and Lee (1993). Another improvement would be to more properly couple the energetic particles into the MHD equations (Liu et al., 2022a; Tronci et al., 2014). This becomes important when the density of the energetic ions becomes comparable to that of the thermal ions. It is estimated that 30% of the ion population in the ITER tokamak will be energetic  $\alpha$ -particles (Putvinski, 1998) born in deuterium–tritium fusion events. Clearly, the ordering  $n_{\text{hot}} \ll n_{\text{MHD}}$  would not hold. Implementing a different coupling scheme would allow NIMROD’s  $\delta f$ -PIC code to study the important effects that a substantial population of energetic ions could have on the MHD plasma stability. We would also like to compare NIMROD’s drift kinetic  $\delta f$ -PIC and drift kinetic continuum approaches to other kinetic-MHD (both gyrokinetic and drift kinetic) codes and validate them against experimental results from the DIII-D tokamak, as was done in Brochard et al. (2022).

## CHAPTER 2

### PRELIMINARIES TO PLASMA PHYSICS

A fundamental approach to classical mechanics is the use of a dimensionless representation of bodies called point particles. In a perfectly ionized plasma, the point particles are negatively charged electrons and positively charged ions. If their motion can be described without considering of their dimensions, then the point particle approximation can be used. A vector describes a particle's position with three Cartesian coordinates as its components. The total time derivative of such a vector is the velocity and the total time derivative of the velocity is the acceleration. Through the classical (non-quantum) empirical experience, it is understood that if the position and velocity of a particle are known simultaneously at a particular instant in time, then any subsequent motion can be obtained. In other words, the acceleration is uniquely determined via the equations of motion ([Landau and Lifshitz, 1976](#)). If a system of  $N$  particles is considered, the position of each particle in space is specified by its own vector. The number of vector components needed to uniquely specify the position and orientation of a system is called the degrees of freedom. For example, a system of  $N$  point particles, where each particle needs  $s$  number of coordinates to describe its position completely, has  $sN$  degrees of freedom. Therefore, to uniquely determine the motion of the system, the position and velocity of each particle needs to be specified. If the number of particles is large, which is the case in a confined plasma where  $N$  is of the order of Avagadro's number, this approach is impractical and unnecessary. Instead, an ensemble of systems is considered to obtain a statistical average.

#### 2.1 Lagrangian and Hamiltonian Mechanics

When considering an ensemble of  $N$ -particle systems, it is advantageous to introduce a phase space of  $2sN$  dimensions and employ Hamiltonian mechanics. Lagrangian and Hamiltonian mechanics are related via the Legendre transformation. The independent vari-

ables for the Lagrangian formulation are  $(q^i, \dot{q}^i, t)$  where  $\dot{q}^i$  is referred to as the generalized velocity. For the Hamiltonian formulation, the canonical momenta are used instead of the generalized velocities  $(q^i, \mathcal{P}^i, t)$ . Therefore, via Legendre transform the generalized coordinates,  $q^i$  and the canonical momenta  $\mathcal{P}^i$  are placed on an equal footing. First, we will construct the Lagrangian and the Hamiltonian formulations for a charged particle in an electromagnetic field. Then we will use a non-canonical formulation of Hamiltonian mechanics to show that the original equations of motion can be obtained using the particle momenta  $p^i = mv^i$ , instead of the canonical momenta  $\mathcal{P}^i$ . Throughout this section we will let the charge of a particle be represented by  $e$  instead of  $q$ .

### 2.1.1 Lagrangian for a Particle in an Electromagnetic Field

The Lagrangian of a charged particle in an electromagnetic field can be obtained by considering the equations of motion from the fundamental Lorentz force,

$$\mathbf{F}(\mathbf{x}, \mathbf{v}, t) = e(\mathbf{E} + \mathbf{v} \times \mathbf{B}) . \quad (2.1)$$

The force is acting on a particle with charge  $e$ , which causes it to accelerate. We use vector notation here for simplicity. The electric field and the magnetic field can vary in space and time,  $\mathbf{E}(\mathbf{x}, t)$  and  $\mathbf{B}(\mathbf{x}, t)$ . The case where the sources of the fields, *i.e.* charge density  $\rho$  and current density  $\mathbf{J}$ , are far from the charged particle is considered. Using the Lorentz force, the following equations of motion for a charged particle is obtained

$$m \frac{d\mathbf{v}}{dt} = e(\mathbf{E} + \mathbf{v} \times \mathbf{B}) . \quad (2.2)$$

The fields  $\mathbf{E}$  and  $\mathbf{B}$  are expressed in terms of the potentials in the Lagrangian formulation. We use the Lorenz gauge

$$\mathbf{E} = -\nabla\phi - \frac{\partial\mathbf{A}}{\partial t} \quad (2.3)$$

and

$$\mathbf{B} = \nabla \times \mathbf{A} , \quad (2.4)$$

where  $\phi$  is the electrostatic scalar potential and  $\mathbf{A}$  is the vector potential. Therefore, the equations of motion is expressed in terms of the potentials as

$$m \frac{d\mathbf{v}}{dt} = e \left( -\nabla\phi - \frac{d\mathbf{A}}{dt} + (\nabla\mathbf{A}) \cdot \mathbf{v} \right) , \quad (2.5)$$

where  $d/dt = \partial/\partial t + \mathbf{v} \cdot \nabla$  was used to introduce the total time derivative for the vector potential. The customary approach for deriving the Lagrangian from the equations of motion is to multiply it by some spatial variation  $\delta\mathbf{x}$  and integrate over time

$$m \int_{t_1}^{t_2} \delta\mathbf{x} \cdot \frac{d\mathbf{v}}{dt} dt = e \int_{t_1}^{t_2} \delta\mathbf{x} \cdot \left( -\nabla\phi - \frac{d\mathbf{A}}{dt} + (\nabla\mathbf{A}) \cdot \mathbf{v} \right) dt . \quad (2.6)$$

We integrate by parts and note that the “surface” terms vanish if the end points are not varied. Thus, we end up with the expression

$$\int_{t_1}^{t_2} \frac{1}{2} m \delta(\mathbf{v} \cdot \mathbf{v}) dt = e \left[ \int_{t_1}^{t_2} \delta\phi dt - \int_{t_1}^{t_2} \delta\mathbf{v} \cdot \mathbf{A} dt - \int_{t_1}^{t_2} \delta\mathbf{A} \cdot \mathbf{v} dt \right] , \quad (2.7)$$

where  $\delta\phi = \delta\mathbf{x} \cdot \nabla\phi$  is the variation of the scalar potential,  $\delta\mathbf{x} \cdot (\nabla\mathbf{A}) \cdot \mathbf{v} = \delta\mathbf{A} \cdot \mathbf{v}$  is the variation of the vector potential and

$$\frac{d\delta\mathbf{x}}{dt} \cdot \mathbf{v} = \delta\mathbf{v} \cdot \mathbf{v} = \frac{1}{2} \delta(\mathbf{v} \cdot \mathbf{v}) .$$

Finally, noting that  $\delta(\mathbf{v} \cdot \mathbf{A}) = \delta\mathbf{v} \cdot \mathbf{A} + \delta\mathbf{A} \cdot \mathbf{v}$ , we end up with a variation of the action integral for a charged particle in an electromagnetic field

$$\delta S = \delta \int_{t_1}^{t_2} \left( \frac{1}{2} m v^2 - e(\phi - \mathbf{v} \cdot \mathbf{A}) \right) dt = 0 . \quad (2.8)$$

The integrand in the above equation minimizes the action and is the Lagrangian for a particle in an electromagnetic field, namely,

$$\mathcal{L}(\mathbf{x}, \mathbf{v}, t) = \frac{1}{2} m v^2 + e\mathbf{v} \cdot \mathbf{A} - e\phi . \quad (2.9)$$

If we express the Lagrangian in terms of the generalized coordinates, we have

$$\mathcal{L}(q^i, \dot{q}^i, t) = \frac{1}{2}m\dot{q}^i\dot{q}_i + e\dot{q}^i A_i - e\phi, \quad (2.10)$$

where  $\mathbf{q} \doteq q^i$  and  $\dot{\mathbf{q}} \doteq \dot{q}^i$  are the generalized position and velocity vector components. Also,  $\mathbf{A} \doteq \eta^{ij}A_j$  where  $A_j$  is the contravariant component that is related to the vector component via the metric  $\eta_{ij}$  for the Cartesian coordinates.

The canonical momentum is needed when developing Hamiltonian mechanics and is useful when considering conserved quantities. Canonical momentum can be obtained from the Lagrangian by

$$\mathcal{P}^i = \frac{\partial \mathcal{L}}{\partial \dot{q}^i} = p^i + eA^i, \quad (2.11)$$

where  $p^i = m\dot{q}^i$  is the particle (linear/angular) momentum. The canonical momentum differs from the particle momentum when a non-conservative field, like the magnetic field, is involved.

### 2.1.2 Hamiltonian for a Particle in Electromagnetic Field

The Hamiltonian of a system is obtained from the Lagrangian via a Legendre transform (Landau and Lifshitz, 1976). The Legendre transform of the Lagrangian maps  $(q^i, \dot{q}^i) \rightarrow (q^i, \mathcal{P}^i)$ ; therefore,

$$H(q^i, \mathcal{P}^i, t) = \mathcal{P}^i \dot{q}_i - \mathcal{L}(q^i, \dot{q}^i, t). \quad (2.12)$$

Using the Lagrangian from Eq. (2.10) and the canonical momentum from Eq. (2.11), the Hamiltonian for a particle in electromagnetic field comes out to be

$$H(q^i, \mathcal{P}^i, t) = \frac{1}{2m} (\mathcal{P}^i - eA^i) (\mathcal{P}_i - eA_i) + e\phi. \quad (2.13)$$

In the Hamiltonian formulation the equations of motion are given by Hamilton's equations

$$\dot{q}_i = \frac{\partial H}{\partial \mathcal{P}^i}, \quad \dot{\mathcal{P}}_i = -\frac{\partial H}{\partial q^i}, \quad (2.14)$$

which are first order differential equations in the variables  $(q^i, \mathcal{P}^i)$ .

Consider a function  $g = g(q^i, \mathcal{P}^i, t)$  of the generalized coordinate, canonical momenta, and time. The total time derivative of such a function, utilizing Hamilton's equations Eq. (2.14), is

$$\frac{dg}{dt} = \frac{\partial g}{\partial t} + \{H, g\} , \quad (2.15)$$

where the Poisson bracket can be expressed as

$$\{H, g\} = \frac{\partial H}{\partial \mathcal{P}^i} \eta^{ij} \frac{\partial g}{\partial q^j} + \frac{\partial H}{\partial q^i} \eta^{ij} \frac{\partial g}{\partial \mathcal{P}^j} . \quad (2.16)$$

Note that  $\eta^{ij}$  is the metric for the Cartesian coordinate.

### 2.1.3 Non-canonical Mechanics

We saw that the Hamiltonian can be obtained from the Lagrangian via a Legendre transform. We can rearrange Eq. (2.12) to get

$$\mathcal{L}(q^i, \dot{q}^i, t) = \mathcal{P}^i \dot{q}_i - H(q^i, \mathcal{P}^i, t) , \quad (2.17)$$

where recall that  $\mathcal{P}^i$  is the canonical momentum, see Eq. (2.11). We define a set of new variables  $z^\alpha = (x^i, p^i)$  that are not necessarily canonical variables. Note  $\alpha$  spans from 1 to  $2s$  where  $s$  is the number of coordinates needed to completely describe the position. For example, in non-relativistic mechanics, we let  $i = 1, 2, 3$  and  $i' = i + 3$ ; therefore,  $z^{\alpha=i} = x^i$  and  $z^{\alpha=i'} = p^i$ . Using the chain rule, we rewrite  $\dot{q}^i$  as

$$\dot{q}^i(z^\alpha) = \frac{\partial q^i}{\partial t} + \dot{z}^\alpha \frac{\partial q^i}{\partial z^\alpha} . \quad (2.18)$$

We insert this expression for  $\dot{q}^i(z^\alpha)$  into Eq. (2.17) to write the Lagrangian in terms of the variables  $z^\alpha$ , thus

$$\mathcal{L} = \Lambda_\alpha \dot{z}^\alpha - \mathcal{H} , \quad (2.19)$$



where

$$\Lambda_\alpha = \mathcal{P}^i \frac{\partial q_i}{\partial z^\alpha} \quad (2.20)$$

and

$$\mathcal{H} = H - \mathcal{P}^i \frac{\partial q_i}{\partial t} . \quad (2.21)$$

We now use the Euler-Lagrange equation in terms of the new variables  $z^\alpha$  and  $\dot{z}^\alpha$ , in order to obtain a new expression for the equations of motion (Cary and Brizard, 2009)

$$\frac{d}{dt} \left( \frac{\partial \mathcal{L}}{\partial \dot{z}^\alpha} \right) = \frac{\partial \mathcal{L}}{\partial z^\alpha} , \quad (2.22)$$

which becomes

$$\omega_{\alpha\beta} \frac{dz^\beta}{dt} = \frac{\partial \mathcal{H}}{\partial z^\alpha} + \frac{\partial \Lambda_\alpha}{\partial t} . \quad (2.23)$$

The symplectic form  $\omega_{\alpha\beta}$  is given by

$$\omega_{\alpha\beta} = \frac{\partial \Lambda_\beta}{\partial z^\alpha} - \frac{\partial \Lambda_\alpha}{\partial z^\beta} = \frac{\partial \mathcal{P}^i}{\partial z^\alpha} \frac{\partial q_i}{\partial z^\beta} - \frac{\partial \mathcal{P}^i}{\partial z^\beta} \frac{\partial q_i}{\partial z^\alpha} . \quad (2.24)$$

Here  $\beta$  spans the same indices as  $\alpha$ . Note that the symplectic form is an expansion of the Poisson bracket. We invert the symplectic form to get a more convenient equations of motion

$$\frac{dz^\alpha}{dt} = \omega^{\alpha\beta} \left( \frac{\partial \mathcal{H}}{\partial z^\beta} + \frac{\partial \Lambda_\beta}{\partial t} \right) = \omega^{\alpha\beta} \left( \frac{\partial H}{\partial z^\beta} + \frac{\partial \mathcal{P}^i}{\partial t} \frac{\partial q_i}{\partial z^\beta} - \frac{\partial q_i}{\partial t} \frac{\partial \mathcal{P}^i}{\partial z^\beta} \right) , \quad (2.25)$$

where the last expression is in terms of the original Hamiltonian  $H$  and the canonical variables  $q^i$  and  $\mathcal{P}^i$ . The tensor  $\omega^{\alpha\beta}$  is called the inverse symplectic form. Note that it is usually easier to compute the symplectic form and then invert it to obtain the inverse symplectic form. Thus, using Eq. (2.25), we can construct the equations of motion even though  $z^\alpha$  may not consist of canonical coordinates. This new expression for the equations of motion (see Eq. (2.25)) reduces to Hamilton's equations when  $z^\alpha$  consists of canonical variables

$$\frac{dz^\alpha}{dt} = \sigma^{\alpha\beta} \frac{\partial H}{\partial z^\beta} \equiv \{z^\alpha, H\} , \quad (2.26)$$

where  $\{, \}$  is the Poisson bracket and  $\sigma^{\alpha\beta}$  is the fundamental (inverse) symplectic form

$$\sigma^{\alpha\beta} \doteq \begin{pmatrix} 0 & \eta^{ij} \\ -\eta^{ij} & 0 \end{pmatrix}. \quad (2.27)$$

Notice that  $\sigma^{\alpha\beta}$  is in block matrix form. In terms of the Poisson bracket, the fundamental symplectic form can be expressed as

$$\{z^\alpha, z^\beta\} = \sigma^{\alpha\beta} \quad \text{or} \quad \{q^i, \mathcal{P}^i\} = \eta^{ij} \quad (2.28)$$

### Particle in Magnetic Field

For a particle in a magnetic field, recall that the canonical momentum is given by

$$\mathcal{P}^i = p^i + eA^i.$$

Using the symplectic form in Eq. (2.24) for the non-canonical variables  $z^\alpha = (x^i, p^i)$ , particle position and momentum, come out to be

$$\omega_{\alpha\beta} \doteq \begin{pmatrix} eF_{ij} & -\eta_{ij} \\ \eta_{ij} & 0 \end{pmatrix}, \quad (2.29)$$

where  $F_{ij}$  is the spatial part of the Faraday tensor

$$F_{ij} = \frac{\partial A_j}{\partial x^i} - \frac{\partial A_i}{\partial x^j} = \varepsilon_{ijk} B^k. \quad (2.30)$$

Inverting the above expression gives us the inverse symplectic form for a particle in magnetic field

$$\omega^{\alpha\beta} \doteq \begin{pmatrix} 0 & \eta^{ij} \\ -\eta^{ij} & eF^{ij} \end{pmatrix}. \quad (2.31)$$

To obtain the equations of motion we first rewrite the Hamiltonian given in Eq. (2.13) in terms of the new, non-canonical variables,  $x^i$  and  $p^i$ , thus

$$H(x^i, p^i, t) = \frac{1}{2m} p^i p_i + e\phi, \quad (2.32)$$

where the expression for the canonical momentum (see Eq. (2.11)) was used. Hence, by evaluating each term (for details on calculating each term, see Appendix B) in Eq. (2.22), we can obtain the equations of motion we started out with in the beginning in Eq. (2.2), namely,

$$\frac{d\mathbf{p}}{dt} = e(\mathbf{E} + \dot{\mathbf{x}} \times \mathbf{B})$$

where  $\dot{\mathbf{x}} = \mathbf{v}$  and  $\mathbf{p} = m\mathbf{v}$ . Recall that the Lorenz gauge was used to write the potentials in terms of electric and magnetic fields.

## 2.2 Classical Statistical Mechanics

A classical system consisting of  $N$  interacting dimensionless point particles has  $3N$  degrees of freedom, where three coordinates are sufficient to describe the position of each particle. To fully determine the state of such a system, the position  $(q_1, q_2, \dots, q_{3N})$  and the velocity  $(\dot{q}_1, \dot{q}_2, \dots, \dot{q}_{3N})$  of every particle in the system needs to be known. The subsequent motion of all the particles is determined by the equations of motion. Such an approach is not feasible nor wise since the microscopic fluctuations from each particle motion cannot be measured experimentally. Experimentally, only the macroscopic quantities such as temperature, pressure, volume, *etc.*, are known. This leads to statistical averaging over an ensemble of isolated microscopic systems, each with the same macroscopic quantities.

In order to formulate the  $N$  particle system's dynamical state, we construct a  $6N$  dimensional space called the phase space. Typically, phase space is specified by  $3N$  spatial coordinates  $(q_1, q_2, \dots, q_{3N})$  and their corresponding  $3N$  particle momenta  $(p_1, p_2, \dots, p_{3N})$ . Together they yield a point, which we call a phase point, in the  $6N$  dimensional phase space. Hence, a phase point in phase space completely specifies the dynamics of the microscopic

state for the  $N$  particle system. A great number of microscopically distinct systems results in a “cloud” of phase points all with the same macroscopic variables. Letting the number of members in the ensemble approach infinity permits treating the cloud as a continuous distribution of phase points in phase space. This is denoted by the  $N$ -particle distribution  $f_N(q_1, \dots, q_{3N}, p_1, \dots, p_{3N}, t)$ , which when integrated over all phase space gives the total number of particles

$$\int f_N(q_1, \dots, q_{3N}, p_1, \dots, p_{3N}, t) d^{3N}q d^{3N}p = N . \quad (2.33)$$

The collection of phase points flows through the phase space like an incompressible fluid. That is, the phase points in any infinitesimal volume will be the same after some time  $dt$ ,

$$\begin{aligned} f_N(q_1, \dots, q_{3N}, p_1, \dots, p_{3N}, t) \\ = f_N(q_1 + \dot{q}_1 dt, \dots, q_{3N} + \dot{q}_{3N} dt, p_1 + \dot{p}_1 dt, \dots, p_{3N} + \dot{p}_{3N} dt, t + dt) . \end{aligned} \quad (2.34)$$

If we expand the right side in terms of the small time interval  $dt$  and neglect terms  $\mathcal{O}(dt^2)$  or higher, we end up with the Liouville equation

$$\frac{\partial f_N}{\partial t} + \sum_{j=1}^{3N} \dot{q}_j \frac{\partial f_N}{\partial q_j} + \sum_{j=1}^{3N} \dot{p}_j \frac{\partial f_N}{\partial p_j} = 0 . \quad (2.35)$$

The above expression is sufficient if the particle momentum is the same as the canonical momentum, which is true for a free particle. In this case, we can express it in terms of the Poisson bracket (see Eq. (2.16))

$$\frac{\partial f_N}{\partial t} + \{f_N, H\} = 0 . \quad (2.36)$$

Since each of the isolated phase points, *i.e.* microscopic states, obeys Hamilton’s equations, the distribution of phase points obeys the  $6N$  Hamilton’s equations of motion thereby, conserving the phase space volume (McQuarrie, 2000).

If a magnetic field is present, for example, the particle and canonical momenta are no longer the same. For this case, we will use the non-canonical formulation to rewrite Eq. (2.35). First, let  $z^\alpha = (x^i, p^i)$  where  $i = 1, 2, 3$  represents the vector components and  $\alpha$  represents both of the vector components, meaning  $\alpha = i$  for  $\mathbf{x}$  and  $\alpha = i'$  for  $\mathbf{p}$  where  $i' = i + 3$ . This lets us conveniently write the Liouville's equation in terms of the non-canonical coordinates

$$\frac{\partial f_N}{\partial t} + \sum_{j=1}^N \frac{\partial f_N}{\partial (z_j)^\alpha} \frac{d(z_j)^\alpha}{dt} = 0, \quad (2.37)$$

where recall that  $\dot{z}^\alpha$  are the equations of motion for the non-canonical formulation (see Eq. (2.25)). Here, summation over  $N$  particles is indicated by the index  $j$ . The repeating indices  $\alpha$  are summed over. If we expand the above expression using Eq. (2.25), we can write it in terms of the Poisson bracket and the time-dependent transformation part

$$\frac{\partial f_N}{\partial t} + \{f_N, H\} + \sum_{j=1}^N \left( \frac{\partial f_N}{\partial (z_j)^\alpha} \omega^{\alpha\beta} \frac{\partial \mathcal{P}^i}{\partial t} \frac{\partial q_i}{\partial (z_j)^\beta} - \frac{\partial f_N}{\partial (z_j)^\alpha} \omega^{\alpha\beta} \frac{\partial \mathcal{P}^i}{\partial (z_j)^\beta} \frac{\partial q_i}{\partial t} \right) = 0, \quad (2.38)$$

where  $\{, \}$  is the general Poisson bracket written in terms of the inverse symplectic form  $\omega^{\alpha\beta}$ ,

$$\{f_N, H\} = \frac{\partial f_N}{\partial (z_j)^\alpha} \omega^{\alpha\beta} \frac{\partial H}{\partial (z_j)^\beta}. \quad (2.39)$$

Therefore, if we have a time-independent transformation, the term inside the parentheses vanishes giving us a form similar to Eq. (2.36). Although, for example, if there is a magnetic field present, then the  $\partial q^i / \partial t$  term vanishes but the  $\partial \mathcal{P}^i / \partial t$  term remains due to the time dependence in the vector potential. Note that Eq. (2.36) holds even for the non-canonical particle momentum for a particle in uniform static electric and magnetic fields since the time derivatives of the fields vanish. If the spatial and temporal dependence of the fields is kept, the Liouville's equation needs to be expanded to include these effects when using particle momenta as one of the phase space coordinates.

The Liouville equation in the non-canonical form (see Eq. (2.37)) reduces to a simple, familiar form when considering non-relativistic particles in Cartesian coordinates

$$\frac{\partial f_N}{\partial t} + \sum_{j=1}^N \frac{\mathbf{p}_j}{m_j} \cdot \nabla_{\mathbf{x}_j} f_N + \sum_{j=1}^N \mathbf{F}_j \cdot \nabla_{\mathbf{p}_j} f_N = 0 . \quad (2.40)$$

Here we have used the vector notation with the phase space coordinate  $(\mathbf{x}_j, \mathbf{p}_j)$  for the  $j$ th particle. In the above expression,  $\nabla_{\mathbf{x}_j}$  is the gradient with respect to the spatial coordinates and  $\nabla_{\mathbf{p}_j}$  is the gradient with respect to the  $j$ th particle momentum. The quantity  $\mathbf{F}_j$  is the total force on the  $j$ th particle.

### 2.2.1 Single Particle Distribution Function

As stated at the beginning of this section, tracking the dynamical behavior of all  $N$  particles is unnecessary. The quantities that can be measured experimentally, such as temperature, pressure, volume, etc., are macroscopic quantities that only require one or two particle distribution functions. Fortunately, most macroscopic quantities in a plasma can be described by the first two reduced distribution functions (Harris, 2004). To a good approximation, the total internal force can often be modeled via the sum of pair-wise forces between two particles  $i$  and  $j$ , namely  $\mathbf{F}_{ij} \equiv \mathbf{F}(\mathbf{x}_i, \mathbf{x}_j)$ . We define the reduced distribution function as

$$f^{(n)}(\mathbf{x}_1, \dots, \mathbf{x}_n, \mathbf{p}_1, \dots, \mathbf{p}_n, t) \equiv \int f_N(\mathbf{x}_1, \dots, \mathbf{x}_N, \mathbf{p}_1, \dots, \mathbf{p}_N, t) d\Gamma_{n+1} , \quad (2.41)$$

where  $d\Gamma \equiv d\mathbf{x}_1 \dots d\mathbf{x}_N d\mathbf{p}_1 \dots d\mathbf{p}_N$  and  $d\Gamma_{n+1} \equiv d\mathbf{x}_{n+1} \dots d\mathbf{x}_N d\mathbf{p}_{n+1} \dots d\mathbf{p}_N$ . This reduces the  $N$  particle distribution function to  $n$  particle distribution function by integrating over the coordinates of the  $n+1^{\text{st}}$  to  $N^{\text{th}}$  particles. We can think of the reduced distribution function as giving the expectation value of finding any of the  $N$  particles in one of the  $d\Gamma_n$  volume elements.

We want to reduce the Liouville equation to that of a single particle distribution function. First, we note that the force that appears in Eq. (2.40) can be broken up into the sum

of pair-wise inter-particle forces  $\mathbf{F}_{ij}$ , and an external force  $\mathbf{F}_j^{(\text{ext})}$ ; hence

$$\int \left( \frac{\partial f_N}{\partial t} + \sum_{i=1}^N \frac{\mathbf{p}_i}{m} \cdot \nabla_{\mathbf{x}_i} f_N + \sum_{i=1}^N \left( \mathbf{F}_i^{(\text{ext})} + \sum_{j=1}^N \mathbf{F}_{ij} \right) \cdot \nabla_{\mathbf{p}_i} f_N \right) d\Gamma_{R+1} = 0. \quad (2.42)$$

When performing the integral, we need to keep in mind that the surface integral that appears vanishes after integration by parts when integrating over all phase space. This is because: (i) particles cannot have infinite momentum, and (ii) spatially, the boundary can be extended beyond the limit of the volume occupied by the system, thus the probability of finding a particle outside that volume is zero. Also, we can break up the integrals into particles being integrated over, *i.e.*  $n + 1$  to  $N$  particles, and those that are not integrated over, *i.e.* 1 to  $n$  particles. Finally, we let the inter-particle force be represented via the gradient of a potential, namely

$$\mathbf{F}_{ij} = - \sum_{i=1}^N \sum_{j=1}^N \nabla_{\mathbf{x}_i} \phi_{ij}, \quad (2.43)$$

where the potential  $\phi_{ij}$  is a function of the distance between the two particles  $i$  and  $j$ ,  $r_{ij} = |\mathbf{x}_i - \mathbf{x}_j|$ . In the case of a fully ionized plasma,  $\phi_{ij}$  is the Coulomb potential between two charged particles. After careful integration of each of the terms, we get

$$\begin{aligned} \frac{\partial f^{(n)}}{\partial t} + \sum_{i=1}^n \frac{\mathbf{p}_i}{m} \cdot \nabla_{\mathbf{x}_i} f^{(n)} + \sum_{i=1}^n \mathbf{F}_i^{(\text{ext})} \cdot \nabla_{\mathbf{p}_i} f^{(n)} - \sum_{i,j=1}^n \nabla_{\mathbf{x}_i} \phi_{ij} \cdot \nabla_{\mathbf{p}_i} f^{(n)} \\ = (N - n) \int \int \sum_{i=1}^n \nabla_{\mathbf{x}_i} \phi_{i,n+1} \cdot \nabla_{\mathbf{p}_i} f^{(n+1)} d\mathbf{x}_{n+1} d\mathbf{p}_{n+1}. \end{aligned} \quad (2.44)$$

This is the BBGKY (Bogoliubov, Born, Green, Kirkwood, Yvon) hierarchy that gives the time evolution of the reduced distribution function  $f^{(n)}$ . Note that on the right of the above equation, the  $f^{(n+1)}$  term appears. This indicates that this equation is not closed. The time evolution for  $f^{(n)}$  requires the  $f^{(n+1)}$  distribution. Equation (2.44) was obtained by assuming that the distribution function is symmetric when permuting the particles. This reduces the  $N-n$  interactions to interactions with just the  $n + 1$  particle. With  $n = 1$ , we

get the time evolution equation for the single particle distribution function  $f \equiv f^{(1)}$ ,

$$\frac{\partial f}{\partial t} + \frac{\mathbf{p}}{m} \cdot \nabla f + \mathbf{F} \cdot \nabla_p f = (N-1) \int \int \nabla \phi_{12} \cdot \nabla_p f^{(2)} d\mathbf{x}_2 d\mathbf{p}_2. \quad (2.45)$$

For the case of no self interaction,  $\phi_{ii} = 0$ , the fourth term in Eq. (2.44) vanishes for the single particle distribution function. Note that for simplicity, we have  $\nabla_{x_1} \equiv \nabla$ ,  $\nabla_{p_1} \equiv \nabla_p$ , and  $\mathbf{F}_1^{(\text{ext})} \equiv \mathbf{F}$  in the above expression. The right side of Eq. (2.45) is the particle interaction term, commonly called the collision term. The left side is the “streaming” term that is governed by the external force. The single particle distribution function gives the expectation value of any of the  $N$  particles having location  $\mathbf{x}$  with momentum  $\mathbf{p}$  at time  $t$  in the phase space volume element  $d\mathbf{x}d\mathbf{p}$ .

In order to close the time evolution equation for the distribution (single particle distribution) function, we need to “close” for the  $f^{(2)}$  dependence. The approach that Boltzmann took (Boltzmann, 1970) was to express the collisional term on the right side of Eq. (2.45) in terms of the product of  $f_i$  and  $f_j$ , the single particle distribution function for species  $i$  and  $j$ . This assumes that the particle position and velocities are uncorrelated, *i.e.* the molecular chaos assumption or *Stosszahlansatz*. Effectively, it only considers short ranged binary interactions between species  $i$  and  $j$ . The Boltzmann equation is not considered further in this thesis. A brute force approach to closure is to completely neglect the collision term and just have the streaming term. This leads us to the Vlasov equation used in modeling collisionless plasmas.

### 2.2.2 The Vlasov Equation

In the Vlasov equation, it is assumed that the effect of collisions is negligible; hence we ignore the two-particle correlation in Eq. (2.45). We will apply this collisionless limit to the energetic particles in the hybrid kinetic-MHD model. In the hybrid model, the energetic particles are fast enough that they do not “see” the bare Coulomb potential of the particles in the bulk MHD plasma. This holds so long as the collision time scale is much longer than the streaming and MHD time scales of interest. Note that from here on we will



express the distribution function in velocity space instead of momentum space  $f(\mathbf{x}, \mathbf{v}, t)$ . For non-relativistic, classical particles, this gives equivalent results.

For the purpose of building some physical intuition, we again consider the  $N$ -particle distribution function. We return to the Liouville's equation (see Eq. (2.40)) written as

$$\left\langle \frac{\partial f_N}{\partial t} + \sum_{j=1}^N \mathbf{v}_j \cdot \nabla_{x_j} f_N + \sum_{j=1}^N \mathbf{a}_j \cdot \nabla_{v_j} f_N \right\rangle = 0 \quad (2.46)$$

where we now use velocities and the angle brackets to indicate the reduction to the single particle distribution function. The difficulty here, as we saw previously, was the acceleration term. For example, if we were to consider the Lorentz force, the exact electromagnetic field depends on the particle trajectories; thus, the fields are not statistically independent of  $f_N$ , meaning

$$\langle \mathbf{a}_j \cdot \nabla_{v_j} f_N \rangle \neq \langle \mathbf{a}_j \rangle \cdot \langle \nabla_{v_j} f_N \rangle . \quad (2.47)$$

We end up with a correlation term with collisions accounting for the missing part of Eq. (2.47). This lets us write

$$\langle \mathbf{a}_j \cdot \nabla_{v_j} f_N \rangle = \langle \mathbf{a}_j \rangle \cdot \langle \nabla_{v_j} f_N \rangle - C(f) . \quad (2.48)$$

Therefore, when we say there are no collisions, we are assuming that the electromagnetic field and the distribution function are statistically independent of each other. This means that the averaged out  $N$  particle distribution function (that appears as a mist in phase space) is influenced only by the averaged fields. Unlike the case with collisions, where each particle may, occasionally, feel a sharp change of the field from the mean that could cause the particle to depart from the streaming motion.

We now carefully consider the Lorentz force,  $\mathbf{F}_j = q(\mathbf{E}(\mathbf{x}, t) + \mathbf{v}_j \times \mathbf{B}(\mathbf{x}, t))$ , in the BBGKY reduction process. Recall that the fields considered are the averaged macroscopic quantities since we are neglecting collisions. Thus no statistical correlation between the fields and the particle trajectories is considered. Therefore, the third term in Eq. (2.46)

with the Lorentz force comes out to be

$$\left\langle \sum_{j=1}^N \frac{q}{m} (\mathbf{E} + \mathbf{v}_j \times \mathbf{B}) \cdot \nabla_{v_j} f_N \right\rangle = \int \left[ \frac{q}{m} (\mathbf{E} + \mathbf{v}_1 \times \mathbf{B}) \cdot \nabla_{v_1} f_N \right] d\Gamma_2 + \int \sum_{j=2}^N \left[ \frac{q}{m} (\mathbf{E} + \mathbf{v}_j \times \mathbf{B}) \cdot \nabla_{v_j} f_N \right] d\Gamma_2, \quad (2.49)$$

where  $d\Gamma_2 = d\mathbf{x}_2 \dots d\mathbf{x}_N d\mathbf{v}_2 \dots d\mathbf{v}_N$ . The operator in the first expression on the right side comes out of the integral because the integration is over particles 2 to  $N$ . Using the definition of reduced distribution function (see Eq. (2.41)), we end up with the operator simply acting on the single particle distribution function

$$\int \left[ \frac{q}{m} (\mathbf{E} + \mathbf{v}_1 \times \mathbf{B}) \cdot \nabla_{v_1} f_N \right] d\Gamma_2 = \frac{q}{m} (\mathbf{E} + \mathbf{v}_1 \times \mathbf{B}) \cdot \nabla_{v_1} f^{(1)}.$$

The second expression in Eq. (2.49) requires more careful consideration. Note that we can rewrite the integrand as the divergence of the whole quantity by using the following reasoning: (i)  $\nabla_{v_j} \cdot (f_N \mathbf{E}) = \mathbf{E} \cdot \nabla_{v_j} f_N$  because  $\nabla_{v_j} \cdot \mathbf{E} = 0$  since the electric field is only a function of the spatial coordinates and (ii)  $\nabla_{v_j} \cdot (\mathbf{v}_j \times \mathbf{B}) = 0$  because  $\nabla_{v_j} \times \mathbf{B} = 0$  and  $\nabla_{v_j} \times \mathbf{v}_j = 0$ . This allows us to write for the second term

$$\int \sum_{j=2}^N \left[ \frac{q}{m} (\mathbf{E} + \mathbf{v}_j \times \mathbf{B}) \cdot \nabla_{v_j} f_N \right] d\Gamma_2 = \int \sum_{j=2}^N \nabla_{v_j} \cdot \left[ \frac{q}{m} (\mathbf{E} + \mathbf{v}_j \times \mathbf{B}) f_N \right] d\Gamma_2.$$

Using Gauss's theorem, we can rewrite the the above expression in terms of a surface integral that vanishes since particles cannot exist at infinity and have an infinite velocity, meaning the  $N$  particle distribution function approaches zero as the surface is moved out to infinity. Therefore, the second term on the right side of Eq. (2.49) vanishes

$$\int \sum_{j=2}^N \left[ \frac{q}{m} (\mathbf{E} + \mathbf{v}_j \times \mathbf{B}) \cdot \nabla_{v_j} f_N \right] d\Gamma_2 = 0.$$

Thus, we have shown that the average fields vanish for particles 2 to  $N$  in the BBGKY reduction to the single particle distribution function. This again yields the Vlasov equation

$$\frac{\partial f}{\partial t} + \mathbf{v} \cdot \nabla f + \frac{q}{m} (\mathbf{E} + \mathbf{v} \times \mathbf{B}) \cdot \nabla_v f = 0 , \quad (2.50)$$

where the subscript 1 has been dropped and  $f \equiv f^{(1)}$  as before.

The average electromagnetic fields are governed by Maxwell's equations

$$\begin{aligned} \nabla \cdot \mathbf{E} &= \frac{\rho_c}{\epsilon_0} , & \nabla \times \mathbf{E} &= -\frac{\partial \mathbf{B}}{\partial t} , \\ \nabla \cdot \mathbf{B} &= 0 , & \nabla \times \mathbf{B} &= \mu_0 \mathbf{J} + \mu_0 \epsilon_0 \frac{\partial \mathbf{E}}{\partial t} . \end{aligned} \quad (2.51)$$

Often in plasma physics, the displacement current  $\mu_0 \epsilon_0 \partial \mathbf{E} / \partial t$  is neglected. In order to solve for the fields via the Maxwell's equations, the sources, charge  $\rho_c$  and current  $\mathbf{J}$  densities, must be known. These sources are related to the distribution function via the moments

$$\rho_c(\mathbf{x}, t) = q \int f(\mathbf{x}, \mathbf{v}, t) d\mathbf{v} \quad (2.52)$$

and

$$\mathbf{J}(\mathbf{x}, t) = q \int \mathbf{v} f(\mathbf{x}, \mathbf{v}, t) d\mathbf{v} . \quad (2.53)$$

Therefore, the evolution of the distribution function is governed by the given fields, which are governed by Maxwell's equations. Given sources that are appropriately specified via the distribution function, this together with the assumption that collisions are negligible, provides closure to Maxwell equations.

### 2.2.3 The Drift Kinetic Equation

In devices such as tokamaks, where the plasma is strongly magnetized, the guiding center drift is heavily characterized by a motion along the magnetic field  $\mathbf{B}$ . Drifts such as  $E \times B$ , magnetic field gradient, and curvature drifts are first-order terms in the guiding center motion of a particle. These first order terms are significant in a tokamak and give rise

to interesting physics due to the complex magnetic geometry. Magnetized plasmas satisfy the condition that the gyro-radius  $\rho$  is much smaller than plasma scale lengths  $L$  and the period of gyro-motion  $\Omega^{-1}$  is much shorter than streaming and MHD timescales  $\omega^{-1}$ . The condition for plasma to be magnetized is indicated by the parameter  $\delta$  that is defined as

$$\delta \equiv \frac{\rho}{L} \sim \frac{\omega}{\Omega} \sim \frac{\omega}{(qB/m)}. \quad (2.54)$$

If  $\delta \sim 1$ , the plasma is no longer strongly magnetized and the drift ordering cannot be applied. For magnetized plasmas, the drift ordering forbids the rapid time variation of the fields and considers only the slowly varying part of the distribution function by suppressing the rapid gyro-motion. Averaging over the short length and time scales of gyro-motion still allows the drift kinetic equation to describe phenomena such as confined plasma equilibrium, transport processes, and various plasma instabilities (Hazeltine and Meiss, 2003), making it a powerful tool for analyzing magnetized plasmas.

The guiding center velocity in the drift kinetic regime, which will be derived later in Chapter 3, can be expressed as

$$\mathbf{v}_{\text{gc}} = v_{\parallel} \mathbf{b} + \frac{\mathbf{E} \times \mathbf{B}}{B^2} + \frac{1}{\Omega} \mathbf{b} \times \left( v_{\parallel} \frac{\partial \mathbf{b}}{\partial t} + v_{\parallel}^2 \boldsymbol{\kappa} + \frac{v_{\perp}^2}{2} \frac{\nabla B}{B} \right), \quad (2.55)$$

where  $\mathbf{b} = \mathbf{B}/B$  is the unit vector along the local magnetic field and  $\boldsymbol{\kappa}$  is the magnetic curvature vector. Note that the magnetic curvature can be expressed in terms of the current density

$$\boldsymbol{\kappa} = \mathbf{b} \cdot \nabla \mathbf{b} = \mu_0 \frac{\mathbf{J} \times \mathbf{B}}{B^2} + \frac{1}{B} \nabla_{\perp} B, \quad (2.56)$$

where  $\nabla_{\perp} = \nabla - \nabla_{\parallel}$  is the component of the gradient that is perpendicular to the magnetic field and we have used the pre-Maxwell form of Ampere's law. Note that Eq. (2.56) will be used later when considering the  $\delta f$  implementation in NIMROD. This is because the current density and the magnetic field are more readily available in NIMROD than the magnetic curvature.

Gyro-averaging allows the plasma kinetic equation to be cast into a drift kinetic equation with the lowest order distribution function only depending on the position and the energy. A few subtle approximations are used for the magnetic moment,  $\mu = mv_{\perp}^2$ , when deriving the lowest order drift kinetic equation. The main idea is that the quantity  $d\mu/dt$  is small compared to other terms and that the lowest order distribution function is dependent only on the position and the energy [Hazeltine and Meiss \(2003\)](#). The result is

$$\frac{\partial f}{\partial t} + \mathbf{v}_{\text{gc}} \cdot \nabla f + \frac{dU}{dt} \frac{\partial f}{\partial U} = C(f) , \quad (2.57)$$

where  $U$  is the total energy. This allows the distribution function  $f(\mathbf{x}, U, \mu, t)$  to be expressed in terms of five degrees of freedom  $\mathbf{x}$ ,  $U$ , and  $\mu$ , instead of the usual six dimensions of phase space. The above drift kinetic equation can be written in terms of the kinetic energy  $w = mv^2/2$  instead of the total energy  $U$  as

$$\frac{\partial f}{\partial t} + (\mathbf{v}_{\parallel} + \mathbf{v}_D) \cdot \nabla f + \left( \mu \frac{\partial B}{\partial t} + e(\mathbf{v}_{\parallel} + \mathbf{v}_D) \cdot \mathbf{E} \right) \frac{\partial f}{\partial w} = C(f) . \quad (2.58)$$

Note that  $\mathbf{v}_{\parallel} = v_{\parallel} \mathbf{b}$  is the parallel streaming term along the magnetic field and  $\mathbf{v}_D$  is the drift portion of the guiding center velocity, hence  $\mathbf{v}_{\text{gc}} = \mathbf{v}_{\parallel} + \mathbf{v}_D$ . Equation (2.58) is the first-order approximation to the kinetic equation. Assuming that the collisions are negligible, *i.e.* set the right side to zero, yields the Vlasov form for the drift kinetic equation. The form of the drift kinetic equation given in Eq. (2.58) is the most common form. For a more detailed discussion see [Hazeltine and Meiss \(2003\)](#).

### 2.3 Axisymmetric Magnetic Field Configuration

The magnetic field configuration of tokamaks is complex, hence difficult to consider analytically. When analyzing particle motion it is easiest to consider a large aspect ratio tokamak with circular poloidal cross section. The aspect ratio is given by the major radius

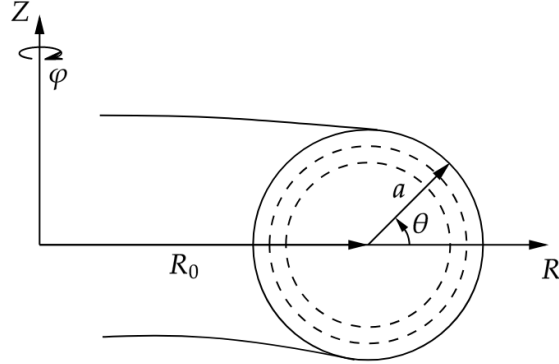


**Figure 2.1:** The major radius  $R_0$  points from the origin to the magnetic axis. The minor radius  $a$  is the radius of the last closed magnetic flux surface. The dotted line indicates flux surfaces that are within the minor radius. The angles  $\theta$  and  $\varphi$  are referred to as the poloidal and toroidal angles, respectively.

$R_0$  divided by the minor radius  $a$  (see 2.1)

$$A = \frac{R_0}{a} . \quad (2.59)$$

Analytical considerations benefit from the small limit of the inverse aspect ratio

$$\epsilon_a = \frac{a}{R_0} \ll 1 . \quad (2.60)$$

There are different regions in the tokamak confinement volume: (i) the confinement region  $r < a$ , a region of closed magnetic flux surfaces; (ii) separatrix,  $r = a$ , last closed flux surface; and (iii) the scrape-off layer (SOL),  $r > a$ , the region where magnetic field lines intersect the walls. Flux surfaces, defined as surfaces that are everywhere tangential to the magnetic field, are shown as the dashed and solid curves in 2.1. These surfaces extend toroidally from  $\varphi = 0$  to  $\varphi = 2\pi$ . Note that in the small aspect ratio limit, if  $a \ll R_0$  then automatically  $r \ll R_0$ , where  $r$  is the radius of a circular flux surface (see Fig. 2.1).

In toroidal plasma confinement devices, it is necessary to have a poloidal magnetic field as well. The toroidal and poloidal components of  $\mathbf{B}$  cause the magnetic field to twist around the tokamak allowing for particle confinement. It is useful to introduce the rotational

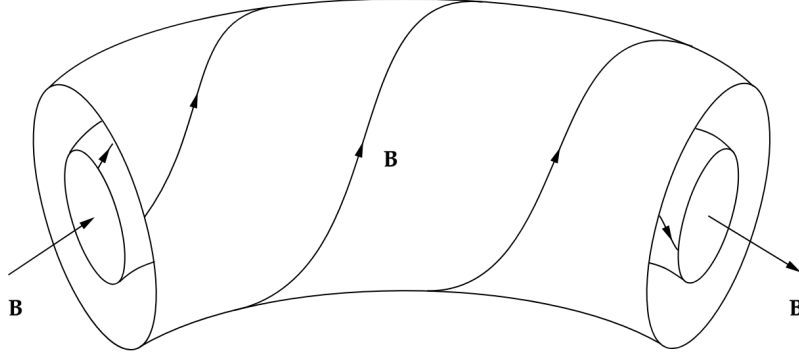


**Figure 2.2:** The helical magnetic field, due to the poloidal and toroidal components, wraps around the flux surfaces.

transform  $\iota$ , defined as the number of poloidal transits per toroidal transit (see Fig. 2.2).

The inverse of the rotational transform is the safety factor

$$q_s = \frac{1}{\iota}. \quad (2.61)$$

In a linear tokamak, *i.e.* periodic cylinder, the safety factor is given by the following expression

$$q_s = \frac{rB_t}{R_0B_p} \quad (2.62)$$

where  $B_t$  is the toroidal magnetic field and  $B_p$  is the poloidal magnetic field. Safety factors are important in toroidal confinement devices since low-order rotational surfaces,  $q_s = 1/1$ ,  $3/2$ ,  $2/1$ ,  $\dots$  are more susceptible to certain instabilities. In this thesis, we will be examining the effect of energetic particles on the linear growth rate of the ideal internal kink mode which resides at the  $q_s = 1/1$  surface.

### 2.3.1 Axisymmetric Toroidal Magnetic Field

Let us consider an axisymmetric toroidal magnetic field. Using the pre-Maxwell form of Ampere's law, we can find an expression for the toroidal magnetic field from

$$\nabla \times \mathbf{B}_t = \mu_0 \mathbf{J} \quad (2.63)$$

by integrating Ampere's law using Stoke's theorem. Here the current  $I$  is carried by toroidal field coils and integrating along an Amperian loop of radius  $R$  yields

$$\mathbf{B}_t = \frac{\mu_0 N_\ell I}{2\pi R} \hat{\varphi} , \quad (2.64)$$

where  $N_\ell$  is the number of coil turns with  $I_{\text{tot}} = N_\ell I$ . Since the toroidal magnetic field is proportional to  $1/R$ , we may express it as

$$B_t = \frac{B_0 R_0}{R} = \frac{B_0 R_0}{R_0 + r \cos \theta} \quad (2.65)$$

where  $B_0$  is the magnetic field strength at the magnetic axis. For the second expression, we have expressed  $R$  in terms of the poloidal variables  $(r, \theta)$ . In the large aspect ratio limit, we can further simplify the expression for  $B_t$  by using the inverse aspect ratio,  $\epsilon = r/R_0$ ,

$$B_t = B_0 (1 + \epsilon \cos \theta)^{-1} \approx B_0 (1 - \epsilon \cos \theta) . \quad (2.66)$$

We see from the expression of the toroidal magnetic field that the gradient of the magnetic field points radially inward. This radially inward gradient of the magnetic field causes a drift that points perpendicular to  $\nabla B_t$  and  $\mathbf{B}_t$ . This causes a drift that is up (ions) or down (electrons) in the  $Z$ -direction. Due to the curvature in the toroidal magnetic field, the particles also experience a curvature drift (often thought of as a drift due to a centrifugal force) perpendicular to the  $R$ -direction and  $\mathbf{B}_t$ . This drift is also up (ions) or down (electrons) along the  $Z$ -direction. The drift due to the gradient and curvature causes charge separation that leads to an electric field perpendicular to  $\mathbf{B}_t$ . The result is a rapid  $E \times B$  drift towards the wall of the tokamak, hence particles cannot be confined by the toroidal magnetic field only. The combined drift is

$$\mathbf{v}_D = \frac{\mathbf{E} \times \mathbf{B}}{B^2} + \frac{W_\perp}{qB} \frac{\mathbf{b} \times \nabla B}{B} + \frac{2W_\parallel}{qB} \frac{\mathbf{b} \times \hat{\mathbf{R}}_c}{R_c} , \quad (2.67)$$

where  $W_\parallel$  is the parallel and  $W_\perp$  the perpendicular particle kinetic energy ([Gurnett and](#)



[Bhattacharjee, 2017](#)). Note that this drift velocity is like Eq. (2.55) only written in terms of the parallel and perpendicular energy and the magnetic curvature vector,  $\hat{\mathbf{R}}_c$ .

In order to confine the plasma, the magnetic field must be twisted. In tokamaks, an axial current is induced to produce a poloidal magnetic field. Thus, a toroidal plasma current produces a poloidal magnetic field  $\mathbf{B}_p$  that is typically much smaller in magnitude than  $\mathbf{B}_t$ . An added benefit of the toroidal current is resistive (Joule) heating of the plasma. Unfortunately, gradients in the toroidal current are also a source of free energy that can drive instabilities like the 1/1 ideal internal kink mode.

CHAPTER 3  
SINGLE PARTICLE MOTION

### 3.1 Motion in a Static Uniform Magnetic Field

Fundamentally, the descriptions of plasma can be traced back to the motion of particles that form the plasma. We start by considering the most simple case of a charged particle in a static uniform magnetic field. Doing so will build intuition, which will help when constructing the guiding center motion of a charged particle. Later, we will treat the more difficult case of spatially and temporally varying fields.

A charged particle in a static uniform magnetic field obeys Newton's second law

$$m \frac{d\mathbf{v}}{dt} = q\mathbf{v} \times \mathbf{B} , \quad (3.1)$$

from which we can obtain an expression for the particle energy by dotting the equations of motion with the particle velocity

$$\frac{d}{dt} \left( \frac{1}{2} m v^2 \right) = 0 . \quad (3.2)$$

Thus, the kinetic energy in a static uniform magnetic field is conserved. When describing the particle motion in a magnetic field it is convenient to express the particle velocity in terms of the parallel and perpendicular components with respect to the magnetic field

$$\mathbf{v} = \mathbf{v}_{\parallel} + \mathbf{v}_{\perp} . \quad (3.3)$$

In doing so we can easily see that  $\mathbf{v}_{\parallel} \cdot (\mathbf{v} \times \mathbf{B}) = v_{\parallel} \mathbf{b} \cdot (\mathbf{v} \times \mathbf{B}) = 0$ , where  $\mathbf{b} = \mathbf{B}/B$ ; hence  $v_{\parallel}$  is constant. Since  $v$  and  $v_{\parallel}$  are constants,  $v_{\perp}$  must be a constant. Therefore, from the energy conservation we get a fundamental result, a charged particle in magnetic field performs a circular motion around the magnetic field line.

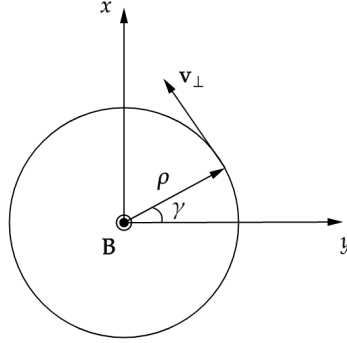


**Figure 3.1:** Gyro-motion in the plane perpendicular to the static uniform magnetic field where the magnetic field is pointing into the page.

In order to find the radius of the circular motion, the magnitude of the perpendicular component of Eq. (3.1) is considered. Note that since we have circular motion in the plane perpendicular to the magnetic field, the acceleration in this plane is the centripetal acceleration, thus we have the expression

$$\frac{mv_{\perp}^2}{\rho} = q|\mathbf{v}_{\perp} \times \mathbf{B}| .$$

From the definition of  $\mathbf{v}_{\perp}$ , we know it is always perpendicular to  $\mathbf{B}$ ; therefore, we solve for the gyro-radius, *i.e.* the radius of the circular motion,

$$\rho = \frac{mv_{\perp}}{qB} . \quad (3.4)$$

The periodic motion in the plane perpendicular to the magnetic field is expressed in vector form using the gyro-radius

$$\boldsymbol{\rho} = \rho (\sin \gamma \hat{\mathbf{x}} + \cos \gamma \hat{\mathbf{y}}) , \quad (3.5)$$

where the static uniform magnetic field was chosen to be in the  $z$ -direction,  $\mathbf{B} = B\hat{\mathbf{z}}$ , of a local Cartesian coordinate system. The angle  $\gamma$  is the gyro-angle that characterizes the

circular motion, see Fig. 3.1, where this angle is time-dependent,  $\gamma = \gamma(t)$ ; thus taking the total time derivative of  $\boldsymbol{\rho}$  gives us an expression for the perpendicular velocity

$$\dot{\boldsymbol{\rho}} = \mathbf{v}_{\perp} = v_{\perp} (\cos \gamma \hat{\mathbf{x}} - \sin \gamma \hat{\mathbf{y}}) , \quad (3.6)$$

where  $v_{\perp} = \rho \dot{\gamma}$ . Since the particle undergoes a circular motion, the characteristic frequency is constant; therefore, we let  $\dot{\gamma} = \Omega$ , the gyro-frequency, which by using Eq. (3.5), gives the form

$$\Omega = \frac{v_{\perp}}{\rho} = \frac{qB}{m} , \quad (3.7)$$

where  $B$  is the magnitude of the field. Later on, when studying non-uniform fields, this form for the gyro-frequency at the center of the gyro-motion becomes important. The vector form of the gyro-radius  $\boldsymbol{\rho}$  can be written in terms of  $\mathbf{v}_{\perp}$  and  $\mathbf{b}$ , where  $\mathbf{b}$  is the unit vector in the magnetic field direction,  $\mathbf{b} = \mathbf{B}/B$ . Note that if we cross  $\mathbf{b}$  into  $\mathbf{v}_{\perp}$ , this gives a vector in the direction of  $\boldsymbol{\rho}$ . This is because for a circular motion  $\mathbf{b}$ ,  $\boldsymbol{\rho}$ , and  $\mathbf{v}_{\perp}$  are all orthogonal to each other; hence, the gyro-radius can be expressed as

$$\boldsymbol{\rho} = \frac{\mathbf{b} \times \mathbf{v}_{\perp}}{\Omega} , \quad (3.8)$$

where the magnitude of this equation satisfies Eq. (3.5).

Finally, for the parallel motion of Eq. (3.1), there is no force acting on the particle in this direction; therefore, a particle with an initial parallel velocity,  $\mathbf{v}_{\parallel 0}$ , will maintain that velocity throughout the motion. The result is a helical motion about a magnetic field line

$$\mathbf{v} = v_{\parallel 0} \mathbf{b} + \rho \Omega (\cos \gamma \hat{\mathbf{x}} - \sin \gamma \hat{\mathbf{y}}) . \quad (3.9)$$

### 3.2 Magnetic Moment in Static Uniform Magnetic Field

As we saw above, a particle in a uniform magnetic field performs a circular gyro-motion about that field. This circular motion of the particle can be thought of as an infinitesimal

ring of current with charge  $q$ . Thus, the magnetic moment  $\mu$  can be defined as

$$\mu = IA = q \left( \frac{v_{\perp}}{2\pi\rho} \right) (\pi\rho^2) = \frac{1}{2}q\rho v_{\perp} .$$

Using the expression for the gyro-radius in Eq. (3.5) gives the result that will be used extensively, namely,

$$\mu = \frac{mv_{\perp}^2}{2B} . \quad (3.10)$$

The gyro-motion of electrons and ions leads to a diamagnetic effect, with the magnetic moment pointing in the opposite direction of the magnetic field. Hence, the magnetic moment vector can be expressed as

$$\boldsymbol{\mu} = -\mu\mathbf{b} . \quad (3.11)$$

### 3.3 Motion in Static Uniform Electric and Magnetic Fields

We now consider a charged particle in static uniform electric and magnetic fields. The particle's motion is governed by Newton's second law with the full Lorentz force

$$m\frac{d\mathbf{v}}{dt} = q(\mathbf{E} + \mathbf{v} \times \mathbf{B}) . \quad (3.12)$$

If we dot the above equation of motion with the particle velocity, like we did for the static magnetic field case, we end up with a kinetic energy evolution equation

$$\frac{d}{dt} \left( \frac{1}{2}mv^2 \right) = q\mathbf{v} \cdot \mathbf{E} , \quad (3.13)$$

thus the kinetic energy is no longer constant in time. The electric field does work on the particle, changing the particle's energy over time. In order to study the particle motion in this case, it is convenient to express Eq. (3.12) in terms of the parallel and perpendicular components to the magnetic field

$$m\frac{d\mathbf{v}_{\parallel}}{dt} = q\mathbf{E}_{\parallel} \quad (3.14)$$

and

$$m \frac{d\mathbf{v}_\perp}{dt} = q (\mathbf{E}_\perp + \mathbf{v}_\perp \times \mathbf{B}) . \quad (3.15)$$

When the parallel component of the equation of motion is integrated with static fields, we end up with the following expression for the parallel velocity

$$\mathbf{v}_\parallel (t) = v_{\parallel 0} \mathbf{b} + \frac{q\mathbf{E}_\parallel}{m} t . \quad (3.16)$$

Here the electric field parallel to the magnetic field accelerates the particle along the magnetic field line.

Now we consider the perpendicular component of the equations of motion. Consider an inertial reference frame moving with velocity  $\mathbf{v}_E$  with respect to the original frame

$$\mathbf{v}_E = \mathbf{v}_\perp - \mathbf{u} , \quad (3.17)$$

where  $\mathbf{u}$  is the particle velocity in the frame moving with  $\mathbf{v}_E$ . When we substitute the expression for the velocity above into the perpendicular equation of motion, Eq. (3.15), we end up with two separate equations because of the definition of  $\mathbf{v}_E$ , hence

$$m \frac{d\mathbf{v}_E}{dt} = q\mathbf{E}_\perp + q\mathbf{v}_E \times \mathbf{B} \quad (3.18)$$

and

$$\frac{d\mathbf{u}}{dt} = q\mathbf{u} \times \mathbf{B} . \quad (3.19)$$

Since  $\mathbf{v}_E$  is constant, the left side of Eq. (3.18) vanishes, and solving for  $\mathbf{v}_E$  yields the expression for the  $E \times B$  drift velocity

$$\mathbf{v}_E = \frac{\mathbf{E} \times \mathbf{B}}{B^2} , \quad (3.20)$$

which arises from the perpendicular (to  $\mathbf{B}$ ) component of the electric field. This drift does not depend on the particle charge, hence electrons and ions will drift in the same direction

across the magnetic field lines. Note that Eq. (3.19) will give the same result that was obtained above for a static uniform magnetic field. Thus, combining all the velocities, namely Eqs. (3.6), (3.16), and (3.20), we get

$$\mathbf{v}(t) = v_{\parallel 0} \mathbf{b} + \frac{q\mathbf{E}_{\parallel}}{m} t + \frac{\mathbf{E} \times \mathbf{B}}{B^2} + \rho\Omega (\cos \gamma \hat{\mathbf{x}} - \sin \gamma \hat{\mathbf{y}}) \quad (3.21)$$

for the particle velocity in static uniform electric and magnetic fields.

### 3.4 Motion in Slowly Varying Magnetic Field: Guiding Center Motion

If the magnetic field varies slowly in space and time, then the motion of the particles can overall be characterized by a drift motion. By slowly varying, we mean that the characteristic length  $\ell_B$  and time scale  $\tau_B$  of the magnetic field

$$\ell_B \sim \left| \frac{\nabla B}{B} \right|^{-1} \quad \text{and} \quad \tau_B \sim \left| \frac{1}{B} \frac{\partial B}{\partial t} \right|^{-1} \sim \omega_B^{-1} \quad (3.22)$$

are much larger than the gyro-radius and gyro-frequency

$$\frac{\rho}{\ell_B} \ll 1 \quad \text{and} \quad \Omega\tau_B \gg 1 \quad \text{or} \quad \frac{\omega_B}{\Omega} \ll 1. \quad (3.23)$$

In a magnetically confined plasma, such as those in tokamak devices, the above conditions for the magnetic field hold. Therefore, it is often sufficient to model the energetic particles using the drift motion. Gaining an insight into the transport of these energetic particles that can have significant effects on the bulk, fluid type, MHD plasma is paramount in understanding the behavior of a magnetically confined plasma.

#### 3.4.1 Gyro-frequency in Slowly Varying Magnetic Field

In a uniform magnetic field, we saw that the energy of the particle is conserved. This leads to circular motion with a constant characteristic frequency, namely the gyro-frequency  $\Omega = qB/m$ . Note that in a spatially non-uniform magnetic field, the energy is still conserved, although for time-dependent magnetic field it is not. Nevertheless, the characteristic

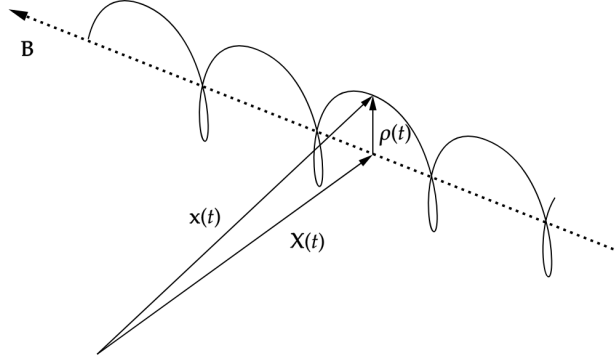


**Figure 3.2:** Guiding center motion, particle gyrating about the magnetic field line.

frequency is not constant due to the fact that it is dependent on the magnitude of the magnetic field, see Eq. (3.7). In Fig. 3.2 the relationship between the guiding center position  $\mathbf{X}$ , the gyro-radius  $\rho$ , and the actual position vector  $\mathbf{x}$  is shown,

$$\mathbf{X} = \mathbf{x} - \boldsymbol{\rho} . \quad (3.24)$$

For a strong, slowly varying magnetic field, we can expand the magnitude of the field about the guiding center motion

$$B(\mathbf{x}) = B(\mathbf{X} + \boldsymbol{\rho}) = B(\mathbf{X}) + \boldsymbol{\rho} \cdot \nabla B \Big|_{\mathbf{x}} + \dots . \quad (3.25)$$

If we assume that in the strong, slowly varying magnetic field limit, the zeroth order frequency is the gyro-frequency, we can expand the varying frequency  $\tilde{\Omega}$  by plugging in the Taylor expanded field into the expression for  $\Omega$  (see Eq. (3.7)),

$$\tilde{\Omega} = \frac{qB(\mathbf{x})}{m} = \frac{q}{m} \left( B(\mathbf{X}) + \boldsymbol{\rho} \cdot \nabla B \Big|_{\mathbf{x}} + \mathcal{O}(\rho^2) \right) .$$



Therefore, we see that to the lowest order, the varying frequency  $\tilde{\Omega}$  is the frequency evaluated at the center of the gyro-motion, namely

$$\tilde{\Omega} \rightarrow \Omega = \frac{qB(\mathbf{X})}{m} . \quad (3.26)$$

Thus we see that  $\tilde{\Omega}$  is the gyro-frequency evaluated at the guiding center. A couple of comments on  $\tilde{\Omega}$  are appropriate: (i) the first order term has gyro-angle dependence that comes from  $\boldsymbol{\rho}$  (see Eq. (3.5)), and (ii) making a magnitude comparison of the expansion for  $\tilde{\Omega}$  gives

$$\tilde{\Omega} \sim \frac{q}{m} \left( B + \frac{\rho}{\ell_B} B + \left( \frac{\rho}{\ell_B} \right)^2 B + \mathcal{O}(\delta^3) \right) = \Omega + \delta\Omega + \delta^2\Omega + \mathcal{O}(\delta^3) ,$$

where  $\delta = \rho/\ell_B$  and the approximation  $\nabla \sim 1/\ell_B$  was used. Thus as long as  $\delta \ll 1$ , the lowest-order approximation for the characteristic frequency may be used. Note that we really don't care to expand the gyro-angle, since it is a coordinate quantity rather than a physical one. The gyro-frequency  $\Omega$ , on the other hand, is a physical quantity, thus it makes sense to expand it in a Taylor series.

### 3.4.2 Gyro-average

In the guiding center model the fast gyro-motion is averaged out, leaving the slower guiding center motion. The gyro-motion, which is approximated as circular motion, has a periodicity of  $2\pi$ ; therefore, we can average a quantity  $A(\gamma)$  that depends on the fast motion by

$$\langle A \rangle = \frac{1}{2\pi} \int_0^{2\pi} A(\gamma) d\gamma . \quad (3.27)$$

For a system with constant frequency  $\omega$ , we can write the gyro-average as an integral over time instead of the angle,  $d\gamma = d(\omega t) = \omega dt$ , thus

$$\langle A \rangle = \frac{\omega}{2\pi} \int_0^{2\pi/\omega} A(t) dt . \quad (3.28)$$

Consider the gyro-average of the particle velocity  $\langle \mathbf{v} \rangle$ . The parallel motion has no gyro-dependence, which leads to the perpendicular component being averaged out, leaving only the motion along the magnetic field line. Using Eq. (3.6), the gyro-average of the perpendicular component of the particle velocity comes out to be

$$\langle \mathbf{v}_\perp \rangle = \frac{v_\perp \Omega}{2\pi} \int_0^{2\pi/\Omega} (\cos(\Omega t) - \sin(\Omega t)) dt = 0 ,$$

where we have assumed  $\Omega$  is constant to lowest-order. This indicates that  $v_\perp$  is constant due to the conservation of kinetic energy since to the lowest-order, we have circular motion about the magnetic field line. Therefore, the gyro-averaged particle velocity gives only the parallel streaming term

$$\langle \mathbf{v} \rangle = \langle \mathbf{v}_\parallel \rangle + \langle \mathbf{v}_\perp \rangle = \mathbf{v}_\parallel . \quad (3.29)$$

### 3.4.3 Guiding Center Motion

If the magnetic field is slowly varying in space according to Eq. (3.22), we can again Taylor expand the magnetic field about the guiding center

$$\mathbf{B}(\mathbf{x}) = \mathbf{B}(\mathbf{X} + \boldsymbol{\rho}) = \mathbf{B}(\mathbf{X}) + \boldsymbol{\rho} \cdot \nabla \mathbf{B}|_{\mathbf{X}} + \dots , \quad (3.30)$$

where we see that to the lowest order the magnetic field is evaluated at the guiding center. Note that if we assume  $\mathbf{B}(\mathbf{X}) \gg \boldsymbol{\rho} \cdot \nabla \mathbf{B}|_{\mathbf{X}}$  we have circular motion; therefore, the guiding center velocity to zeroth order in  $\boldsymbol{\rho}$ , *i.e.* all fields evaluated at  $\mathbf{X}$ , can be written in terms of parallel and perpendicular components with respect to the local magnetic field

$$\mathbf{v} = v_\parallel \mathbf{b} + \rho \Omega (\cos(\Omega t) \mathbf{e}_1 - \sin(\Omega t) \mathbf{e}_2) . \quad (3.31)$$

Previously, we placed the origin of the position vector to be at the center of the circular motion and we used Cartesian unit vectors  $\hat{\mathbf{x}}$ ,  $\hat{\mathbf{y}}$ , and  $\mathbf{b}$ , where  $\mathbf{b}$  was chosen to be in the z-direction, *i.e.*  $\mathbf{b} = \hat{\mathbf{z}}$  (see Eq. (3.5)). Now we have placed the origin of the position vector at an arbitrary point and have introduced local unit vectors that are dependent on the

position and the slow time scale of the magnetic field,  $\mathbf{e}_1(\mathbf{x}, t)$  and  $\mathbf{e}_2(\mathbf{x}, t)$ , centered at the guiding center. These local coordinates obey the orthogonality relation

$$\mathbf{b} \cdot \mathbf{e}_1 \times \mathbf{e}_2 = 1 . \quad (3.32)$$

Here the guiding center velocity is derived in the usual coordinates  $(\mathbf{x}, t)$ .

In these coordinates, the gyro-angle is not an independent variable, which means we have to assume  $\Omega$  is constant in order to gyro-average, since  $t$  is an independent variable. Another approach is to use the guiding center coordinates  $(\mathbf{R}, \gamma, t)$ , where  $\gamma$  is an independent variable, hence gyro-averaging is easier. If we use the guiding center coordinate, however, a perturbation theory is used instead of the more physical argument of Taylor expansion of the magnetic field.

For slowly varying magnetic fields, we can write the position vector of a particle in terms of the fast gyrating motion  $\boldsymbol{\rho}$  and the slow guiding center motion  $\mathbf{X}$ . Taking the total time derivative and gyro-averaging will give the guiding center velocity; therefore, using Eq. (3.24) we get

$$\frac{d\mathbf{X}}{dt} = \frac{d\mathbf{x}}{dt} + \frac{d}{dt} \left( \frac{\mathbf{v} \times \mathbf{b}}{\Omega} \right) , \quad (3.33)$$

where  $\boldsymbol{\rho}$  was rewritten using Eq. (3.8). Note that  $d\mathbf{x}/dt = \mathbf{v}$  is the particle velocity which is given by Eq. (3.31). We now take the gyro-average and simplify (see Appendix C for the complete derivation of the guiding center velocity) to get the guiding center velocity

$$\langle \dot{\mathbf{X}} \rangle = v_{\parallel} \mathbf{b} + \frac{\mathbf{E} \times \mathbf{B}}{B^2} + \frac{1}{\Omega} \mathbf{b} \times \left( v_{\parallel} \frac{\partial \mathbf{b}}{\partial t} + v_{\parallel}^2 \boldsymbol{\kappa} + \frac{v_{\perp}^2}{2} \frac{\nabla B}{B} \right) + \frac{\mu_0 \mu}{qB} \mathbf{J}_{\parallel} , \quad (3.34)$$

where  $\boldsymbol{\kappa} = -\mathbf{b} \times (\nabla \times \mathbf{b}) = \mathbf{b} \cdot \nabla \mathbf{b}$  is the magnetic curvature vector. For magnetic fields that vary slowly in time, the partial time derivative of  $\mathbf{b}$  is small, *i.e.*

$$\frac{1}{\Omega} \frac{\partial \mathbf{b}}{\partial t} \sim \frac{1}{\Omega \tau_B} \ll 1 \quad (3.35)$$

and can be neglected in many cases. In magnetic confinement tokamak devices, a typical fuel

for fusion reaction is a Deuterium-Tritium mixture (Putvinski, 1998). A D-T fusion reaction yields an  $\alpha$ -particle. For the ITER experiment, it is predicted that at peak performance, the magnetic field strength will be  $\sim 11.8$  Tesla. This means the gyro-frequency of the  $\alpha$ -particles is roughly  $\Omega \approx 5.64 \times 10^8$  Hertz. Thus for  $\alpha$ -particles the condition Eq. (3.35) holds for slowly varying magnetic fields (see Eq. (3.23)), in which case we can neglect the  $\partial \mathbf{b} / \partial t$  term.

In the low  $\beta$ -limit, where  $\beta$  is the plasma pressure over magnetic energy

$$\beta = \frac{P}{B^2/2\mu_0}, \quad (3.36)$$

the parallel current density,  $\mathbf{J}_{\parallel}$ , term can be neglected since it is essentially proportional to  $\sim \beta \mathbf{J}_{\parallel}$ . Therefore, in many cases, the guiding center velocity, which we will call  $\mathbf{v}_{gc}$  from now on, can be simplified to

$$\mathbf{v}_{gc} = v_{\parallel} \mathbf{b} + \frac{\mathbf{E} \times \mathbf{B}}{B^2} + \frac{1}{\Omega} \mathbf{b} \times \left( v_{\parallel}^2 \boldsymbol{\kappa} + \frac{v_{\perp}^2}{2} \frac{\nabla B}{B} \right). \quad (3.37)$$

We encountered the first two terms in the above  $\mathbf{v}_{gc}$  expression for the more simple case of streaming along the magnetic field line and the drift motion perpendicular to the magnetic fields due to the electric field. The last two terms come from the curvature,  $\mathbf{v}_c$ , and the gradient of the magnetic field strength,  $\mathbf{v}_{\nabla B}$ . These also cause a drift perpendicular to the magnetic field. Notice that  $\mathbf{v}_c$  and  $\mathbf{v}_{\nabla B}$  depend on particle charge via  $\Omega$ . This causes a charge separation that results in an electric field and a rapid  $E \times B$  drift. This  $E \times B$  drift, if left unchecked, will rapidly propel the entire plasma radially outward to hit the wall of the tokamak. Again, equilibrium plasma confinement in a tokamak cannot exist with only a purely toroidal magnetic field. If a poloidal magnetic field is introduced, a twist in the magnetic field to neutralize the charge separation, *i.e.* the opposite charges can now travel poloidally along the magnetic field to neutralize the charge build-up (Freidberg, 2014).

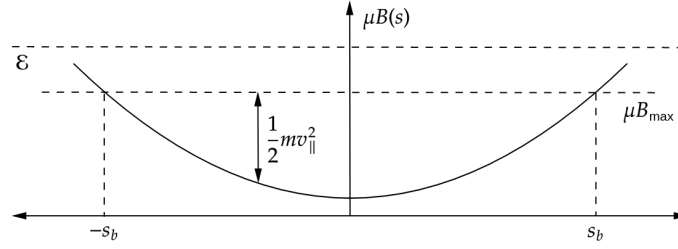


**Figure 3.3:** Potential energy for a particle in a magnetic mirror field. This mirror field is realized in tokamaks as particles travel radially inwards (in major radius  $R$ ) to stronger magnetic field (see Eq. (2.64)), causing particles with not enough parallel kinetic energy to be trapped inside the magnetic potential.

### 3.5 Motion in Axisymmetric Tokamak

In larger aspect ratio tokamaks, particles move under the joint influence of toroidal magnetic field and the much smaller poloidal magnetic field induced by the toroidal plasma current. We saw that the toroidal magnetic field was proportional to  $1/R$  (see Eq. (2.65)). When looking at the poloidal cross section, the magnetic field is greater on the inside of a flux surface, hence we have a magnetic mirror setup. This leads to populations of trapped and passing particles. Unlike the magnetic mirror setup, though, for tokamaks, the passing particles are still confined. A magnetic mirror with no electric field acceleration means kinetic energy is conserved

$$\mathcal{E} = \frac{1}{2}mv^2 = \frac{1}{2}mv_{\parallel}^2 + \mu B . \quad (3.38)$$

At bounce points,  $v_{\parallel} = 0$  (see Fig 3.3) and all the energy is in the effective potential term, *i.e.*  $\mathcal{E} \rightarrow \mu B_{\max}$ . Energy conservation then dictates that

$$\frac{1}{2}mv_{\parallel}^2 + \mu B = \mu B_{\max} . \quad (3.39)$$

It is useful to consider the pitch angle  $\alpha$  that measures the pitch away from the magnetic field. In doing so, we can come up with an approximate value for the parallel velocity to determine if the particle is trapped or passing. The pitch angle has the relation

$$\sin^2 \alpha = \frac{v_{\perp}^2}{v^2} = \frac{B}{B_{\max}} . \quad (3.40)$$

Here we can relate the magnetic fields at the bounce point and some other point where the parallel velocity is non-zero. We will specifically consider the point where the parallel velocity is the greatest, which means the effective potential is minimum, *i.e.*  $\mu B \rightarrow \mu B_{\min}$ . First, we evaluate the toroidal magnetic field at  $\theta = \pi$  on some flux surface with radius  $r = r_0$ , where the magnetic field strength is maximum; thus, via Eq. (2.65)

$$B_{\max} = \frac{B_0 R_0}{R_0 - r_0} . \quad (3.41)$$

Now at  $\theta = 0$  where the magnetic field strength is minimum on the same flux surface

$$B_{\min} = \frac{B_0 R_0}{R_0 + r_0} . \quad (3.42)$$

Using the pitch angle relation (see Eq. (3.40)) we can introduce the parallel velocity via trigonometric identity  $\cos^2 \theta + \sin^2 \theta = 1$  and the expressions for  $B_{\min}$  and  $B_{\max}$  to get

$$\frac{v_{\parallel, \max}^2}{v^2} = \cos^2 \alpha = 1 - \frac{R_0 - r_0}{R_0 + r_0} . \quad (3.43)$$

Hence, simplifying and introducing the large aspect ratio limit ( $r_0 \ll R_0$ ), we get an approximate condition for a trapped particle

$$v_{\parallel, \max} \approx v\sqrt{2\epsilon} . \quad (3.44)$$

Therefore, if a particle's maximum parallel velocity, *i.e.* parallel velocity at  $\theta = 0$ , is equal to or less than the quantity  $v\sqrt{2\epsilon}$ , the particle will be trapped.

### 3.5.1 Trapped/Passing Condition

In the above explanation, we derived the condition for a trapped particle. Essentially, we used the conservation of particle energy in a magnetic field without acceleration by an

electric field. Since the particle energy is conserved, we have  $\Delta\mathcal{E} = 0$  that allows us to say that the energy difference between two points along the orbit is zero. Choosing the point  $\theta = 0$  that corresponds to  $B_{\min}$ , and  $\theta = \pi$  that corresponds to  $B_{\max}$  on a flux surface, we have the energy conservation statement

$$\frac{1}{2}mv_{\parallel,\max}^2 + \mu B_{\min} = \mu B_{\max} , \quad (3.45)$$

with the parallel velocity a maximum at  $B_{\min}$ . We divide Eq. (3.45) by  $\mathcal{E}$  to get the expression we essentially had above (see Eq. (3.43)),

$$\frac{v_{\parallel,\max}^2}{v^2} = 1 - \frac{B_{\min}}{B_{\max}} \sim 2\epsilon . \quad (3.46)$$

Therefore, as explained above, we have the conditions

$$\frac{v_{\parallel,\max}^2}{v^2} = 2\epsilon \quad (\text{barely trapped}) , \quad \frac{v_{\parallel,\max}^2}{v^2} < 2\epsilon \quad (\text{trapped}) . \quad (3.47)$$

Let us analyze this another way. As before, we have  $B_{\max}$  at  $\theta = \pi$  and  $B_{\min}$  at  $\theta = 0$  on a flux surface. For a passing particle, the particle energy is greater than the maximum effective potential,  $V_{\text{eff},\max} = \mu B_{\max}$ , thus we have

$$\frac{\mathcal{E}}{\mu B_{\max}} > 1 ,$$

which means the particle escapes the potential and is no longer trapped. Now consider a case where the particle energy is barely smaller or even equal to  $V_{\text{eff},\max}$ . In this case the particle is said to be barely trapped, i.e. barely not enough energy to escape the potential.

This gives the condition

$$\frac{\mathcal{E}}{\mu B_{\max}} \leq 1 .$$

Now consider the case where the parallel velocity is maximum,  $v_{\parallel,\max}$ , which means from the energy conservation, the effective potential is minimum,  $V_{\text{eff},\min} = \mu B_{\min}$ . Since  $\mathcal{E}$  is

the combination of  $v_{\parallel, \max}$  and  $V_{\text{eff}, \min}$ ,  $\mathcal{E}$  can never be less than  $\mu B_{\min}$ ; therefore, we have the condition

$$\frac{\mathcal{E}}{\mu B_{\min}} > 1 .$$

By introducing the pitch angle variable,  $\lambda = \mu B_0 / \mathcal{E}$ , and using Eq. (2.66) for the large aspect ratio,  $1 \gg \epsilon = r / R_0$ , we can write the trapped/passing condition (Helander and Sigmar, 2005) as

$$\begin{aligned} \text{passing if: } & 1 - \epsilon > \lambda > 0 \\ \text{trapped if: } & 1 - \epsilon < \lambda < 1 + \epsilon . \end{aligned} \tag{3.48}$$

### 3.5.2 Banana Orbit

Banana orbits are due to the combined effects of guiding center motion parallel to the magnetic field together with the curvature and gradient drift caused by the toroidal magnetic field. Recall the guiding center velocity given in Eq. (3.37) is

$$\mathbf{v}_{\text{gc}} = v_{\parallel} \mathbf{b} + \frac{1}{\Omega} \mathbf{b} \times \left( v_{\parallel}^2 \boldsymbol{\kappa} + \frac{v_{\perp}^2}{2} \frac{\nabla B}{B} \right) ,$$

where the  $E \times B$  drift has been omitted. Assuming the lowest-order toroidal field is dominant, *i.e.*  $\mathbf{B} \approx B_t \hat{\boldsymbol{\varphi}}$ , the gradient and curvature drifts are

$$\mathbf{v}_{\nabla B} = \frac{v_{\perp}^2}{2\Omega} \frac{\mathbf{b} \times \nabla B}{B} = \frac{v_{\perp}^2}{2R\Omega} \hat{\mathbf{Z}} \tag{3.49}$$

and

$$\mathbf{v}_c = \frac{v_{\parallel}^2}{\Omega} \mathbf{b} \times \boldsymbol{\kappa} = \frac{v_{\parallel}^2}{R\Omega} \hat{\mathbf{Z}} , \tag{3.50}$$

where  $\Omega = qB_t/m$  since we assumed  $B_t \gg B_p$ . Note that the curvature of the magnetic field in this simple geometry is purely radially inward,  $\boldsymbol{\kappa} = -\hat{\mathbf{R}}$ . Therefore, the banana orbit in the axisymmetric field is governed by the velocity (Gurnett and Bhattacharjee, 2017)

$$\mathbf{v}_{\text{gc}} = v_{\parallel} \mathbf{b} + \frac{1}{R\Omega} \left( v_{\parallel}^2 + \frac{v_{\perp}^2}{2} \right) \hat{\mathbf{Z}} . \tag{3.51}$$



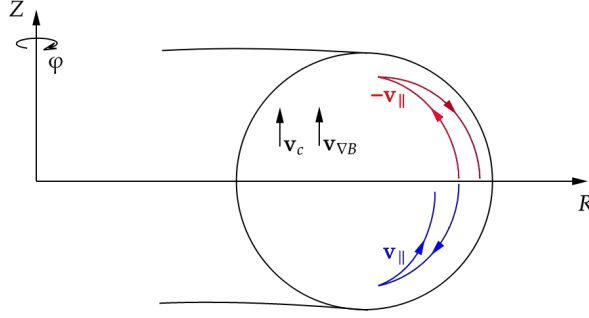


**Figure 3.4:** Depending on the initial parallel velocity, a particle in an axisymmetric field (an ion is depicted here) will bounce inward or outward due to the magnetic curvature and gradient drifts.

Thus, we see that as the particle moves along the toroidal magnetic field line, it drifts in the  $Z$ -direction. We can analyze this in the poloidal plane by considering an ion with  $\mathbf{v}_{\parallel}$  in the positive  $\varphi$ -direction. Initially, the parallel velocity points opposite to the drift velocity (see Fig. 3.4). Therefore, it will not stay on the flux surface but rather drift up. A trapped particle encounters a stronger magnetic field and bounces. The particle travels up, it again encounters a stronger magnetic field as it travels along a different flux surface and bounces again, and thus the cycle continues. Therefore, what determines whether the particle is reflected inwards or outwards is the initial parallel velocity and the gradient and the curvature drifts.

### Banana Orbit Width

The banana orbit width, measured across  $\theta = 0$  to  $\theta = \pi$ , can be found by using the conservation of canonical toroidal angular momentum. Recall that the canonical toroidal angular momentum is given by

$$\mathcal{P}_{\varphi} = mR^2\dot{\varphi} + qRA_{\varphi} . \quad (3.52)$$

We introduce the poloidal flux variable  $\psi_p$ , which is related to the toroidal component of the vector potential. The poloidal magnetic flux, *i.e.* flux through a ribbon wrapped around

toroidally, is

$$\Phi_p = \int \mathbf{B} \cdot \hat{\boldsymbol{\theta}} dS = \oint \mathbf{A} \cdot d\boldsymbol{\ell} . \quad (3.53)$$

Integration leads to the definition of  $\psi_p$ ,

$$\Phi_p = 2\pi R A_\varphi \equiv -2\pi\psi_p . \quad (3.54)$$

We also use  $v_\varphi \equiv R\dot{\varphi}$  to rewrite the toroidal canonical angular momentum in terms of  $v_\varphi$  and  $\psi_p$ ,

$$\mathcal{P}_\varphi = mRv_\varphi - q\psi_p . \quad (3.55)$$

We are interested in the average width of the banana orbit, thus the guiding center motion of these trapped particles suffices. Taking the gyro-average of Eq. (3.55), the toroidal canonical angular momentum ([Helander and Sigmar, 2005](#)) gives

$$\langle \mathcal{P}_\varphi \rangle = mRv_{\parallel} b_\varphi - q\psi_p , \quad (3.56)$$

where  $b_\varphi = \mathbf{b} \cdot \hat{\boldsymbol{\varphi}} = B_\varphi/B$ . Since  $\mathcal{P}_\varphi$  is a conserved quantity in toroidally symmetric magnetic geometry, we know  $\Delta\mathcal{P}_\varphi = 0$ . Thus, we can say  $\Delta\langle \mathcal{P}_\varphi \rangle = 0$  to obtain a relation between the change in parallel velocity and the change in poloidal flux variable

$$\Delta\psi_p = \frac{mg}{qB} \Delta v_{\parallel} . \quad (3.57)$$

Here we have neglected the variation of the toroidal flux quantity  $g = RB_\varphi$  along the particle trajectory.

Now we want to express  $\Delta\psi_p$  in terms of the mid-plane banana width  $\Delta r_b$ . In order to do so, we go back to the poloidal magnetic flux introduced in Eq. (3.53). First, we Taylor expand  $B_\theta$ , since it is assumed to be small compared to the toroidal magnetic field  $B_\varphi$ , about the center of the banana orbit  $r = r_0$

$$B_\theta(r) = B_\theta(r_0) + (r - r_0) \left. \frac{\partial B_\theta}{\partial r} \right|_{r_0} + \dots ,$$

where  $r_0$  is the radius of the flux surface the particle started out at. Recall, we assume that the poloidal magnetic field was small and roughly constant; therefore, taking only the lowest order term is a good rough estimate when calculating the banana orbit width. We now integrate the lowest order  $B_\theta = B_\theta(r_0)$  expansion to find the poloidal magnetic flux between  $\theta = 0$  and  $\theta = \pi$ , thus

$$\Delta\Phi_p \approx 2\pi B_\theta \int_{R_\pi}^{R'} R dR = \pi B_\theta (R'^2 - R_\pi^2) .$$

Here we have used  $R = R_0 + r \cos \theta$  to define  $R' = R_0 + r \cos(0) = R_0 + r'$  and  $R_\pi = R_0 + r \cos(\pi) = R_0 - r_\pi$ ; with the result  $\Delta r_b = r' - r_\pi$ . Therefore,  $\Delta\Phi_p$  comes out to be

$$\Delta\Phi_p = 2\pi B_\theta R_0 \left( \Delta r_b + \frac{\Delta r_b^2}{2R_0} \right) \approx 2\pi \Delta r_b B_\theta R_0 , \quad (3.58)$$

where we assumed  $\Delta r_b^2 \ll R_0$  in the large aspect ratio limit. Also, note that  $\Delta\Phi_p = -2\pi \Delta\psi_p$ , from Eq. (3.54). Combining these results and using Eq. (3.44) for the approximate value of  $v_\parallel$ , we end up with the final approximation for the banana orbit width

$$\Delta r_b = \frac{\sqrt{2} q_s v}{\Omega \sqrt{\epsilon}} , \quad (3.59)$$

where the safety factor  $q_s$  appearing in Eq. (2.62), and the inverse aspect ratio,  $\epsilon = r/R_0$ , is introduced.

### Banana Orbit Period

Trapped particles bounce between two bounce points caused by the gradient in the magnetic field strength along the magnetic field line of a tokamak. For the bounce period  $\tau_b$ , we want the velocity in the poloidal direction  $\mathbf{v} \cdot \nabla\theta$ , where  $\nabla\theta$  is the contravariant form of the  $\theta$  unit vector. But, since we are mostly concerned with the drift motion along the magnetic field, we get the parallel velocity in the poloidal direction upon gyro-averaging

$$\langle \mathbf{v} \cdot \nabla\theta \rangle = v_\parallel \mathbf{b} \cdot \nabla\theta = \frac{v_\parallel b_\theta}{r} . \quad (3.60)$$

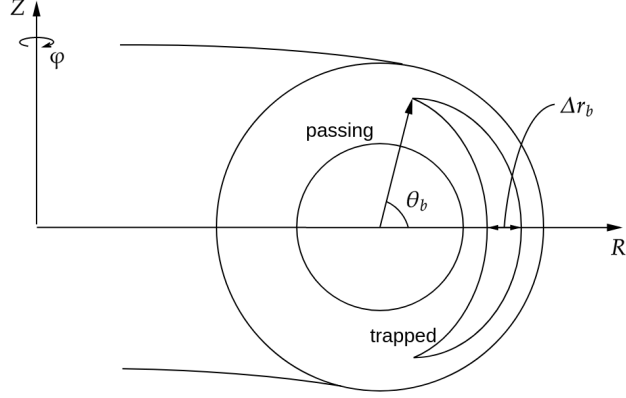


**Figure 3.5:** Trapped (banana) and passing orbits on the poloidal plane.

Ignoring the particle deviation from a flux surface (White, 2013), the bounce period of a trapped particle, in general, is given by

$$\tau_b = \int dt = \oint \frac{d\theta}{\dot{\theta}} = \oint \frac{d\theta}{v_{\parallel} \mathbf{b} \cdot \nabla \theta} . \quad (3.61)$$

For the parallel velocity, we use an expression that can be obtained from Eq. (3.38)

$$v_{\parallel} = \sqrt{\frac{2}{m} (\mathcal{E} - \mu B)} . \quad (3.62)$$

Throughout our derivation for trapped/passing particles, we have used the assumption that  $B_t \gg B_p$ , hence  $B \sim B_t$ . Also, we have assumed a large aspect ratio and expressed the magnetic field according to Eq. (2.66). With these assumptions, the parallel velocity can be written as

$$v_{\parallel} = \sqrt{\frac{2\mathcal{E}}{m}} \sqrt{1 - \lambda(1 - \epsilon \cos \theta)} ,$$

where  $\lambda = \mu B_0 / \mathcal{E}$ . Using the identity  $\cos \theta = 1 - 2 \sin^2(\theta/2)$  and rearranging gives the form which will be used for the integration

$$v_{\parallel} = v \sqrt{2\epsilon\lambda} \sqrt{\kappa^2 - \sin^2(\theta/2)} . \quad (3.63)$$

Note that  $v = \sqrt{2\mathcal{E}/m}$  and we have introduced a parameter  $\kappa$  that has the form

$$\kappa^2 = \frac{1 - \lambda(1 - \epsilon)}{2\epsilon\lambda} . \quad (3.64)$$

For passing particle,  $\kappa > 1$ , and for trapped particle,  $0 < \kappa < 1$ . Therefore,  $\kappa$  is a parameter that distinguishes if a particle is trapped or not since it is related to  $\lambda$ . We now substitute the parallel velocity into the integral for the bounce period (see Eq. (3.61))

$$\tau_b = \oint \frac{rd\theta}{b_\theta v_\parallel} = \frac{1}{v\sqrt{2\epsilon\lambda}} \frac{rB_0}{B_\theta} \oint \frac{d\theta}{\sigma\sqrt{\kappa^2 - \sin^2(\theta/2)}} . \quad (3.65)$$

Since we are neglecting the deviation from the flux surface both  $r$  and  $b_\theta$  come out of the integral (we are assuming that  $b_\theta$  is constant along the  $\theta$ -direction). Notice that the parameter  $\sigma = \pm 1$  was introduced into the integral. For trapped particle, when it bounces, the velocity changes signs; therefore,  $\sigma$  accounts for the change of sign of the parallel velocity (Helander and Sigmar, 2005). We now introduce the safety factor (see Eq. (2.62)) to get the expression (for a careful consideration of the integral Eq. (3.66), see Appendix D)

$$\tau_b = \frac{q_s R}{v\sqrt{2\epsilon\lambda}} \oint \frac{d\theta}{\sigma\sqrt{\kappa^2 - \sin^2(\theta/2)}} . \quad (3.66)$$

Once the integral above is evaluated for the case of trapped ( $0 < \kappa < 1$ ) and passing ( $\kappa > 1$ ) particles, we get the following two time periods. The first is for the full orbit of the passing particles

$$\tau_b = \frac{4q_s R}{v\sqrt{2\epsilon\lambda}} \frac{K(\kappa^{-1})}{\kappa} . \quad (3.67)$$

The second is for the full orbit of the trapped particles

$$\tau_b = \frac{8q_s R}{v\sqrt{2\epsilon}} K(\kappa) . \quad (3.68)$$

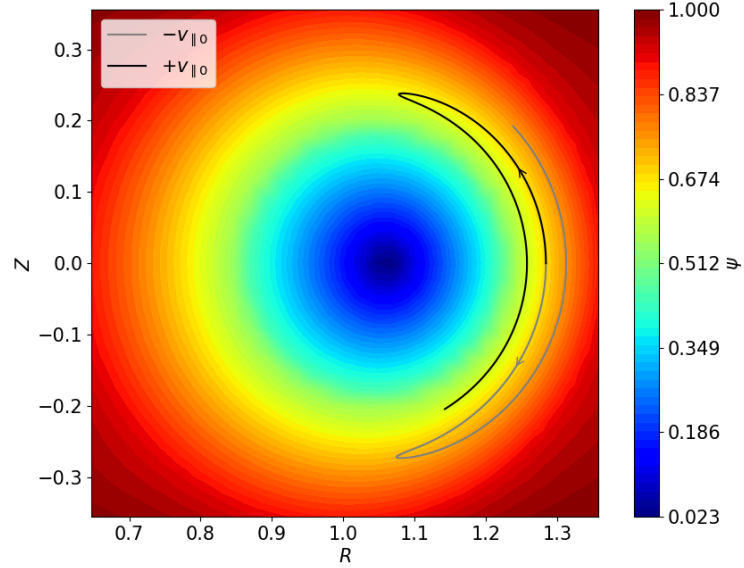


**Figure 3.6:** NIMROD uses a left-hand cylindrical coordinate system. The magnetic flux  $\psi$  is plotted as the contours and the particles are pushed in the equilibrium fields only. The  $\mathbf{v}_c$  and  $\mathbf{v}_{\nabla B}$  drifts point in the negative  $Z$ -direction causing the ion with initial negative parallel velocity to bounce outward off its starting flux surface and the ion with the positive initial parallel velocity to bounce inward from the same starting point.

The elliptic integral,  $K(k)$ , is defined on the interval  $0 \leq x < \pi/2$ , where  $k$  is called the modulus that is defined on the interval  $0 \leq k < 1$ . The elliptic integral has the form

$$K(k) = \int_0^{\pi/2} \frac{dx}{\sqrt{1 - k^2 \sin^2 x}}. \quad (3.69)$$

### 3.6 Numerical Results for Motion in Axisymmetric Tokamak

The banana orbit width and the bounce period were derived with the following main assumptions: (i) circular cross-section, (ii) small aspect ratio, *i.e.*  $\epsilon = r/R_0 \ll 1$ , and (iii) dominant toroidal magnetic field, *i.e.*  $B \sim B_t$ . For the bounce period, an additional assumption was made: when integrating, the particle does not deviate from the flux surface during the transit of the banana orbit. These assumptions were made because particle motion in more complex magnetic geometry is difficult and most often cannot be obtained analytically. Nevertheless, Eqs. (3.59) and (3.68) give a rough estimate and some insight into

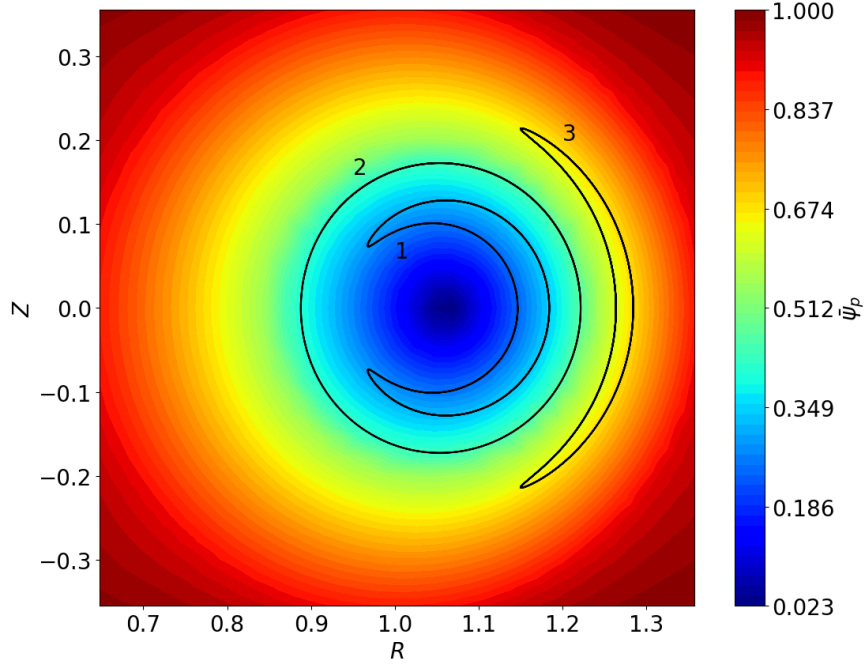


**Figure 3.7:** A contour plot of normalized poloidal magnetic flux  $\bar{\psi}_p$  is overlaid by three different particle orbits. The innermost orbit (1) is barely trapped, the middle orbit (2) is passing since it circumnavigates the entire flux surface, and the outermost orbit (3) is deeply trapped.

these behaviors. We will compare numerical results with the analytical expression for the banana orbit width and the bounce period. We consider a case with circular cross-section where the particles are pushed along the equilibrium fields. Note that in the numerical simulation, which represent the exact solution to within numerical errors, the assumptions  $\epsilon \ll 1$  and  $B \sim B_t$  are not applied; also, the banana orbit does deviate from the flux surface during the transit. Therefore, we should expect differences in the results from the analytic expression and the numerical values we present here.

In Fig. 3.4, we saw that for  $\mathbf{v}_c$  and  $\mathbf{v}_{\nabla B}$  drifts pointing in the positive  $Z$ -direction with a right-hand cylindrical coordinate system, the initial positive parallel velocity bounces inward and initial negative parallel velocity bounces outward. In NIMROD, a left-hand cylindrical coordinate system is used and the  $\mathbf{v}_c$  and  $\mathbf{v}_{\nabla B}$  drifts, due to the equilibrium magnetic field

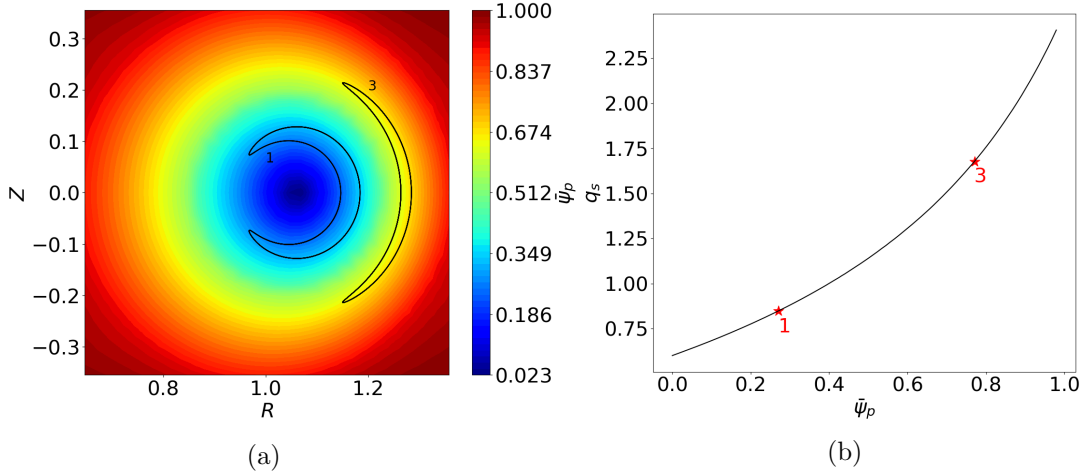


**Figure 3.8:** Figure (a) shows the orbit of barely trapped (1) and deeply trapped (3) particles overlaid on a contour plot of  $\bar{\psi}_p$ . Figure (b) shows the corresponding safety factor  $q_s$  where the value of  $q_s$  is shown for orbits 1 and 3 at their initial flux surfaces.

orientation, point in the negative  $Z$ -direction. This results in similar behavior. Thus, as we can see from Fig. 3.6, that we end up with the same underlying physics as predicted by the numerical results.

Particles with different initial positions and initial parallel velocities were considered numerically. In Fig. 3.7, three of those cases are shown. The innermost orbit is the barely trapped particle, where the parallel velocity is large enough so that it travels farther along the magnetic field line until it encounters a strong enough effective magnetic potential,  $V_{\text{eff}} = \mu B$ , and then bounces. The middle orbit is the passing particle, where the parallel kinetic energy is always greater than magnetic potential, hence it never bounces. The outermost orbit is the deeply trapped particle where the parallel kinetic energy is much smaller than the magnetic potential (see Fig. 3.3).

The banana width and the bounce period for barely trapped (1) and deeply trapped (3) particles are considered (see Fig. 3.7) and the results from Eqs. (3.59) and (3.68) with the assumptions that were used in deriving the two expressions, are compared to the numerical values. A Deuterium ion with mass  $m = 3.344 \times 10^{-27}$  kg and charge  $q = 1.602 \times 10^{-19}$  C was pushed along the equilibrium fields. The deeply trapped particle is considered first.



The particle has an initial position of  $(R_{\text{init}}, Z_{\text{init}}) = (1.284, 0)$  with initial velocity  $v_{\perp 0} = 3.0 \times 10^5$  m/s and  $v_{\parallel 0} = 1.0 \times 10^5$  m/s. From Fig. 3.8, we see that at  $(R_{\text{init}}, Z_{\text{init}})$ , the normalized poloidal magnetic flux has the value  $\bar{\psi}_p = 0.7708$ , which gives the safety factor of  $q_s = 1.677$ . Since we are assuming  $B \sim B_t$ , the magnetic field strength at the magnetic axis is roughly  $B_0 = 0.9676$  T and at the initial position  $(R_{\text{init}}, Z_{\text{init}})$ , we have  $B_t = 0.7843$  T. The major radius for the equilibrium set up is  $R_0 = 1.06$  m; thus the inverse aspect ratio for the flux surface given at  $(R_{\text{init}}, Z_{\text{init}})$  is  $\epsilon = 0.2116$ , for which the small aspect ratio limit does not hold. When using the values provided above the following analytical values are obtained:  $\Delta r_b = 0.0211$  m and  $\tau_b = 1.171 \times 10^{-4}$  s, for the banana width and the bounce period, respectively. From the numerical simulation, the banana width is  $\Delta r_b = 0.0205$  m and the bounce period is  $\tau_b = 0.772 \times 10^{-4}$  s. Next we consider the barely trapped (3) particle. The initial position of the barely trapped particle is  $(R_{\text{init}}, Z_{\text{init}}) = (1.147, 0)$ , hence the inverse aspect ratio comes out to be  $\epsilon = .08161$ . The initial velocities of the particle are  $v_{\perp 0} = 3.0 \times 10^5$  m/s and  $v_{\parallel 0} = 1.281 \times 10^5$  m/s. Again, from Fig. 3.8 we see that the normalized poloidal flux is  $\bar{\psi}_p = 0.2708$  with the safety factor of  $q_s = 0.8488$ . The magnetic field strength at the axis is the same as before, while at the initial position, we have  $B_t = 0.8935$  T. Using these values, the analytical results for the barely trapped particle comes out to be  $\Delta r_b = 0.0311$  m for the banana width, where the numerical result is  $\Delta r_b = 0.0376$  m. For the bounce period we need a little more explanation of the results. First, when

$$\lambda = \frac{\mu B_0}{\mathcal{E}} = \frac{v_{\perp}^2 B_0}{v^2 B} \quad (3.70)$$

was calculated (recall Eq. (3.48)), the result came out to be  $\lambda = 0.916$ , which gave the following value for  $\kappa = 1.03$  (see Eq. (3.64)). Notice that  $\kappa > 1$ , which is the condition for passing particles. Thus, we already see a discrepancy in the analytical results. Nonetheless, in order to calculate the bounce time we let  $\lambda = 1$  since as  $\lambda \rightarrow 1 - \epsilon = 0.9135$ , which is close to the  $\lambda$  calculated from Eq. (3.70), the particle's bounce period approaches infinity since it becomes a passing particle as it reaches the boundary  $\lambda = 1 - \epsilon$  (see Eq. (3.48)). Letting  $\lambda = 1$ , we end up with the analytical bounce period of  $\tau_b = 9.84 \times 10^{-5}$  s which agrees with

the numerical result fairly well,  $\tau_b = 8.64 \times 10^{-5}$  s. As expected, these results do not agree perfectly. This is due to the underlying assumptions, *i.e.*  $\epsilon \ll 1$ ,  $B \sim B_t$ , and no deviation from flux surface during orbit transit. Keep in mind that in the numerical simulations, the particles are pushed along their trajectories to within small numerical errors. Nevertheless, it is interesting to note that for the barely trapped case, which had the smaller  $\epsilon$  value, the analytical bounce time was closer to the numerical result.

## CHAPTER 4

## SERENDIPITY SHAPE FUNCTIONS IN NIMROD'S PARTICLE SIMULATION

The particle-in-cell (PIC) approach uses the equations of motion to push computational particles. Thus the fields, *e.g.* electric, magnetic (or current density), must be known at the particle position  $(R, Z, \varphi)$ . In NIMROD, the fields and the coordinates  $(R, Z)$  are discretized on a two-dimensional (2D) finite element grid in the poloidal plane. This means that we need to check if the particle is actually in the finite element cell in question or not. Thus, a searching algorithm is needed to check if a particle's logical coordinates  $(\xi, \eta)$  are within the finite element cell, where each cell is defined on the interval  $[-1, 1]$  in both logical directions.

NIMROD has parallel algorithm capabilities. This means that a particle could leave a discretized block in the poloidal plane (handled by a single compute node) and enter another. In the original PIC implementation for NIMROD, this was handled by exchanging particles between processors owning different blocks (Kim et al., 2004). This approach also led to poor load balancing since processors owning blocks in the higher pressure core had significantly more particles than those owning blocks in the low-pressure edge region of the plasma. In order to avoid needing to exchange particles and permit almost perfect load balancing, the field information was incorporated into global structures so that all processors could push particles throughout the global domain. These structures eliminate the need for the processors to hand-off particles whenever they leave one block in the computational domain and enter another. These improvements on the previous code, where the field information was stored in local structures, eliminated the time-intensive communication between processors during the push and equalized the number of particles pushed by each processor.

In Fig. 4.1, the logical and the physical grids for the DIII-D giant sawtooth case is shown. The total computational domain is divided up between different processors, where 16 processors (blocks in the poloidal plane) were used for the case shown in the figure.

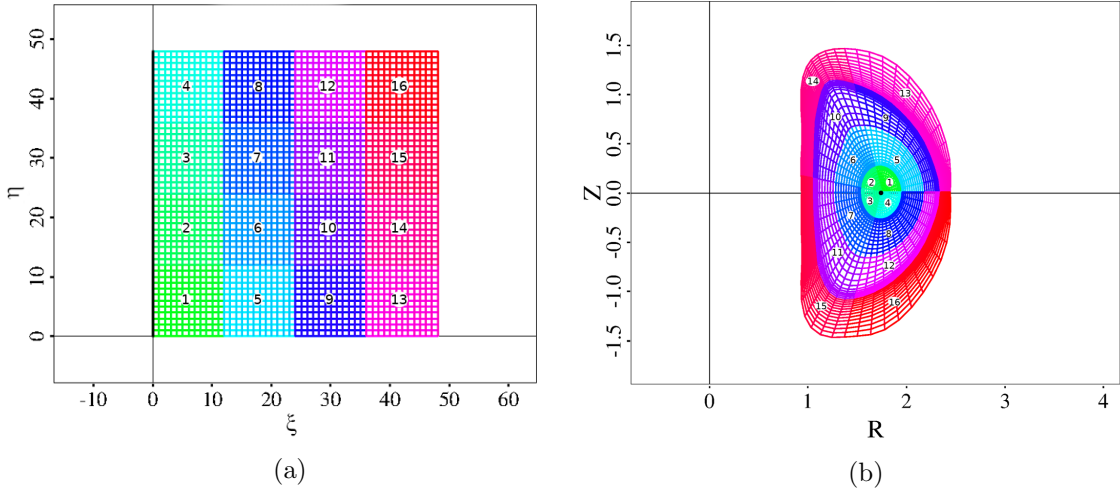


**Figure 4.1:** Figure (a) shows the logical grid that the fields are defined on in terms of either the 2D Lagrange or Serendipity basis sets. Figure (b) shows the physical grid for DIII-D geometry. Here computational domain is divided up amongst 16 different processors. The magnetic axis indicated by a black dot on the physical grid corresponds to the  $\eta$ -axis ( $\xi = 0$ ) on the logical grid.

Each processor's computational domain is discretized on a 2D finite element grid and each finite element uses a basis of 2D Lagrange polynomials. When pushing the computational particles, the full set of coefficients in the 2D Lagrange basis expansion could be used to deposit particle information to the finite element nodes and evaluate the fields in the push. Unfortunately, using the full set to deposit particle information onto NIMROD's grid requires evolving particle shape functions. This is time consuming. Instead, we choose to assume  $\delta$ -function, point particles, which make deposition easy and instead retain higher-order accuracy in the field evaluation used for the particle push. Nevertheless, the 2D Lagrange coefficients are directly used for the Serendipity basis sets. This is done since the nodal location of the Serendipity set coincide with the Lagrange set (see Fig. 4.2). Therefore, when gathering and scattering the computational particles using the Serendipity basis, only the coefficients that coincide with the 2D Lagrange basis are used. This was done to reduce memory in the global field storage yet allow for potentially higher order accuracy compared to the existing bilinear implementation.

We now go into more details of the gathering and scattering process that is essential

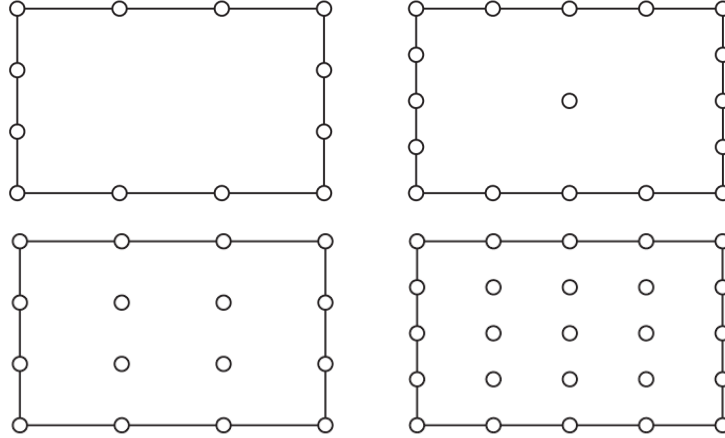


**Figure 4.2:** The top two cells are the node location for the Serendipity sets (left: bicubic and right: biquartic) while the bottom two cells are the node locations for the Lagrange sets (left: bicubic and right: biquartic). The nodal locations for both are the same except the Serendipity has fewer nodes in the center of the finite element cell.

to the PIC method in a finite element code like NIMROD. We will also formally state how the fields in NIMROD are represented and how the physical coordinates can be expanded via the basis sets, 2D Lagrange or Serendipity. A Newton-Raphson iteration is used for the nonlinear mapping between the logical and physical coordinates. A different form (more convenient for NIMROD, than Eqs. (2.55) and (2.56)) for the equations of motion is used for pushing the computational particles (see Eqs. (4.1) and (4.2)). The Serendipity shape functions were tested with tracer particles pushed along the equilibrium fields. The terms that appear in the equilibrium equations of motion are presented. For the computational particles to alter the fields, particle information needs to be deposited onto the finite element grid. We discuss this further in Chapter 5. Here we present the results of using the reduced set of Serendipity shape functions for tracer particles compared to the full 2D Lagrange polynomials.

#### 4.1 Gathering and Scattering of Particles on the Finite Element Grid

In NIMROD, 2D finite elements are used in the poloidal plane and a Fourier series decomposition is used in the periodic, toroidal direction (Sovinec et al., 2004). Higher order Lagrange polynomials are used to represent the field quantities on the finite element grid

with scalar and vector quantities discretized as

$$a(R, Z, \varphi) = \sum_{k,n} (a_{kn} e^{in\varphi} + a_{kn}^* e^{-in\varphi}) L_k^p(\xi, \eta) \quad (4.1)$$

and

$$\mathbf{A}(R, Z, \varphi) = \sum_{k,\ell,n} (A_{k\ell n} e^{in\varphi} + A_{k\ell n}^* e^{-in\varphi}) L_k^p(\xi, \eta) \mathbf{e}_\ell . \quad (4.2)$$

The finite element basis functions  $L_k^p$  of polynomial degree  $p$  are defined on the logical (computational) coordinates  $(\xi, \eta)$ . The quantities  $a_{kn}$  and  $A_{k\ell n}$ , with their complex conjugates  $a_{kn}^*$  and  $A_{k\ell n}^*$ , are the complex coefficients for the expansions in 3D. Each index in Eqs. (4.1) and (4.2) represents the following: (i)  $k$  indicates the finite element basis function, which for NIMROD's nodal finite element representation corresponds to a point (node) in the poloidal plane, (ii)  $\ell$  gives the vector components, *e.g.*  $\ell = R, Z, \varphi$  for cylindrical coordinates, and (iii)  $n$  is the Fourier mode.

For PIC to operate inside a finite element code like NIMROD, a mapping from the physical  $(R, Z)$  to logical  $(\xi, \eta)$  coordinates needs to take place. This central process of PIC simulation, known as gathering and scattering (Kim et al., 2004), is essential in pushing the particles along the fields. The computational particles in PIC may be pushed via the guiding center equations of motion

$$\dot{\mathbf{X}}_{\text{gc}} = v_{\parallel} \mathbf{b} + \frac{\mathbf{E} \times \mathbf{B}}{B^2} + \frac{m}{qB^4} \left( v_{\parallel}^2 + \frac{v_{\perp}^2}{2} \right) \left( \mathbf{B} \times \nabla \left( \frac{B^2}{2} \right) \right) + \frac{\mu_0 m v_{\parallel}^2}{qB^2} \mathbf{J}_{\perp} \quad (4.3)$$

and

$$m\dot{v}_{\parallel} = -\mathbf{b} \cdot (\mu \nabla B - q\mathbf{E}) , \quad (4.4)$$

where the rapid gyro-motion has been averaged out and the force on a magnetic moment in a non-uniform magnetic field is present in Eq. (4.4). In Eq. (4.3), the magnetic curvature  $\boldsymbol{\kappa}$  was expressed in terms of the current density via the pre-Maxwell form of Ampere's law (see Eqs. (2.56) and (3.34)). The guiding center velocity, Eq. (4.3) will be discussed again in Chapter 5. Since the field quantities in the equations of motion are updated at each time

step, the mapping from  $(R, Z)$  to  $(\xi, \eta)$  (*i.e.* gathering) and pushing via the equations of motion (*i.e.* scattering) of computational particles on the finite element grid happens at each time step.

The mapping between the physical and logical coordinates (or vice-versa) is nonlinear, thus an iterative method is employed. The physical  $(R, Z)$  coordinates are expanded in terms of continuous basis functions as follows:

$$R = \sum_{k=1} R_k N_k^p(\xi, \eta) \quad , \quad Z = \sum_{k=1} Z_k N_k^p(\xi, \eta) \quad , \quad (4.5)$$

where the coefficients  $(R_k, Z_k)$  correspond to the coordinates  $(R, Z)$  at the finite element node  $k$  and  $N_k^p$  are the basis functions of polynomial degree  $p$  in  $\xi$  and  $\eta$  for the node  $k$ . Here  $N_k^p(\xi, \eta)$  represents a larger set of basis functions that include the  $L_k^p$ 's in Eqs. 4.1 and 4.2 as one possibility. For the PIC algorithm in NIMROD, either the Lagrange  $L_k^p$ , Serendipity  $S_k^p$ , or the reduced Serendipity  $s_k^p$  polynomials are implemented for the mapping and the field evaluation.

For the nonlinear mapping between logical  $(\xi, \eta)$  and physical  $(R, Z)$  coordinates, the Newton-Raphson method is utilized. Consider a vector function  $\mathbf{f}(\mathbf{x}_0 + \Delta\mathbf{x})$  where  $\Delta\mathbf{x} = \mathbf{x} - \mathbf{x}_0$  is a small displacement from  $\mathbf{x}_0$ . Using a Taylor expansion, the vector function (in our case the coordinates  $R$  and  $Z$ ) is expanded to first order as

$$f_i(\mathbf{x}_0 + \Delta\mathbf{x}) \approx f_i(\mathbf{x}_0) + \sum_{j=1}^n \frac{\partial f_i}{\partial x_j} \Delta x_j \quad , \quad i = 1, 2, \dots, n \quad , \quad (4.6)$$

where  $n$  is the dimensionality of the problem. We can express the above Taylor expansion in vector form

$$\begin{bmatrix} f_1(\mathbf{x}_0 + \Delta\mathbf{x}_1) \\ \vdots \\ f_n(\mathbf{x}_0 + \Delta\mathbf{x}_n) \end{bmatrix} = \begin{bmatrix} f_1(\mathbf{x}_0) \\ \vdots \\ f_n(\mathbf{x}_0) \end{bmatrix} + \begin{bmatrix} \frac{\partial f_1}{\partial x_1} & \cdots & \frac{\partial f_1}{\partial x_n} \\ \vdots & \ddots & \vdots \\ \frac{\partial f_n}{\partial x_1} & \cdots & \frac{\partial f_n}{\partial x_n} \end{bmatrix} \begin{bmatrix} \Delta\mathbf{x}_1 \\ \vdots \\ \Delta\mathbf{x}_n \end{bmatrix} . \quad (4.7)$$

The matrix that appears on the right side is the Jacobian matrix  $\mathcal{J}$ , which consists of the

partial derivatives of the vector function  $\mathbf{f}$  in terms of the variables  $x_j$ . In a more compact form

$$\mathbf{f}(\mathbf{x}_0 + \Delta\mathbf{x}) = \mathbf{f}(\mathbf{x}_0) + \mathcal{J}\Delta\mathbf{x} . \quad (4.8)$$

The task is to find the roots of the above expression. In order to do so, we demand that  $\mathbf{f}(\mathbf{x}_0 + \Delta\mathbf{x}) = 0$ . Recall that  $\Delta\mathbf{x} = \mathbf{x} - \mathbf{x}_0$ , thus solving Eq. (4.8) for  $\mathbf{x}$  gives

$$\mathbf{x} = \mathbf{x}_0 - \mathcal{J}^{-1}\mathbf{f}(\mathbf{x}_0) , \quad (4.9)$$

where  $\mathcal{J}^{-1}$  is the inverse of the Jacobian matrix. The above expression allows for the following iteration

$$\mathbf{x}_{(i+1)} = \mathbf{x}_{(i)} - \mathcal{J}_{(i)}^{-1}\mathbf{f}(\mathbf{x}_{(i)}) , \quad (4.10)$$

where  $i$  on the inverse Jacobian indicates that it is evaluated at that iteration. Using Eq. (4.10), we can update the values  $\mathbf{x}_{(i+1)}$  if we know  $\mathbf{x}_{(i)}$ , assuming that  $\mathcal{J}_{(i)}^{-1}$  can be computed. The initial starting point of the iteration, *i.e.*  $\mathbf{x}_{(0)}$ , is chosen to be at the center of the finite element cell. The iteration for the Newton-Raphson method is continued until some tolerance is met, at which point the logical coordinates  $(\xi, \eta)$  agree (to within the desired tolerance) with the physical coordinates  $(R, Z)$  that the particle has been pushed to.

In NIMROD's PIC routine the physical coordinates are expanded in terms of the logical ones (see Eq. (4.5)). Note that we have  $\mathbf{f} \doteq (R, Z)$  and  $\mathbf{x} \doteq (\xi, \eta)$ , therefore via Eq. (4.6) we get

$$\begin{aligned} R(\xi_0 + \Delta\xi, \eta_0 + \Delta\eta) &\approx R(\xi_0, \eta_0) + \frac{\partial R}{\partial \xi}\Delta\xi + \frac{\partial R}{\partial \eta}\Delta\eta , \\ Z(\xi_0 + \Delta\xi, \eta_0 + \Delta\eta) &\approx Z(\xi_0, \eta_0) + \frac{\partial Z}{\partial \xi}\Delta\xi + \frac{\partial Z}{\partial \eta}\Delta\eta , \end{aligned} \quad (4.11)$$

where  $(\xi_0, \eta_0)$  are the logical value at the center of the finite element cell in the poloidal plane. We solve these equations for the new logical variables  $(\xi_{(i+1)}, \eta_{(i+1)})$  in terms of the old ones  $(\xi_{(i)}, \eta_{(i)})$ . This gives us the following iterative method of finding the logical



coordinates for the known physical coordinates

$$\begin{bmatrix} \xi_{(i+1)} \\ \eta_{(i+1)} \end{bmatrix} = \begin{bmatrix} \xi_{(i)} \\ \eta_{(i)} \end{bmatrix} + \frac{1}{\det(\mathcal{J}_{(i)})} \begin{bmatrix} \frac{\partial Z}{\partial \eta} & -\frac{\partial R}{\partial \eta} \\ -\frac{\partial Z}{\partial \xi} & \frac{\partial R}{\partial \xi} \end{bmatrix}_{(\xi_{(i)}, \eta_{(i)})} \begin{bmatrix} R - R_{(i)} \\ Z - Z_{(i)} \end{bmatrix}. \quad (4.12)$$

Here the determinant of the Jacobian matrix,  $\det(\mathcal{J}_{(i)})$ , and the derivatives in the matrix are evaluated at  $(\xi_{(i)}, \eta_{(i)})$ . In order to evaluate the Jacobian matrix, we need to take the derivatives of the polynomials  $N_k^p(\xi, \eta)$  in Eq. (4.5). The determinant of the Jacobian for Eq. (4.12) is simply

$$\det(\mathcal{J}) = \frac{\partial R}{\partial \xi} \frac{\partial Z}{\partial \eta} - \frac{\partial R}{\partial \eta} \frac{\partial Z}{\partial \xi}. \quad (4.13)$$

#### 4.1.1 Bilinear Shape Functions

Consider the simplest example of the lowest polynomial order, *i.e.* bilinear case. This means products of 1D linear functions in  $\xi$  and  $\eta$ . Similar steps can be taken for higher order polynomials. The only difference is that more terms will be introduced making the analytical (and computational) algebra more tedious. Note that the bilinear polynomials for the Lagrange and Serendipity bases are the same. The bilinear polynomial can be expressed as

$$N_k^1(\xi, \eta) = a_1 + a_2\xi + a_3\eta + a_4\xi\eta, \quad (4.14)$$

where  $-1 \leq \xi, \eta \leq 1$ . In two dimensions, in order to indicate the location of the node, we introduce two other variables  $\{\xi', \eta'\}$  for each node  $k$  to clarify what the index  $k$  means. As an example, consider the node at the lower left corner of a finite element, where this node is indicated by  $k = 1$  with  $\xi' = -1$  and  $\eta' = -1$ , *i.e.*  $k = 1 \implies \{-1, -1\}$ , (see Fig. 4.3); hence we have

$$N_1^1(\xi, \eta) \equiv N_{\{-1, -1\}}^1 = a_1 - a_2\xi - a_3\eta + a_4\xi\eta = a(1 - \xi)(1 - \eta). \quad (4.15)$$

Note that  $\{\xi', \eta'\}$  is essentially given by the value of  $(\xi, \eta)$  of the location of node  $k$ . The simplifying assumption that all  $a$ 's are the same was made to obtain the last form in

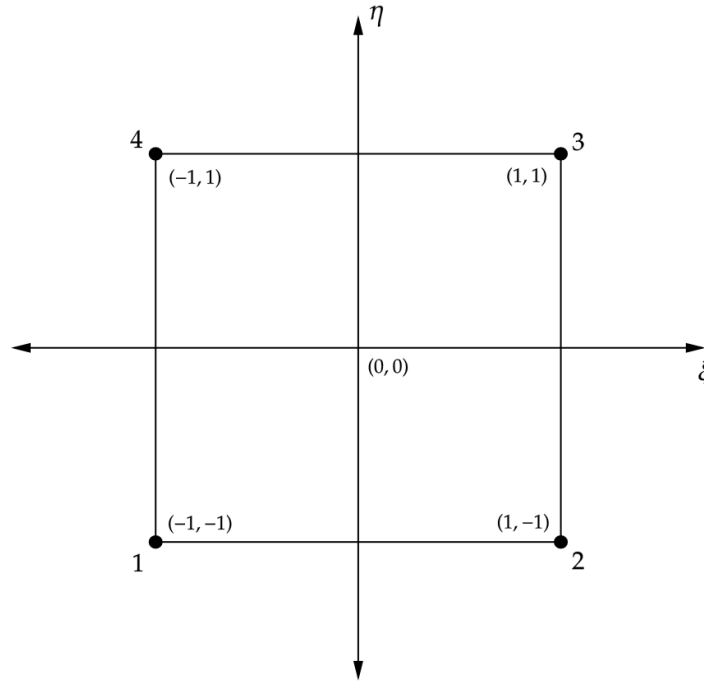


**Figure 4.3:** A square finite element cell with a bilinear decomposition consists of 4 vertex node locations at the corners of the cell. The finite element cell is defined on the interval  $[-1, 1]$  for both  $\xi$  and  $\eta$ . The center of the cell is placed at the location  $(0, 0)$ . The locations of the nodes are indicated by dots.

the above expression. This is true for simple square elements. The coefficient  $a$  is the normalizing factor so that at the node location  $\{-1, -1\}$  we have  $N_1^1 = 1$ .

Using the form given in Eq. (4.15), the polynomials for the bilinear case, which consists of four nodes (see Fig. 4.3), are

$$\begin{aligned} N_1^1 &= \frac{1}{4} (1 - \xi) (1 - \eta) , & N_2^1 &= \frac{1}{4} (1 + \xi) (1 - \eta) , \\ N_3^1 &= \frac{1}{4} (1 + \xi) (1 + \eta) , & N_4^1 &= \frac{1}{4} (1 - \xi) (1 + \eta) . \end{aligned} \quad (4.16)$$

Using the above bilinear basis functions we can now express the partial derivatives of the  $(R, Z)$ -expansion (see Eq. (4.5)). Letting  $G_k \doteq \{R_k, Z_k\}$  represent the coefficients at node  $k$

for both  $R$  and  $Z$ , allows us to write the partial derivatives in terms of the coefficients

$$\begin{aligned}\frac{\partial G}{\partial \xi} &= \frac{1}{4} \left[ (G_2 - G_1 + G_3 - G_4) + \eta (G_1 - G_2 + G_3 - G_4) \right] \\ \frac{\partial G}{\partial \eta} &= \frac{1}{4} \left[ (G_4 - G_1 + G_3 - G_2) + \xi (G_1 - G_4 + G_3 - G_2) \right].\end{aligned}\tag{4.17}$$

If we let  $\xi = 0$  and  $\eta = 0$ , *i.e.* the center of the finite element cell, the two later terms in Eq. (4.17) vanish. Thus we can, in general, separate the determinant of  $\mathcal{J}$  into terms evaluated at the center and at the  $i^{\text{th}}$  iteration  $(\xi_{(i)}, \eta_{(i)})$  as

$$\det(\mathcal{J}) = \left( \frac{\partial R}{\partial \xi} \frac{\partial Z}{\partial \eta} - \frac{\partial R}{\partial \eta} \frac{\partial Z}{\partial \xi} \right)_{(0,0)} + \left( \frac{\partial R}{\partial \xi} \frac{\partial Z}{\partial \eta} - \frac{\partial R}{\partial \eta} \frac{\partial Z}{\partial \xi} \right)_{(\xi_{(i)}, \eta_{(i)})}\tag{4.18}$$

This indicates that to start the Newton-Raphson iteration, it would be convenient to begin the iteration from the origin of the finite element cell and then update the Jacobian via the terms that have  $\xi$  and  $\eta$  dependence throughout the iteration.

## 4.2 Serendipity Shape Functions

As was mentioned above, Serendipity shape functions are implemented in NIMROD's PIC routine for the mapping from physical to logical coordinates (or vice-versa) and for the field evaluation. Therefore, we will now give a few general comments regarding the Serendipity polynomials. Afterward, we will give a method for constructing the nodal Serendipity polynomials from the closely related Lagrange polynomials by considering the fourth-order (biquartic) case.

In NIMROD's nodal finite element approach, basis functions have  $C^0$  continuity between cells. By forming a tensor product of two Lagrange polynomials in two orthogonal directions (logical  $(\xi, \eta)$ ), one can build a Lagrange set in two dimensions. We define this 2D region  $\mathcal{Q}^2$  as a bi-unit square

$$\mathcal{Q}_p^2 = \{-1 \leq \xi, \eta \leq 1\},\tag{4.19}$$

where  $p$  indicates the polynomial degree that represents the 2D bi-unit square region. The

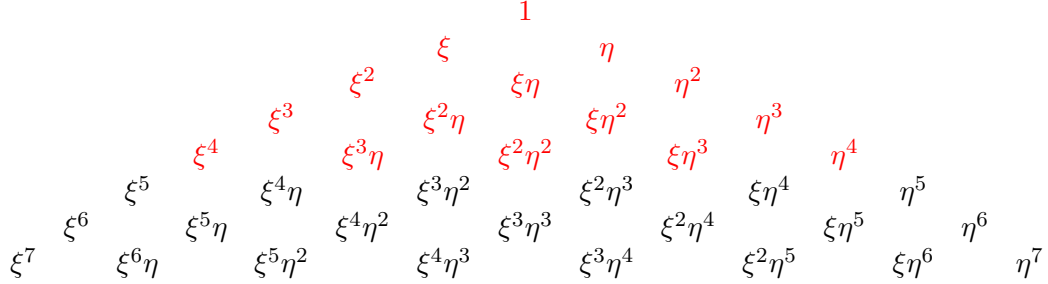


**Figure 4.4:** Terms that are included in  $\mathcal{P}_4^2$  are shown in red.

Serendipity set that doesn't include the full tensor product of the interior nodes as does the Lagrange polynomials (Arnold and Awanou, 2011), is also defined on the similar bi-unit square that we will call

$$\mathcal{S}_p^2 = \{-1 \leq \xi, \eta \leq 1\} . \quad (4.20)$$

The nodal Serendipity set can be built from the Lagrange polynomials; therefore, it can be considered as a subset of the Lagrange polynomials with fewer degrees of freedom. Note that as long as all the cell boundary nodes are kept in the Lagrange polynomial set, and the Serendipity sets are built from them,  $C^0$  continuity will be valid for the Serendipity sets as well. As for the interior nodes, there is some freedom in choosing the nodal locations (Karniadakis et al., 2005). For the Serendipity biquartic case the interior node was placed at the center of the finite element cell.

Figures 4.4 and 4.5 are examples of Pascal's triangle that is useful when talking about the terms considered in the Serendipity set. In order to build complete Serendipity sets, we pick the order  $p$  that spans the bi-unit square  $\mathcal{S}_p^2$  and then add the two extra terms  $\{\xi^p\eta, \xi\eta^p\}$ , thus

$$\mathcal{S}_p^2 = \mathcal{P}_p^2 + \text{span} \{\xi^p\eta, \xi\eta^p\} , \quad (4.21)$$

where  $\mathcal{P}_p^2$ , also defined on the bi-unit square  $\mathcal{P}_p^2 = \{-1 \leq \xi, \eta \leq 1\}$ , includes all the terms in Pascal's triangle up to the order  $p$  (see Fig. 4.4). Therefore, if we were to build the

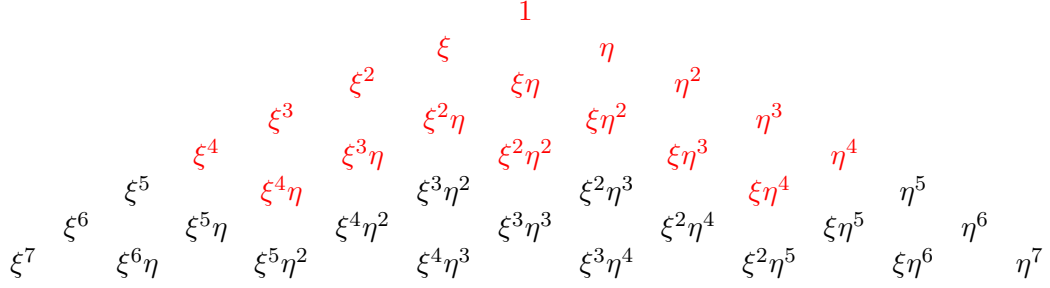


**Figure 4.5:** Terms that are included in  $\mathcal{S}_4^2$  are shown in red. Notice the extra two terms  $\{\xi^4\eta, \xi\eta^4\}$  that were added to the set.

fourth-order Serendipity set  $\mathcal{S}_4^2$ , we would have the terms

$$\mathcal{S}_4^2 = \text{span} \{1, \xi, \eta, \xi\eta, \xi^2, \eta^2, \xi^2\eta, \xi\eta^2, \xi^3, \eta^3, \xi^2\eta^2, \xi^3\eta, \xi\eta^3, \xi^4, \eta^4, \xi^4\eta, \xi\eta^4\} . \quad (4.22)$$

This is easier to see using Pascal's triangle (see Fig. 4.5). The explicit forms of the Serendipity basis sets are given in Appendix E.

The crucial point is that the Serendipity set has fewer terms than the Lagrange set. Note that the last two terms  $\{\xi^4\eta, \xi\eta^4\}$  in the expression above arise due to the edge nodes when expanding these subset polynomials for a square cell. These two terms are required for completeness of the quadrilateral expansion (Karniadakis et al., 2005). If we were to construct Serendipity sets for fifth- or sixth-order and higher, we would have to introduce more internal nodes. If we want to introduce a Lagrange-like nodal placement for order  $p > 4$ , this would yield a non-symmetric nodal placement for these polynomials (Floater and Gillette, 2017). Therefore, for order  $p > 4$ , we have constructed a set that has no interior nodes. We call this the reduced Serendipity set  $\mathcal{R}_p^2 = \{-1 \leq \xi, \eta \leq 1\}$  (also defined on the bi-unit square). The terms that give rise to the interior nodes have been removed from the Serendipity set in order to build these reduced sets. As an example, we consider the fourth order case

$$\mathcal{R}_4^2 = \text{span} \{1, \xi, \eta, \xi\eta, \xi^2, \eta^2, \xi^2\eta, \xi\eta^2, \xi^3, \eta^3, \xi^3\eta, \xi\eta^3, \xi^4, \eta^4, \xi^4\eta, \xi\eta^4\} . \quad (4.23)$$

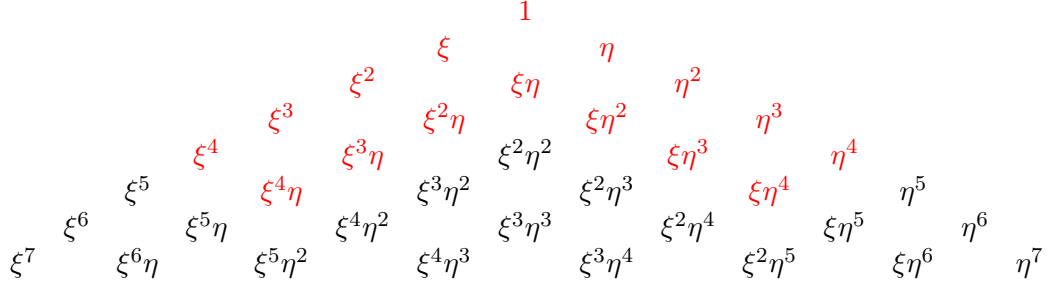


**Figure 4.6:** Terms that are included in  $\mathcal{R}_4^2$  are shown in red. Notice that the two terms  $\{\xi^4\eta, \xi\eta^4\}$  are still included in the set but the term  $\{\xi^2\eta^2\}$ , which results in an interior node, is removed.

Note that the  $\{\xi^2\eta^2\}$  term is missing from the above list. This is shown in Pascal's triangle for the reduced biquartic case in Fig. 4.6.

All of the polynomial sets discussed above are nodal, thus they satisfy the Kronecker delta condition

$$N_k^p(\xi_\ell, \eta_\ell) = \delta_{k\ell} , \quad (4.24)$$

where  $N_k^p \doteq (L_k^p, S_k^p, s_k^p)$  represents the polynomials with degree  $p$  that coincides with the appropriate bi-unit square space described above, meaning  $L_k^p(\xi, \eta) \in \mathcal{Q}_p^2$ ,  $S_k^p(\xi, \eta) \in \mathcal{S}_p^2$ , and  $s_k^p(\xi, \eta) \in \mathcal{R}_p^2$ . The above relation indicates that the nodal polynomial function is equal to unity at node  $k$  while zero everywhere else. The second condition they satisfy is the partition of unity

$$\sum_k N_k(\xi, \eta) = 1 , \quad (4.25)$$

which says that when all the shape functions are added together, they equal 1 throughout the unit cell. It is also important to note that for all of these polynomial basis sets, the location of the nodes coincide with each other. Meaning, the node location for the Serendipity and the reduced Serendipity polynomials are subset of the Lagrange polynomials. This makes the communication between NIMROD's finite element fluid formulation and the PIC formulation more convenient. This is due to the fact that we can use the nodal coefficients from the Lagrange basis for the Serendipity basis when gathering and scattering the compu-

tational particles in the PIC formulation, while potentially obtaining a higher order spatial convergence. Although other basis transformation between the different sets may prove to be more accurate, we sought the most efficient one in terms of memory footprint and run-time, especially when running PIC simulations with millions of computational particles. We will see later that despite using the simplest basis transformation, higher order convergence was obtained on average while keeping the memory footprint and the run-time sufficiently low.

#### 4.2.1 Construction of the Biquartic Serendipity Shape Functions

Nodal Serendipity shape functions can be constructed using the Lagrange polynomials (Zienkiewicz et al., 2005). Here we will build the fourth order (biquartic) shape functions as an example. The same approach can be taken to build any order of these nodal Serendipity shape functions as long as the location of the nodes are known. First, we define the one dimensional Lagrange polynomials

$$\ell_k^n(\xi) = \frac{(\xi - \xi_0)(\xi - \xi_1) \dots (\xi - \xi_{k-1})(\xi - \xi_{k+1}) \dots (\xi - \xi_n)}{(\xi_k - \xi_0)(\xi_k - \xi_1) \dots (\xi_k - \xi_{k-1})(\xi_k - \xi_{k+1}) \dots (\xi_k - \xi_n)} = \prod_{\substack{i=1 \\ i \neq k}}^n \frac{\xi - \xi_i}{\xi_k - \xi_i} . \quad (4.26)$$

Polynomials for each node  $k$  can be constructed via the above expression. This gives an amplitude of unity at the desired node and zero at the remaining nodes. In two dimensions, we can construct these Lagrange polynomials for each dimension, say  $\xi$  and  $\eta$ , and multiply them together in order to obtain a 2D Lagrange set at an arbitrary node  $k$

$$L_k^p(\xi, \eta) = \ell_i^n(\xi) \ell_j^m(\eta) , \quad (4.27)$$

where we will only consider the case of  $n = m$  which is hardwired into the NIMROD code. The superscript  $p$  indicates the order of the 2D Lagrange polynomial; therefore, if  $p = 2$  we have a biquadratic 2D Lagrange set. The same notation will be used for the Serendipity set, indicated by  $S_k^p$ . A reduced Serendipity set will also be mentioned, which will be indicated by a lower case  $s$ , thus  $s_k^p$ . These reduced Serendipity sets have no interior nodes.

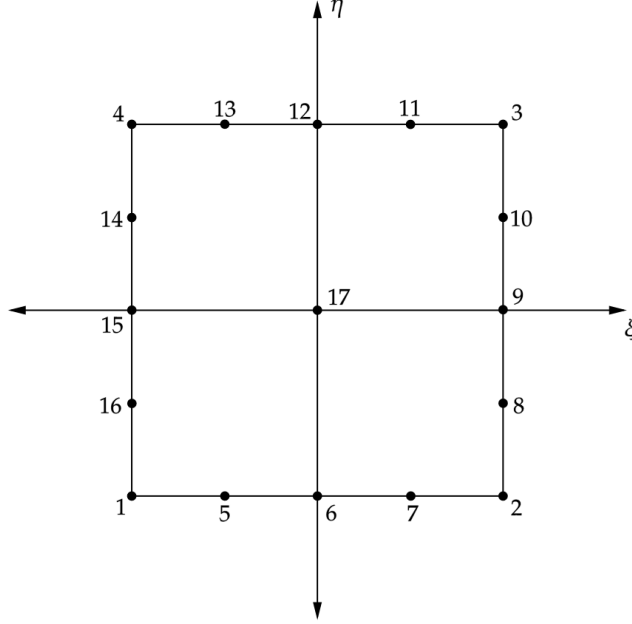


**Figure 4.7:** A square finite element cell with complete fourth-order (biquartic) Serendipity decomposition consists of 17 node locations with one in the middle of the cell. The center of the cell is placed at the location  $(0, 0)$ . The location of the nodes are indicated by dots.

The goal is to reduce the degrees of freedom and thus lower the computational time and memory but still obtain higher order spatial resolution when pushing the particles along their trajectories. The lowest order (bilinear) Lagrange and Serendipity sets are the same,  $L_k^1 = S_k^1 = s_k^1$ . In the case of  $k = 1$  node, we have

$$L_1^1(\xi, \eta) = \frac{1}{4} (1 - \xi) (1 - \eta) , \quad (4.28)$$

where  $1/4$  is the normalization factor.

We will now construct a complete Serendipity set, with one interior node in the middle of the finite element cell. For the purpose of building the Serendipity sets, we introduce further notation. For mid-side nodes ( $k = 5, 6, 7, 8, 9, 10, 11, 12, 13, 14, 15, 16$ ) (see Fig. 4.7), we will let  $k \doteq m$ . For the corner nodes ( $k = 1, 2, 3, 4$ ) we will let  $k \doteq c$ ; and finally, for the center node ( $k = 17$ ) we will let  $k \doteq o$ . The 1D Lagrange polynomials in  $\xi$  and  $\eta$ , which we indicate them by  $\ell_{\xi,k}^p \equiv \ell_k^p(\xi)$  and  $\ell_{\eta,k}^p \equiv \ell_k^p(\eta)$ , respectively (see Eq. (4.27)),



will also be used when constructing the fourth-order Serendipity shape functions.

Using the convention given above, we start by building the mid-side nodes. First, the fourth order 1D Lagrange polynomials in either  $\xi$  or  $\eta$ , *i.e.*  $\ell_{\xi,k}^4$  or  $\ell_{\eta,k}^4$ , are multiplied by a linear function of the opposite variable, meaning

$$S_m^4(\xi, \eta) = \ell_{\xi,m}^4(1 \pm \eta) \quad \text{and} \quad S_m^4(\xi, \eta) = \ell_{\eta,m}^4(1 \pm \xi) , \quad (4.29)$$

where a minus sign is chosen for the  $-1$  boundaries and a positive for the  $+1$  boundaries in  $(\xi, \eta)$ . Before moving on to the corner nodes, it is imperative that these mid-side nodes are normalized so that at the node  $k \doteq m$ , the amplitude is unity.

Once the mid-side nodes are built and normalized we can start the construction of the corner nodes. The corner nodes can be constructed by subtracting the biquartic mid-side shape functions from the bilinear corner Lagrange polynomials. This ensures that at each node, other than that specific corner node, the function value is zero, and at that node the amplitude is unity. Thus, we have

$$S_c^4(\xi, \eta) = L_c^1(\xi, \eta) - \sum_m a_m S_m^4(\xi, \eta) , \quad (4.30)$$

where  $a_m = S_m^4(\xi_m, \eta_m)$  is the value of the mid-side node Serendipity polynomial (see Eq. (4.29)) evaluated at the node location  $(\xi_m, \eta_m)$ . The linear combination of the mid-side nodes needs to be subtracted off so that  $S_c^4$  is zero at those nodes. Note that only the mid-side nodes that are adjacent to the corner node being constructed need to be considered. For example, when constructing the corner node  $k = 1$ , we have

$$S_1^4(\xi, \eta) = L_1^1 - (a_5 S_5^4 + a_6 S_6^4 + a_7 S_7^4 + a_{14} S_{14}^4 + a_{15} S_{15}^4 + a_{16} S_{16}^4) , \quad (4.31)$$

where  $a_5 = 3/4$ ,  $a_6 = 1/2$ ,  $a_7 = 1/4$ ,  $a_{14} = 1/4$ ,  $a_{15} = 1/2$ ,  $a_{16} = 3/4$ , see Fig. 4.8. If we are considering the reduced Serendipity polynomials, we don't have to consider the internal node. Performing the similar task for all corner nodes gives us the set.

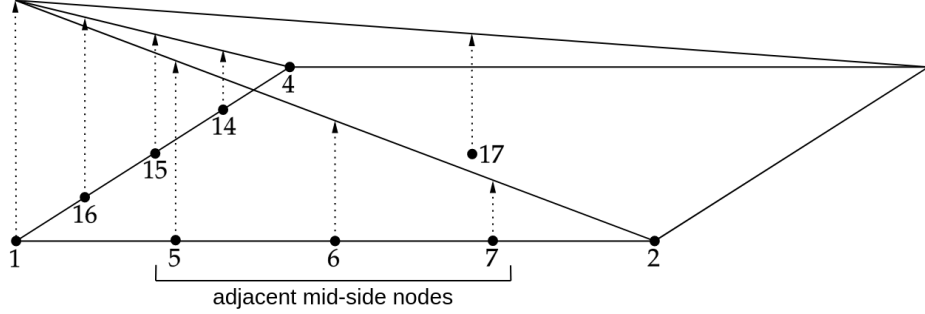


**Figure 4.8:** A linear combination of the adjacent mid-side nodes and the center node is subtracted from the bilinear Lagrange polynomial  $L_1^1(\xi, \eta)$  to make the Serendipity biquartic polynomial  $S_1^4(\xi, \eta)$ . This insures that these Serendipity polynomials satisfies the conditions stated in Eqs. (4.24) and (4.25). Note that an example for node  $k = 1$  is shown.

For the complete set of fourth order Serendipity shape functions, we need to introduce the central node, which has the form

$$S_o^4(\xi, \eta) = (1 - \xi^2)(1 - \eta^2) . \quad (4.32)$$

Since a new node has been added, we have to insure that all other biquartic shape functions are zero at the central node; therefore, we find the value of the corner and mid-side node shape functions at the central node and subtract that much of the central shape function from all others. For the corner nodes

$$S_c^4(\xi, \eta) = S_c^{\text{old},4} - b_o S_o^4 , \quad (4.33)$$

where  $S^{\text{old},4}$  indicates the old previously found shape functions, and  $b_o = S_c^{\text{old},4}(\xi_o, \eta_o)$  are the values of the corner Serendipity functions at the center  $(\xi_o, \eta_o)$ . Similarly, for the mid-side nodes

$$S_m^4(\xi, \eta) = S_m^{\text{old},4} - a_o S_o^4 , \quad (4.34)$$

with  $a_o = b_o = 1/2$ . Once the above steps are taken in order to construct the biquartic

Serendipity shape functions, we can see that they satisfy the conditions in Eqs. (4.24) and (4.25). If we want to build the incomplete fourth-order Serendipity shape functions  $s_k^4$ , we would just skip the part where we added the center node. The shape functions are given in the Appendix E.

### 4.3 Numerical Results for Serendipity Basis Functions

The Serendipity shape functions were used for tracer particles moving according to the equations of motion in the equilibrium fields. The goal here is to simply assess the accuracy of using the reduced field information of the Serendipity sets compared to the full 2D Lagrange representation. The equilibrium fields associated with Fig. 4.1 for the DIII-D giant sawtooth case were used. The Serendipity cases were tested against the full 2D Lagrange polynomials, where we treated the Lagrange cases as “exact” solutions for the particle trajectories. The equations of motion (here subscript 0 indicates equilibrium fields)

$$\dot{\mathbf{X}}_{\text{gc}0} = v_{\parallel} \mathbf{b}_0 + \frac{m}{qB_0^4} \left( v_{\parallel}^2 + \frac{v_{\perp}^2}{2} \right) \left( \mathbf{B}_0 \times \nabla \left( \frac{B_0^2}{2} \right) \right) + \frac{\mu_0 m v_{\parallel}^2}{qB_0^2} \mathbf{J}_{\perp 0} \quad (4.35)$$

and

$$m\dot{v}_{\parallel 0} = -\mu \mathbf{b}_0 \cdot \nabla B_0, \quad (4.36)$$

were integrated using the predictor-corrector method. The  $E \times B$  drift in Eq. (4.3) and the  $\mathbf{E}$ -term in Eq. (4.4) do not appear since we are assuming that the equilibrium electric field is negligible, *i.e.*  $\mathbf{E}_0 = 0$ .

The fields and coordinates of each finite element in NIMROD are represented by 2D Lagrange polynomials. Thus, when pushing the computational particles, the coefficients of the 2D Lagrange basis expansion are directly used as the coefficients for the Serendipity basis sets. This is done since the nodal location of the Serendipity set are a subset of the Lagrange set (see Fig. 4.9). This cuts down on the computational time when evaluating the fields and reduces global storage while allowing for processor to push particles throughout the spatial domain. Therefore, when gathering and scattering the computational particles

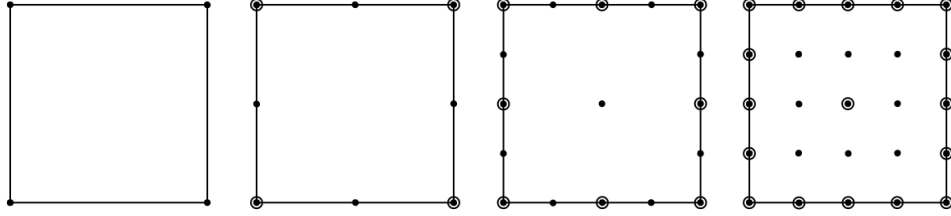


**Figure 4.9:** From left to right, the nodal representations are: bilinear, Serendipity biquadratic, Serendipity biquartic, and 2D Lagrange biquartic (“exact”). The circle around the nodes indicates the coinciding nodes from the previous representation. Thus for example, when running the Serendipity biquartic case, the 2D Lagrange coefficients at the circled nodes are directly used in the Serendipity basis representation.

using the Serendipity basis, the coefficients that are not part of the expansion are ignored and the the coefficients that coincide with the Lagrange basis are used in hopes of achieving a higher-order convergence while using fewer data points to represent the fields. Again, we were looking for the most efficient approach that saves on the memory footprint and run-time with the desire to run PIC simulations with millions of computational particles. Therefore, the above approach was taken with the goal of achieving higher-order convergence while keeping the memory foot print and the run time sufficiently low.

The difference in the poloidal position at each time step was considered for the Serendipity and the Lagrange representations. In Fig. 4.10, the errors between the bilinear, Serendipity biquadratic (biquad), and reduced Serendipity biquartic (biquar) and the “exact” 2D Lagrange representation were calculated via

$$\epsilon_D = \frac{\sqrt{(R - R^*)^2 + (Z - Z^*)^2}}{\sqrt{R^2 + Z^2}}, \quad (4.37)$$

where  $(R^*, Z^*)$  are used to represent the reduced sets and  $(R, Z)$  are used for the “exact” set at each time step. Figure. 4.10 presents the errors as a function of time. We note that the errors for the biquadratic and incomplete biquartic cases are significantly smaller than the bilinear case which is used in NIMROD’s default PIC method. Thus by utilizing the Lagrange coefficients mapped onto Serendipity basis sets, we were able to obtain better convergence, at least for this case.

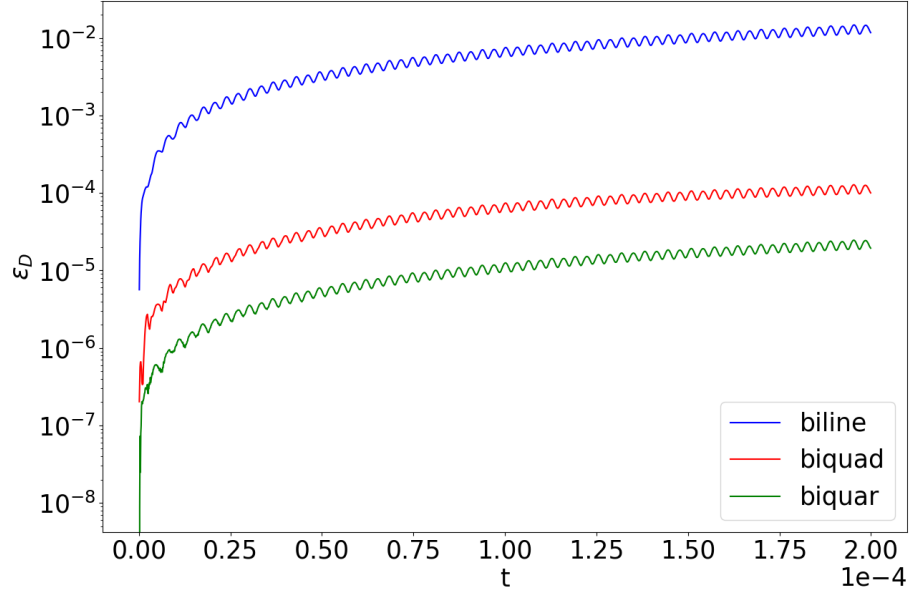


**Figure 4.10:** The error  $\epsilon_D$  between the different representations (see Eq. (4.37)) is shown. The three errors relative to the “exact” 2D Lagrange are: bilinear (biline), Serendipity biquadratic (biquad), and the reduced Serendipity biquartic (biquar). Note that the  $y$ -axis is log-scaled.

For some particle trajectories, however, the biquadratic representation did better than the biquartic (see Fig. 4.11). Many tracer particles were examined but no pattern was found. At first it was speculated that near the magnetic axis, where the Jacobian (see Eq. (4.12)) can have issues, is where this was happening. But, as other trajectories were studied, the effects appeared to be random. Since the behavior of the different basis representations seemed random, an average error of the trajectories’  $R$  coordinates

$$\langle \Delta R \rangle = \frac{1}{N} \sum_{j=1}^N \Delta R_{\max,j}^* \quad (4.38)$$

was considered. The quantity  $\Delta R_{\max,j}^*$  represents the maximum error in the  $j^{\text{th}}$  particle trajectory for the reduced representations and  $N$  is the total number of computational particles.

Roughly 30000 tracer particles were used to calculate the average error for the different

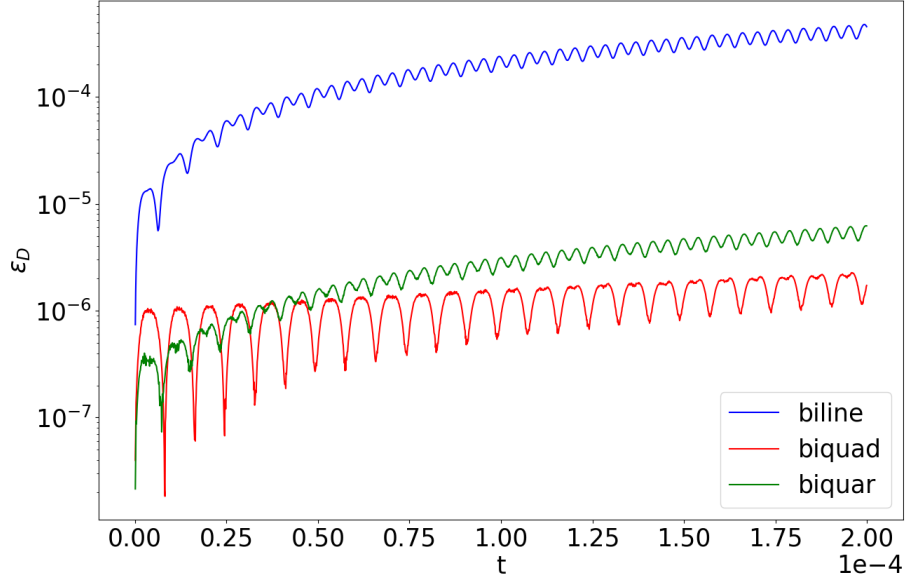


**Figure 4.11:** The error  $\epsilon_D$  for the reduced Serendipity biquartic case does worse than the biquadratic case. However, both are still more accurate than the bilinear (biline) approach.

representations. The errors in the particle trajectories were calculated against the full 2D Lagrange case as before and averaged using Eq. (4.38) to see how the trajectories were being resolved overall in the PIC algorithm. The average error in the physical  $R$  coordinate (see Fig. 4.12), and in the parallel velocity (see Fig. 4.13) are shown. These figures show the results for all Serendipity (complete or reduced) sets. It is interesting to see that the complete Serendipity biquartic (cmplt4) case, which has the one interior node in the middle, has the smallest error. This is indicative of how the interior node helps in resolving the particle trajectory. Also, note the reduced Serendipity biquartic (biquar), biquintic (biquin), and the bisextic (bisext) cases with no interior nodes have similar error on average, hence adding more boundary nodes makes little difference in predicting the particle trajectory more accurately. One odd result is that the error in the  $R$  coordinate from the Serendipity biquadratic at time step 3500 does, on average, better than the Serendipity bicubic (see Fig. 4.12). Note that this is not the case for the average error in the parallel velocity  $\langle \Delta v_{\parallel} \rangle$ . While the results given in Fig. 4.12 and Fig. 4.13 show that all the higher order

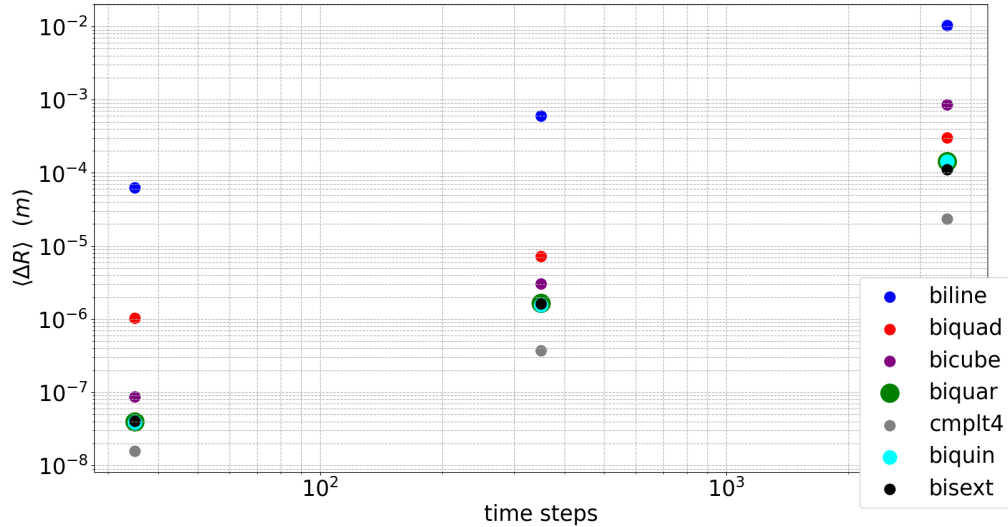


**Figure 4.12:** Average error in the physical  $R$  (m) coordinate for all Serendipity (complete/reduced) sets compared against the "exact" 2D Lagrange polynomials. The errors were averaged over  $\sim 30000$  particles. The cases were run for 35, 350, and 3500 time steps with each time step  $\Delta t = 2.0 \times 10^{-8}$  seconds. The results shown are for bilinear (biline), biquadratic (biquad), bicubic (bicube), reduced biquartic (biquar), biquartic (cmplt4), reduced biquintic (biquin), and reduced bisextic (bisext).

representations do better than the bilinear case by a significant amount, the user would still have to decide whether the extra effort was worth it for a PIC simulation in NIMROD. NIMROD production runs often use a biquartic 2D Lagrange representation. For this important case replacing the bilinear field representation with biquadratic or biquartic may be desirable if greater accuracy is needed in the particle push.

Next, we looked at the memory footprint of each of the representations. The total memory footprint given in Fig. 4.14 is the combination of memories used for the basis functions  $N_k^p$ , the global field array, and the computational particle structure that stores the particle information. Since we are using fewer coefficients for the Serendipity sets, the memory for these is significantly less. Figure 4.14 shows that as the polynomial degree increases, the memory used for the full 2D Lagrange basis significantly increases due to the increasing number of interior nodes that need to be added. While for the Serendipity cases with no interior nodes, the memory used is much smaller. For the "cmplt4" case the

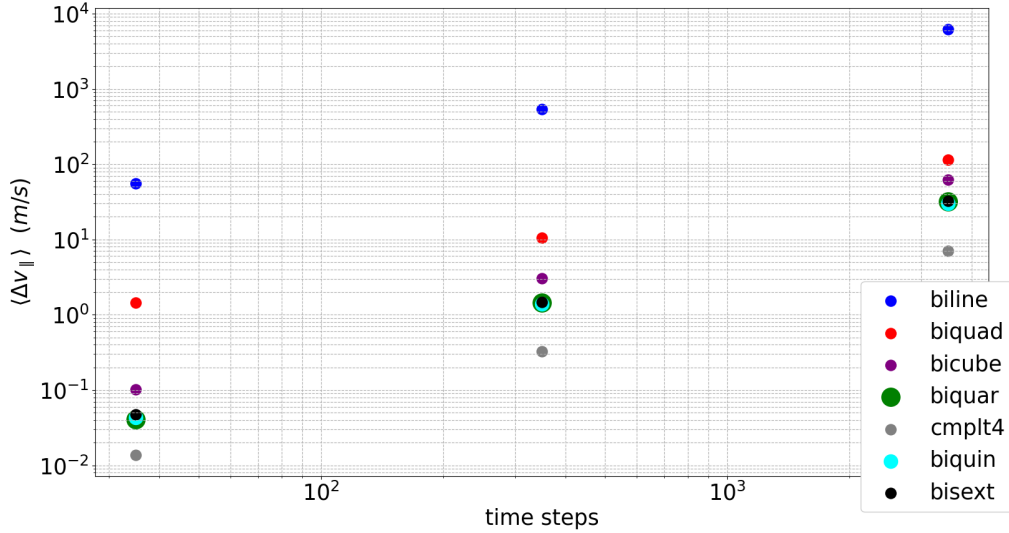


**Figure 4.13:** Average error in the parallel velocity  $v_{\parallel}$  (m/s) for all Serendipity (complete/reduced) sets compared against the “exact” 2D Lagrange polynomials. The errors were averaged over  $\sim 30000$  particles. The cases were run for 35, 350, and 3500 time steps with each time step  $\Delta t = 2.0 \times 10^{-8}$  seconds. The results shown are for bilinear (biline), biquadratic (biquad), bicubic (bicube), reduced biquartic (biquar), biquartic (cmplt4), reduced biquintic (biquin), and reduced bisextic (bisext). Note that the biquartic case with the central node (cmplt4) outperforms the fifth and sixth order representations.

interior node adds a bit more of memory (see Fig. 4.14), but this extra node gives us a particle trajectory that has much less error than the reduced “biquar” case (see Fig. 4.12 and Fig. 4.13).

Finally, we looked at the run time of each of the representations. It is important to note that two different setups were used, the *load-balanced* and the *non-load-balanced* cases. When running the code in parallel, if we do not load-balance the computational particles, the processors have different number of particles depending on whether their blocks in the poloidal plane are in the high-pressure core or at the edge of the plasma. Recall that the purpose of storing the fields for the particle push in structures that encompass the global domain was to allow processors to push an equal number throughout the computational domain. In the old algorithm, some processors worked much harder than others, which slowed down the code. If we were to load-balance the particles, then the particles would



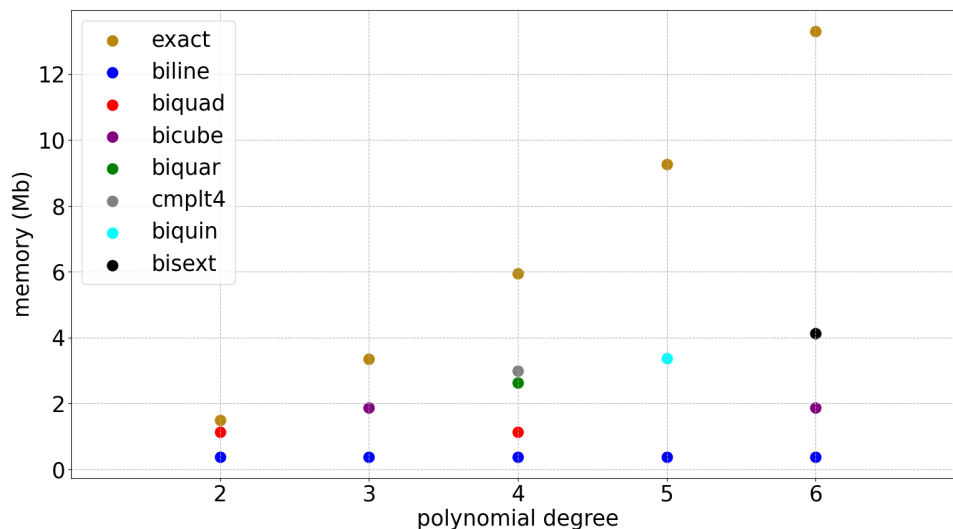


**Figure 4.14:** The total memory used for each representation is plotted as a function of polynomial degree. The Serendipity (complete or reduced) cases use much less memory than the full 2D Lagrange polynomials. Memory is given in Megabits (Mb). Roughly 30000 particles were used, thus the memory used will increase with more particles, but the overall trend between different cases will remain similar. The total memory consists of the basis functions  $N_k^p$ , the global field array, and the computational particle structure that stores the particle information.

be evenly distributed among the processors, hence each would roughly perform an equal amount of tasks. This can speed up the code by a good bit. The load-balancing will be discussed in Chapter 5 in more details when we talk about the particle weights, the sampling of physical and velocity space, and the time evolution of the weights. Figure 4.15 shows that the load-balanced cases, indicated by ▼, do better than the non-load-balanced cases, indicated by • in terms of real-time. This is especially true for the “exact” case. It is interesting to see that the run time for all Serendipity cases is fairly close while the “exact” cases seem to increase exponentially. Also, note the “cmplt4” case, where the run time is only slightly greater than the “biquar” and rest of the cases, obtains a much greater accuracy than the rest of the Serendipity representations (see Fig. 4.12 and Fig. 4.13).

As a reminder, the results in this chapter use the coefficients from the full 2D Lagrange basis for the Serendipity sets. A least-squares projection using the two bases may likely

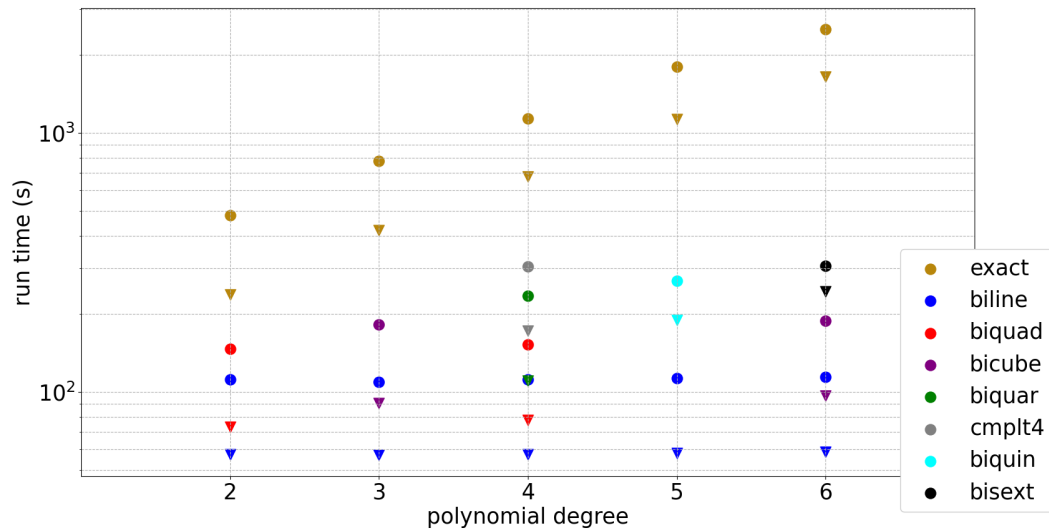


**Figure 4.15:** Comparing the total run-time (s) for different representations as a function of polynomial degree. The data points with ▼ indicates the load-balanced and ● indicates the non-load-balanced cases. Note that  $y$ -axis is given in log-scale.

lead to better results for the reduced Serendipity sets. That being said, transforming the basis at each time step could prove to be costly in run time for the gathering and scattering process of the PIC algorithm. Perhaps one way to “truly” implement the Serendipity sets would be to introduce it in the NIMROD routines. In which case the fields would already be represented in terms of the Serendipity basis sets, thereby eliminating the need for basis transform in the PIC algorithm. If the Serendipity basis sets were implemented in NIMROD, an extensive study of the performance of these polynomials and how they perform in plasma fluid equations would have to be considered. This approach is beyond the scope of this thesis, hence it was not pursued. The least-squares projection approach, though not implemented, is discussed briefly below.

#### 4.4 The Method of Least Squares

The least squares method is widely used for fitting a predicted model to a data sample. The parameters of the model are estimated so as to minimize the residual. In almost all applications, the system is over determined; therefore, an exact fit to the data sample

is impossible. The parameters that minimizes the residual is the best thing that can be done. We will apply the least square method to two locally continuous basis functions, namely Lagrange polynomials  $L_k^p(\xi, \eta)$  and the Serendipity shape functions  $S_k^p(\xi, \eta)$  where  $k$  denotes the finite element nodes and  $p$  the polynomial degree as before.

We want to minimize the square of the residual

$$\int \left( \sum_k a_k S_k^p(\xi, \eta) - f(\xi, \eta) \right)^2 d\xi d\eta = \min, \quad (4.39)$$

where we expand the function via the Serendipity basis. This means we have an optimization problem where we optimize the square of the residual with respect to the parameters. The parameters in this case are the coefficients of the Serendipity basis expansion  $a_k$ 's. We take the derivative with respect to the  $a_k$ 's and set it equal to zero to end up with the expression

$$\int S_{k'}^p(\xi, \eta) \sum_k a_k S_k^p(\xi, \eta) d\xi d\eta = \int S_{k'}^p(\xi, \eta) f(\xi, \eta) d\xi d\eta.$$

The above expression can be solved for the coefficients by introducing the mass matrix

$$M_{k'k} = \int S_{k'}^p(\xi, \eta) S_k^p(\xi, \eta) d\xi d\eta \quad (4.40)$$

and inverting it in order to get

$$a_k = \sum_{k'} M_{k'k}^{-1} \int S_{k'}^p(\xi, \eta) f(\xi, \eta) d\xi d\eta. \quad (4.41)$$

Note that  $M_{k'k}^{-1}$  is the inverse of the mass matrix. Equation (4.41) solves for the coefficients of the Serendipity basis expansion. Now if the function  $f(\xi, \eta)$  is already expanded in 2D Lagrange polynomials  $L_j^p$  (at node  $j$ ) and their corresponding coefficients  $b_j$ 's, then we get

$$a_k = \sum_{j,k'} b_j M_{k'k}^{-1} \int S_{k'}^p(\xi, \eta) L_j^p(\xi, \eta) d\xi d\eta. \quad (4.42)$$

This allows us to transform from the Lagrange basis  $L_j^p$ , given its coefficients  $b_j$ , and find the Serendipity coefficients  $a_k$ .

CHAPTER 5  
THE  $\delta f$ -PIC APPROACH IN NIMROD

Energetic particles can have significant effects on confined plasma stability, even when the density of energetic particles is much smaller than that of the bulk magnetohydrodynamics (MHD) plasma. Examples of such energetic particles are those produced by neutral beams (Stix, 1972), external radio-frequency (RF) sources (Stix, 1975), or fusion-produced  $\alpha$ -particles. Although the bulk plasma can be well modeled by fluid-MHD, the energetic particles require kinetic theory for an adequate description. This leads to the hybrid kinetic-MHD model where energetic particles are coupled into the fluid model through either the energetic pressure tensor or the current density (Tronci et al., 2014). This model allows for a multi-scale approach where the bulk plasma can be modeled with the MHD timescale and a kinetic timescale can be considered for the energetic particles. If the fast timescales of gyro-motion is relevant, then the full Vlasov description is used. Although in tokamak devices, where the plasma is strongly magnetized, we can use the drift kinetic regime where the fast gyro-motion is averaged out.

The  $\delta f$ -PIC approach in NIMROD uses the energetic pressure tensor to couple the energetic particles to the fluid equations in the drift kinetic regime. The bulk plasma is modeled via the finite element fluid code NIMROD (Sovinec et al., 2004), while a particle-in-cell (PIC) code (Kim, 2008) is used for the minority energetic particles. In order to couple the kinetic energetic particles to the fluid-MHD equations, we dump the energetic particle information onto the finite element grid via  $\mathbf{P}_{\text{hot}}$ , a process called deposition. Once deposition takes place, the MHD flow evolution equation is updated and includes the divergence of the energetic pressure tensor

$$\rho \left( \frac{\partial \mathbf{V}}{\partial t} + \mathbf{V} \cdot \nabla \mathbf{V} \right) = \mathbf{J} \times \mathbf{B} - \nabla P - \nabla \cdot \mathbf{P}_{\text{hot}} . \quad (5.1)$$

Here  $\rho$  is the mass density and  $\mathbf{V}$  is the center of mass flow velocity of the bulk plasma. Formally,  $\mathbf{P}_{\text{hot}}$  is obtained through the second moment of the energetic particle distribution function

$$\mathbf{P}_{\text{hot}} = \int m_{\text{hot}} (\mathbf{v} - \mathbf{V}_{\text{hot}}) (\mathbf{v} - \mathbf{V}_{\text{hot}}) f_{\text{hot}} d^3v , \quad (5.2)$$

thereby closing the MHD flow equation for a system with minority energetic particles. Often times the center-of-mass flow velocity of the energetic particles  $\mathbf{V}_{\text{hot}}$  is neglected. This can become an issue if the density of the energetic particles increases to a significant amount. In a strongly magnetized plasma where the mean free path for particle collisions is large compared to any parameters of the system (dilute plasma), we can use the CGL (Chew-Goldberg-Low) form (Chew et al., 1956) of the pressure

$$\mathbf{P} = \begin{bmatrix} P_{\perp} & 0 & 0 \\ 0 & P_{\perp} & 0 \\ 0 & 0 & P_{\parallel} \end{bmatrix} . \quad (5.3)$$

This can be written more generally, using magnetic field unit vector  $\mathbf{b}$ , as

$$\mathbf{P} = P_{\parallel} \mathbf{b}\mathbf{b} + P_{\perp} (\mathbf{I} - \mathbf{b}\mathbf{b}) . \quad (5.4)$$

The parallel component  $P_{\parallel}$ , and the perpendicular component  $P_{\perp}$  with respect to the magnetic field can each be obtained by the moments of the distribution function using the first and the second adiabatic invariants. They are written as

$$P_{\perp} = \int \mu B f(\mathbf{x}, \mathbf{v}, t) d^3v \quad (5.5)$$

and

$$P_{\parallel} = \int v_{\parallel}^2 f(\mathbf{x}, \mathbf{v}, t) d^3v . \quad (5.6)$$

The first adiabatic invariant corresponds to the magnetic moment  $\mu$  while the second adiabatic invariant is related to the parallel motion of the particle along the magnetic field.

It is important to note that if the population of energetic ions are small compared to the bulk of the plasma, the energetic ion momentum is small compared to that of the plasma. Nevertheless, the pressure from the energetic ions can be large from the  $\mathbf{v}\mathbf{v}$  contribution as seen in Eq. (5.2). In this situation, the  $\delta f$  approach to the energetic ions is valid. Consider a situation where the population of the energetic ions is greater, *e.g.* for ITER  $\sim 30\%$  of the plasma can become energetic  $\alpha$ -particles (Putvinski, 1998). The macroscopic momentum of these energetic ions becomes significant relative to the bulk, which indicates that the  $\delta f$  approach could have issues. Therefore, in order for the hybrid kinetic-MHD model that uses  $\mathbf{P}_{\text{hot}}$  to be valid additional assumptions must be made: (i) the density of energetic particles is much less than the density of the bulk plasma ( $n_{\text{hot}} \ll n_{\text{MHD}}$ ), while (ii) the energy of the energetic particles are significant enough so that the energetic particle plasma- $\beta$  is on the order of the bulk plasma- $\beta$  ( $\beta_{\text{hot}} \sim \beta_{\text{MHD}}$ ).

### 5.1 Initial Setup: Particle Load onto Computational Domain

In PIC, the phase space is populated by computational particles. Particles are placed so as to form a prescribed distribution in space and velocity,  $f_0(\mathbf{x}, \mathbf{v})$ . From the prescribed distributions, the initial position and velocity ( $\mathbf{x}_{0j}, \mathbf{v}_{0j}$ ) for each particle  $j$  are determined using a random number generator. This is the Monte Carlo method where random numbers can be utilized for particle sampling in the computational domain (Birdsall and Langdon, 2018; Hammersley and Handscomb, 1964). The initial conditions for the computational particles, found via the prescribed distribution function, give the starting point for the governing equations of motion, namely Newton's 2<sup>nd</sup> law. Therefore, the initial condition on particle distribution function  $f_0$  is important in determining the behavior of the overall system.

In NIMROD's  $\delta f$ -PIC approach, the sampling of phase space for energetic ions, is done using a slowing down distribution function,  $f_0$ . The slowing down distribution function assumes that these energetic ions have interacted with the bulk thermal electron and ion populations which are Maxwellian distributions. Typically, the thermal velocity of electrons,  $v_{Te}$ , is much greater than that of the ions,  $v_{Ti}$  (where  $v_T = \sqrt{(2k_B T/m)}$ ). The energetic

ions will “feel” a drag from the thermal electrons first, thus slowing down to a critical energy  $\mathcal{E}_c$ . Once the energetic ions reach  $\mathcal{E}_c$ , they begin to interact with the slower thermal ions as well. This sort of process results in heating of the electrons and raising its thermal energy (Helander and Sigmar, 2005). The slowing down distribution function (Kim, 2008) can be expressed as

$$f_0 = \frac{p_0 \exp(p_\varphi/q\psi_n)}{\mathcal{E}^{3/2} + \mathcal{E}_c^{3/2}}, \quad (5.7)$$

where  $p_0$  is a normalization constant,  $\mathcal{E}_c$  is the critical slowing down energy, and  $\langle \mathcal{P}_\varphi \rangle \equiv p_\varphi$  is the gyro-averaged toroidal momentum (see Eq. (3.56)). Here,  $\psi_n$  is chosen for each equilibrium in order to match the shape of the MHD pressure profile. Since the energy dependence of the slowing down distribution function is written in terms of the canonical variables it satisfies Eq. (5.16). Note that the slowing down distribution function arises from solving the Fokker-Planck equation for the energetic beam Coulomb scattering off the background plasma. Thus it makes sense to use it to sample the initial distribution function in phase space. The perturbed ( $\delta f$ ) part of the distribution function is advanced via the weight equation (see Eq. (5.15)).

The  $\delta f$ -PIC in NIMROD samples the phase space via important sampling, *i.e.* a non-uniform sampling, using the condition  $f(t=0) \approx f_0$ . Here, we are assuming  $\delta f \ll f_0$ , where  $\delta f$  is the time dependent perturbed part of the distribution function (see Eq. (5.13)). Therefore, sampling from the steady state distribution function allows us to cover the more “important” part of phase space. In order to sample the physical space, we consider the pressure profile of the equilibrium MHD bulk plasma, which obeys the force balance equation

$$\mathbf{J}_0 \times \mathbf{B}_0 = \nabla P_0. \quad (5.8)$$

The initial pressure is assumed isotropic. Initially, when loading the energetic particles, the equilibrium pressure  $P_{\text{hot}0}$  is constructed to be a fraction of the MHD equilibrium pressure  $P_0$ , namely,

$$P_{\text{hot}0} = \frac{1}{\beta_{\text{frac}}} P_0 = \frac{1}{\beta_{\text{frac}}} (n_e k_B T_e + n_i k_B T_i) \quad (5.9)$$



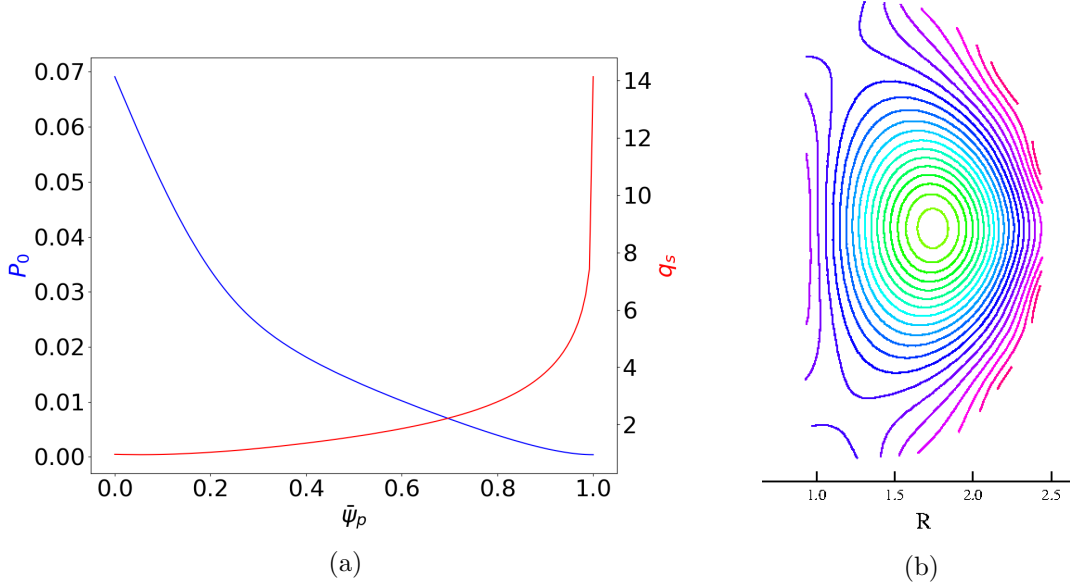


**Figure 5.1:** Figure (a) shows the equilibrium pressure  $P_0$  and the normalized safety factor  $q_s$  vs. the normalized poloidal flux  $\bar{\psi}_p$ . Portion of the plasma where  $q_s < 1$  (roughly at  $\bar{\psi}_p < 0.168$ ) undergoes the 1/1 kink. Figure (b) shows the magnetic flux surface geometry for DIII-D (value decreases from green to red).

where  $\beta_{\text{frac}} = \beta_{\text{hot}}/\beta_{\text{MHD}}$  and we used the ideal gas law for the thermal electrons and ions. This allows us to modify the force balance equation, Eq. (5.8), to include the equilibrium pressure of the energetic particles

$$\mathbf{J}_0 \times \mathbf{B}_0 = (1 - \beta_{\text{frac}}) \nabla P_0 + \nabla P_{\text{hot}0} . \quad (5.10)$$

Note that since the equilibrium pressure for the energetic particles is isotropic, when sampling from Eq. (5.7), the term  $\exp(p_\varphi/q\psi_n)$  is approximated as  $\exp(\psi/\psi_n)$  so as to not yield an anisotropic contribution to the pressure (Kim, 2008). Therefore, the velocity distribution is sampled from

$$f_0 = \frac{p_0 \exp(\psi/\psi_n)}{\mathcal{E}^{3/2} + \mathcal{E}_c^{3/2}} \quad (5.11)$$

and  $p_0$  is used to ensure that the isotropic pressure moment is

$$P_{\text{hot}0} = \int \frac{1}{3} m v^2 f_0 d^3 v = \beta_{\text{frac}} P_0 . \quad (5.12)$$

Sampling the physical space with particles of weight  $w = 1$ , so that it fits the equilibrium pressure profile (see Fig. 5.1) inevitably places more particles near the center of the tokamak since the pressure is greater there. This means that the processors handling the grid blacks near the center, *e.g.* processors 1-4, would have many more particles than the outer processors, *e.g.* processors 9-16. This slows down the code because some processors work much harder than others. Therefore, a load balancing of the particles is done once the computational domain is sampled. The load balancing passes the particles evenly to each processors so that they all have, roughly, the same number. As we saw in Fig. 4.15, the load balanced case ran faster than the case with no load balancing by roughly a factor of 2.

After the particles are sampled in the computational domain, they are advanced along their orbits in time via the PIC algorithm. Then, the pressure tensor in Eq. (5.7) is computed and deposited onto the finite element grid. Finally, the flow is advanced including the energetic particle pressure tensor. In the  $\delta f$ -PIC approach,  $\delta f$  is evolved in time according to the updated particle weights. We now discuss the derivation of the weight evolution equation.

## 5.2 The $\delta f$ -PIC Approach in NIMROD

The  $\delta f$ -PIC method, which can be interpreted as the control variates approach in Monte Carlo schemes (Aydemir, 1994), separates the distribution function into a steady state portion  $f_0$  and some small deviation  $\delta f$  from it

$$f(\mathbf{z}, t) = f_0(\mathbf{z}) + \delta f(\mathbf{z}, t) . \quad (5.13)$$

Here  $\mathbf{z} \doteq (\mathbf{x}, \mathbf{v})$  are the variables in position and velocity space and the steady state part is time independent. We consider the Vlasov equation (see Eq. (2.50))

$$\frac{\partial f}{\partial t} + \dot{\mathbf{z}} \cdot \frac{\partial f}{\partial \mathbf{z}} = 0 \quad (5.14)$$

for the energetic particles, where collisions between themselves or off the bulk plasma are

ignored. We can ignore collisional effects because we are mostly concerned with the microsecond, MHD timescale over which collisions have only a small effect. The collisional timescale is on the order of  $\sim 10^{-3}$  s for energetic ions in a dilute plasma. By sampling from the slowing down distribution function (see Eq. (5.7)) for the equilibrium energetic particle distribution function, we assume that collisions with the bulk plasma have given us the energy dependence in Eq. (5.7) over a millisecond timescale. Then, a fast MHD event, like the sawtooth mode, arises and grows over a much shorter timescale. The evolution of the weights capture this rapid, nearly collisionless  $\delta f$  response in the energetic particle distribution function.

Using Eq. (5.13) and breaking up  $\mathbf{z}$  into the equilibrium and the perturbed parts,  $\mathbf{z} = \mathbf{z}_0 + \delta\mathbf{z}$ , we can obtain a linear expression for the time evolution equation of  $\delta f$ , namely

$$\dot{\delta f} = -\delta\dot{\mathbf{z}} \cdot \frac{\partial f_0}{\partial \mathbf{z}} . \quad (5.15)$$

The steady state distribution function  $f_0$  is constant along the characteristics

$$\frac{\partial f_0}{\partial t} + \dot{\mathbf{z}}_0 \cdot \frac{\partial f_0}{\partial \mathbf{z}} = 0 , \quad (5.16)$$

and the choice of  $f_0$  must satisfy Eq. (5.16).

The slowing down distribution function (see Eq. (5.7)) is in terms of the position  $\mathbf{x}$  and the kinetic energy  $\mathcal{E} = mv^2/2$ . In terms of these variables  $(\mathbf{x}, \mathcal{E})$ , Eq. (5.15) can be expressed as

$$\frac{d\delta f}{dt} = -\delta\dot{\mathbf{x}} \cdot \nabla f_0 - \delta\dot{\mathcal{E}} \partial_{\mathcal{E}} f_0 , \quad (5.17)$$

where we have expanded  $\mathbf{x} = \mathbf{x}_0 + \delta\mathbf{x}$  and  $\mathcal{E} = \mathcal{E}_0 + \delta\mathcal{E}$  into their equilibrium and perturbed parts. We use the drift kinetic model for  $\delta\dot{\mathbf{x}}$  in Eq. (5.17); therefore,  $\delta\dot{\mathbf{x}} = \delta\mathbf{v}_{\text{gc}}$ , the perturbed guiding center velocity. Instead of using the form given in Eq. (2.55), which is in terms of the magnetic curvature,

$$\mathbf{v}_{\text{gc}} = v_{\parallel} \mathbf{b} + \frac{\mathbf{E} \times \mathbf{B}}{B^2} + \frac{1}{\Omega} \mathbf{b} \times \left( v_{\parallel} \frac{\partial \mathbf{b}}{\partial t} + v_{\parallel}^2 \boldsymbol{\kappa} + \frac{v_{\perp}^2}{2} \frac{\nabla B}{B} \right) ,$$

we will express the guiding center velocity using the current density. The magnetic curvature vector  $\boldsymbol{\kappa}$  can be expressed in terms of the current density via the pre-Maxwell form of Ampere's law,

$$\boldsymbol{\kappa} = \mu_0 \frac{\mathbf{J} \times \mathbf{B}}{B^2} + \frac{1}{B} \nabla_{\perp} B . \quad (5.18)$$

Once Eq. (5.18) is plugged into the expression for  $\mathbf{v}_{\text{gc}}$  and rearranged, we get a form that can be more easily be implemented into NIMROD,

$$\mathbf{v}_{\text{gc}} = v_{\parallel} \mathbf{b} + \frac{\mathbf{E} \times \mathbf{B}}{B^2} + \frac{m}{qB^4} \left( v_{\parallel}^2 + \frac{v_{\perp}^2}{2} \right) \left( \mathbf{B} \times \nabla \left( \frac{B^2}{2} \right) \right) + \frac{\mu_0 m v_{\parallel}^2}{qB^2} \mathbf{J}_{\perp} + \frac{m v_{\parallel}}{qB} \mathbf{b} \times \frac{\partial \mathbf{b}}{\partial t} . \quad (5.19)$$

This form of the guiding center velocity is more convenient since the current density, rather than the magnetic curvature, is readily available in NIMROD. Recall that we need the perturbed quantity  $\delta \mathbf{v}_{\text{gc}}$  for Eq. (5.17); therefore, we linearize Eq. (5.19). The equilibrium fields are assumed to be time independent. Additionally, the equilibrium electric field is assumed to be zero,  $\mathbf{E}_0 = 0$ . The result for the equilibrium guiding center velocity is

$$\mathbf{v}_{\text{gc}0} = v_{\parallel} \mathbf{b}_0 + \frac{m}{qB_0^4} \left( \frac{v_{\perp}^2}{2} + v_{\parallel}^2 \right) \left( \mathbf{B}_0 \times \nabla \left( \frac{B_0^2}{2} \right) \right) + \frac{\mu_0 m v_{\parallel}^2}{qB_0^2} \mathbf{J}_{0\perp} . \quad (5.20)$$

Notice that the  $E \times B$  drift does not appear in the equilibrium term due to  $\mathbf{E}_0 = 0$ . Also,  $\partial \mathbf{b}_0 / \partial t = 0$  since the equilibrium fields are time independent.

Linearizing  $\delta \mathbf{v}_{\text{gc}}$ , *i.e.* only considering first-order terms yields

$$\begin{aligned} \delta \mathbf{v}_{\text{gc}} = v_{\parallel} \delta \mathbf{b} + \frac{\delta \mathbf{E} \times \mathbf{B}_0}{B_0^2} + \frac{m}{qB_0^3} \left( \frac{v_{\perp}^2}{2} + v_{\parallel}^2 \right) \left( \mathbf{B}_0 \times \nabla \delta B + ((\mathbf{I} - 3\mathbf{b}_0 \mathbf{b}_0) \cdot \delta \mathbf{B}) \times \nabla B_0 \right) \\ + \frac{\mu_0 m v_{\parallel}^2}{qB_0^2} \left( \delta \mathbf{J}_{\perp} - \frac{2(\mathbf{B}_0 \cdot \delta \mathbf{B})}{B_0^2} \mathbf{J}_{0\perp} \right) + \frac{m v_{\parallel}}{qB_0} \mathbf{b}_0 \times \frac{\partial \delta \mathbf{b}}{\partial t} . \end{aligned} \quad (5.21)$$

A simplified expression is implemented in the  $\delta f$ -PIC formulation in NIMROD (Kim, 2008),

$$\delta \mathbf{v}_{\text{gc}} = v_{\parallel} \delta \mathbf{b} + \frac{\delta \mathbf{E} \times \mathbf{B}_0}{B_0^2} . \quad (5.22)$$

Note that the  $E \times B$  drift term still appears in the reduced, perturbed guiding center velocity

because it is technically a  $B_0^{-1}$  term. Here the existing implementation use  $\delta\mathbf{b} \approx \delta\mathbf{B}/B_0$ . If we were to carefully linearize the perturbed magnetic unit vector, we would end up with an extra term,  $\delta\mathbf{b} = (\mathbf{I} - \mathbf{b}_0\mathbf{b}_0) \cdot \delta\mathbf{B}/B_0$ , where  $\mathbf{I}$  is the identity matrix.

We now consider the  $\delta\dot{\mathcal{E}}$  term in Eq. (5.17), where recall that  $\mathcal{E} = mv^2/2$  is the kinetic energy. The time derivative of the kinetic energy gives us the work that is done on the particle by the electromagnetic field. Since the magnetic field does not contribute to the energy change,

$$\frac{d\mathcal{E}}{dt} = \frac{d\mathbf{v}}{dt} \cdot \frac{\partial\mathcal{E}}{\partial\mathbf{v}} = q\mathbf{v} \cdot \mathbf{E} . \quad (5.23)$$

Therefore, the first-order perturbation for Eq. (5.23), recalling that  $\mathbf{E}_0 = 0$ , gives

$$\delta\dot{\mathcal{E}} = q\mathbf{v}_{\text{gc}0} \cdot \delta\mathbf{E} . \quad (5.24)$$

Using the results given above, Eq. (5.17) can be written as

$$\dot{\delta f} = -\delta\mathbf{v}_{\text{gc}} \cdot \nabla f_0 - q\mathbf{v}_{\text{gc}0} \cdot \delta\mathbf{E} \partial_{\mathcal{E}} f_0 . \quad (5.25)$$

Equation (5.25) gives the time evolution for  $\delta f$  in the new coordinates  $(\mathbf{x}, \mathcal{E})$  for the drift kinetic regime. By solving this equation, we are able to obtain  $\delta f$  at each time step through updating the particle weights,  $w_j = \delta f/f_0$ . What remains is to find the derivatives of  $f_0$  (see Eq. (5.7)) in the coordinates  $(\mathbf{x}, \mathcal{E})$ . This calculation yields

$$\nabla f_0 = -\frac{mgf_0}{qv_{\parallel}B^2\psi_p} \left( v_{\parallel}^2 + \frac{v_{\perp}^2}{2} \right) \nabla B - \frac{f_0}{\psi_n} \left( \nabla\psi_n - \frac{mv_{\parallel}}{qB} \nabla g \right) \quad (5.26)$$

and

$$\partial_{\mathcal{E}} f_0 = \frac{gf_0}{qv_{\parallel}B\psi_n} - \frac{3}{2} \frac{f_0\mathcal{E}^{1/2}}{\mathcal{E}^{3/2} + \mathcal{E}_c^{3/2}} , \quad (5.27)$$

where  $g = RB_{\varphi}$  and Eq. (3.62) was used for  $v_{\parallel}$ . For more details on the above expressions see Kim (2008). For a similar implementation of the hybrid approach in a different code (M3D-C1-K) see ?.

### 5.2.1 Deposition of Energetic Particle Pressure Tensor

The energetic particle physics is merged with the fluid MHD model via the energetic particle pressure tensor  $\mathbf{P}_{\text{hot}}$  in NIMROD's  $\delta f$ -PIC formulation. In order to obtain the pressure tensor, a moment of the distribution function is taken (see Eq. (5.2))

$$\mathbf{P}_{\text{hot}} = P_{0\text{hot}}\mathbf{I} + \int m_{\text{hot}} (\mathbf{v} - \mathbf{V}_{\text{hot}}) (\mathbf{v} - \mathbf{V}_{\text{hot}}) \delta f d^3v, \quad (5.28)$$

where we have used Eq. (5.13) and assumed isotropic pressure for the equilibrium. The second term on the right is the perturbed pressure tensor  $\delta\mathbf{P}_{\text{hot}}$ . Note that the pressure tensor is defined as a second moment of the distribution function and uses the random velocity  $\mathbf{w} = \mathbf{v} - \mathbf{V}_{\text{hot}}$ , where  $\mathbf{V}_{\text{hot}}$  is the center-of-mass flow velocity for the energetic particles. The energetic particle pressure tensor is then used in the MHD momentum equation to update the flow evolution of the bulk plasma

$$\rho \left( \frac{\partial \mathbf{V}}{\partial t} + \mathbf{V} \cdot \nabla \mathbf{V} \right) = \mathbf{J} \times \mathbf{B} - \nabla \cdot \mathbf{P} - \nabla \cdot \mathbf{P}_{\text{hot}}. \quad (5.29)$$

It is important to note that if the population of energetic ions is small compared to the bulk of the plasma, the energetic ion momentum is small compared to the rest of the plasma momentum. Nevertheless, the pressure from the energetic ions can be large from the  $\mathbf{v}\mathbf{v}$  contribution in the definition of  $\delta\mathbf{P}_{\text{hot}}$ . In this situation, the  $\delta f$  approach for energetic ions is valid.

We see that in order to introduce the effects of the energetic particles into an MHD plasma,  $\mathbf{P}_{\text{hot}}$  needs to be updated. This is done using Eq. (5.28), where the evolving  $\delta f$  is obtained via Eq. (5.25). To add a little more subtlety we express  $\delta f$  in term of the Kilmontovich representation

$$\delta f = \sum_j^N g_0 \bar{w}_j \delta^3(\mathbf{x} - \mathbf{x}_j) \delta^3(\mathbf{v} - \mathbf{v}_j). \quad (5.30)$$

Here,  $j$  represents a particular computational particle. The Kilmontovich representation is

composed of all the particle positions, velocities, corresponding weights  $\bar{w}_j$ , and uses a point particle,  $\delta$ -function representation. The scaling factor  $g_0$  is used to reproduce the desired fraction of the MHD pressure profile. Plugging Eq. (5.30) into Eq. (5.28) and integrating with the Dirac delta, we get

$$\delta\mathbf{P}(\mathbf{x}) = \sum_{j=1}^N g_0 m_j \bar{w}_j \delta^3(\mathbf{x} - \mathbf{x}_j) (\mathbf{v}_j - \mathbf{V}) (\mathbf{v}_j - \mathbf{V}) , \quad (5.31)$$

where  $\bar{w}_j = w_j/g_0$  is some normalized weight and the subscript "hot" has been suppressed for simplicity. Therefore, when Eq. (5.25) is used to update  $\delta f$ , we are actually updating the weight  $\bar{w}_j$  that is used for the deposition.

In NIMROD, cylindrical coordinates  $(R, Z, \varphi)$  are used, where the right-hand rule applies in the order that the variables are written. The poloidal plane, i.e.  $(R, Z)$ , is expanded in the finite element basis and the toroidal direction  $\varphi$  is expanded in the Fourier representation. The Dirac delta function in these coordinates is

$$\delta^3(\mathbf{x} - \mathbf{x}_j) = \frac{1}{R} \delta(R - R_j) \delta(Z - Z_j) \delta(\varphi - \varphi_j) . \quad (5.32)$$

We discuss this form in Appendix A. Plugging this into Eq. (5.30) and introducing the Fourier expansion in the toroidal direction yields

$$\begin{aligned} \delta\mathbf{P}(R, Z, \varphi) &= \sum_{j=1}^N (\mathbf{v}_j - \mathbf{V}) (\mathbf{v}_j - \mathbf{V}) \\ &\quad \times \frac{g_0 m_j \bar{w}_j}{R} \delta(R - R_j) \delta(Z - Z_j) \left( \frac{1}{2\pi} \int \delta(\varphi - \varphi_j) e^{-in\varphi} R d\varphi \right) . \end{aligned}$$

In the Fourier representation, a factor of  $R$  is introduced in the integral to correctly integrate over the spatial volume. The above expression for  $\delta\mathbf{P}$  simplifies to

$$\delta\mathbf{P}_n(R, Z) = \frac{1}{2\pi} \sum_{j=1}^N (\mathbf{v}_j - \mathbf{V}) (\mathbf{v}_j - \mathbf{V}) g_0 m_j \bar{w}_j \delta(R - R_j) \delta(Z - Z_j) e^{in\varphi_j} , \quad (5.33)$$

where the particle's  $\varphi$  information has been projected onto the Fourier mode  $n$ . The above expression is the Fourier transform of  $\delta\mathbf{P}$ , thus

$$\delta\mathbf{P}_n = \frac{1}{2\pi} \int \delta\mathbf{P} e^{-in\varphi} d\varphi \quad (5.34)$$

where

$$\delta\mathbf{P} = \sum_n \delta\mathbf{P}_n . \quad (5.35)$$

The  $(R, Z)$  components of  $\delta\mathbf{P}$  are now expanded in the finite element basis  $\alpha_k$ , with the spatial basis expressed as  $\mathbf{e}_\ell$ . Here  $k$  represents the finite element expansion and  $\ell$  represents the vector direction, i.e.  $\hat{\mathbf{x}}$ ,  $\hat{\mathbf{R}}$ , etc.; thus the expansion in the basis gives

$$\delta\mathbf{P}_n(R, Z) = \sum_{k, \ell, m} L_k^p \mathbf{e}_\ell \mathbf{e}_m (\delta P_{k\ell mn} e^{in\varphi} + \delta P_{k\ell mn}^* e^{-in\varphi}) = \sum_k \delta\mathbb{P}_k^n L_k^p(R, Z) \quad (5.36)$$

where

$$\delta\mathbb{P}_k^n \equiv \sum_{\ell, m} \mathbf{e}_\ell \mathbf{e}_m (\delta P_{k\ell mn} e^{in\varphi} + \delta P_{k\ell mn}^* e^{-in\varphi}) . \quad (5.37)$$

Since this is a tensor, we have two vector basis indices  $\ell$  and  $m$ . The  $\mathbb{P}_k^n$  are the coefficients of Fourier mode  $n$  at a finite element node indicated by  $k$  that has the corresponding spatial basis that gives the tensor components.

Now that we have both the finite element and the PIC representation for the energetic particle pressure, we can set the two equal to each other and put it into the weak form by multiplying by a test function  $\alpha_{k'}$  and integrating. By doing so we get an expression that yields the coefficients of the pressure at the finite element nodes

$$\delta\mathbb{P}_k^n = M_{kk'}^{-1} \sum_{j=1}^N g_0 m_j \bar{w}_j (\mathbf{v}_j - \mathbf{V}) (\mathbf{v}_j - \mathbf{V}) L_{k'}^p(R_j, Z_j) \frac{e^{-in\varphi_j}}{2\pi} . \quad (5.38)$$

Here,  $M_{kk'}^{-1}$  is the inverse of the finite element mass matrix. Using the above equation we can deposit the weights of the energetic particles onto the finite element grid. Note that we have included the energetic ion flow throughout the derivation of  $\delta\mathbb{P}_k^n$ . The  $\delta\mathbf{f}$ -PIC routine



in NIMROD assumes that the flow is negligible. Therefore, the deposition is simpler where the scalars in Eqs. (5.5) and (5.6) are computed from  $\delta f$  instead, namely,

$$\delta P_{\perp} = \int \mu B \delta f d^3v \quad (5.39)$$

and

$$\delta P_{\parallel} = \int v_{\parallel}^2 \delta f d^3v . \quad (5.40)$$

### 5.3 Numerical Results from NIMROD PIC Simulations

At this point, we include linear results that compare NIMROD's fluid and hybrid fluid/kinetic-PIC predictions of the giant sawteeth observed on the DIII-D tokamak. The energetic particles in the continuum approach in NIMROD used the initial energy dependence shown in Fig. 5.2 on the right. The simulations given below sample from the slowing down part only and do not have the RF tail of the energetic particle distribution. These ideal (zero resistivity) simulations were performed with  $mx \times my = 80 \times 48 = 3,840$  finite element cells (the same as was presented in Fig. 4.1b) and a poloidal block decomposition of  $nxb1 = 16$  and  $nyb1 = 12$ . NIMROD performs linear calculations like these with relative ease. Here we used 6 Cori Haswell nodes at NERSC (National Energy Research Scientific Computing Center) for a total of  $16 \times 12 = 192$  cores and the run times for all three cases presented below took about a minute. Note, the hybrid fluid/kinetic-PIC simulations that we present later are significantly more computationally intensive. Figure 5.1 shows the magnetic flux surface geometry on the right, and the temperature, density and  $q_s$  profiles on the left. Although MHD codes often assume a close, conducting wall at the last closed flux surface, here we keep the open flux region, an approximate vacuum region with open magnetic field lines that intersect the DIII-D wall. In NIMROD PIC simulations, particles that drift across the divertor separatrix most often rapidly travel along magnetic field lines to the wall and are assumed lost.

For this discharge, the central toroidal magnetic field strength, electron density and electron temperature were  $B_T = 1.925$  T,  $n_e = 4.18 \times 10^{19} \text{ m}^{-3}$  and  $T_e = 4106$  eV,

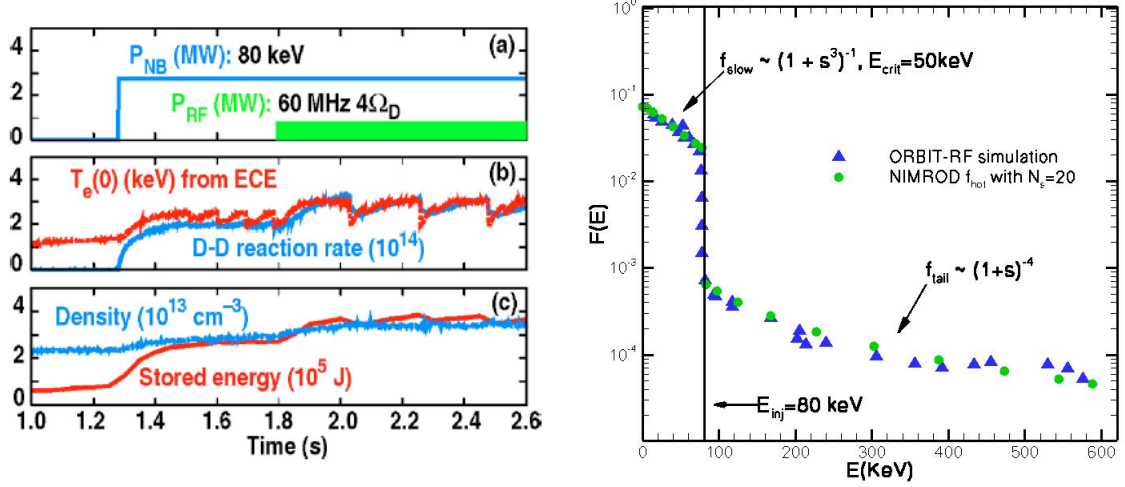


**Figure 5.2:** (Left) shows data from DIII-D experiment, discharge #96043. (a) Time at which the neutral beam and the RF wave were injected into the plasma. (b) Electron central temperature and neutron reaction rate vs. time. (c) Plasma density and plasma stored energy given as functions of time. (Right) shows the energy dependence of the energetic particle distribution function. It shows the energetic slowing down distribution function  $f_{\text{slow}} \sim (1 + s^3)^{-1}$ ,  $E_{\text{crit}} = 50 \text{ keV}$  and the more energetic tail  $f_{\text{tail}} \sim (1 + s)^{-4}$  driven by RF waves. Here the injection energy of the neutral beam,  $E_{\text{inj}} = 80 \text{ keV}$ . The left figure figure was taken from Choi et al. (2007).

respectively. The Alfvén time (roughly, the time it takes for shear Alfvén waves to propagate across the domain) was  $\tau_A = 3.8 \times 10^7 \text{ s}$ . NIMROD uses a semi-implicit leapfrog algorithm to take time steps that are long compared to the compressional Alfvén time, which is roughly ten times larger than the shear Alfvén time (Sovinec et al., 2004). Each of the above cases were run for 4000 steps with a time step,  $\text{dtm} = 1.0 \times 10^{-7} \text{ s}$ , until a dominant, unstable 1/1 eigenmode was obtained.

Time traces of NIMROD’s fluid prediction for the 1/1 ideal kink growth rate for this DIII-D giant sawteeth case are shown in Fig. 5.2. Here we performed a scan in polynomial order (polynomial degree 1, 2, and 4) using NIMROD’s 2D Lagrange finite element basis reconstruction of the DIII-D equilibrium. Recall that the ideal 1/1 mode is a kinking of the plasma column inside the  $q_s = 1$  surface that leads to rapid crashes in the core electron temperature. These are shown in the time traces of DIII-D discharge #96043 in Fig. 5.2 on the left. We take the force balance equilibrium from the reconstruction at  $t = 1900 \text{ ms}$ ,

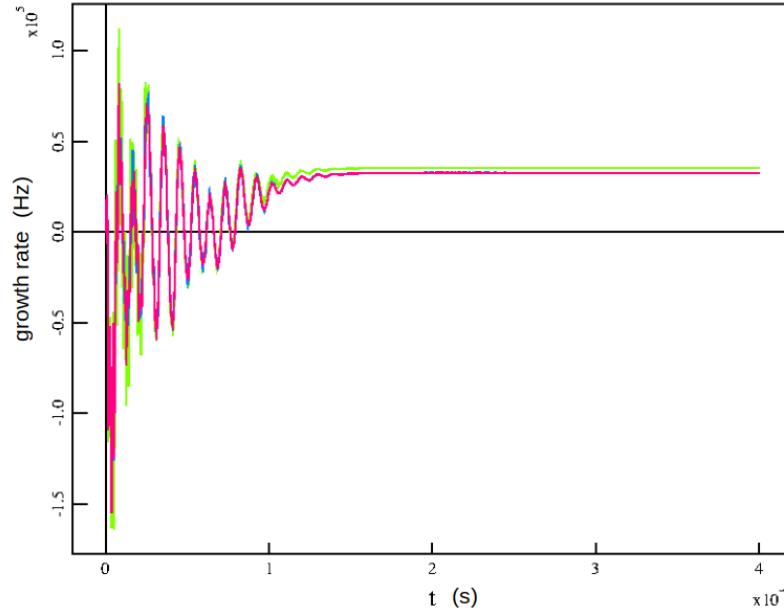


**Figure 5.3:** Shows the growth rate vs. time graph for the ideal fluid only calculation. Polynomial degree 1 (green) has a growth rate of  $\gamma = 35,344$  Hz, polynomial degree 2 (blue under pink) has a growth rate of  $\gamma = 32,810$  Hz, and polynomial degree 4 (pink) has growth rate of  $\gamma = 32,809$  Hz.

after the RF waves have been used to drive the energetic ions to energies around 600 keV, but just before the first giant sawtooth around  $t = 2000$  ms. Rapid convergence in the fluid-only growth rate is obtained with the polynomial degree 2 and 4 cases almost lying on top of each other (see Fig. 5.3).

The growth rates are computed using the log of the total (kinetic, magnetic, and internal) MHD energy. The error in the divergence of the magnetic field ( $\text{div}(\mathbf{B})$  diagnostic versus  $t$ ) shows how higher-order finite elements do a better job of preserving the law of no magnetic monopoles. Although there are exact algorithms for enforcing  $\nabla \cdot \mathbf{B} = 0$ , NIMROD's algorithm instead adds a diffusive term to Faraday's law ( $\partial \mathbf{B} / \partial t = -\nabla \times \mathbf{E}$ ) to diffuse  $\text{div}(\mathbf{B})$  error out of the computational domain and keep it at a tolerable level.

Finally, for the ideal fluid only calculation, we present the eigenfunctions using contours of the  $R$ -component of the plasma flow,  $V_R$ , and the electron temperature,  $T_e$ . The top row shows the results for the polynomial degree 1 case and the bottom row shows them for the polynomial degree 4 case (see Fig. 5.5). In terms of physics, the linear flow response

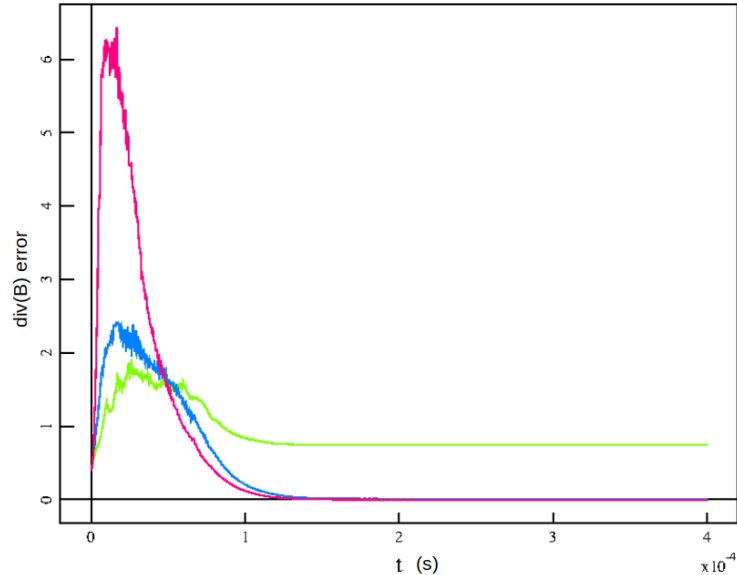


**Figure 5.4:** Shows the error in divergence of magnetic field ( $\text{div}(\mathbf{B})$ ) vs. time graph, *i.e.*  $\text{div}(\mathbf{B})$  diagnostic plot. The polynomial degree 1 (green) case has much greater error associated with the converged eigenfunction. The polynomial degree 2 (blue) and 4 (green) do a better job preserving  $\nabla \cdot \mathbf{B} = 0$  condition beyond  $10^{-4}$  seconds.

inside the  $q_s = 1$  surface (roughly  $1.5 < R < 2$  m, see Fig. 4.1 where the finite element is more finely packed on the 1/1 surface) is outward both above and below the magnetic axis, indicating an outward shift of the plasma at toroidal angle  $\phi = 0$ . A plot at  $\phi = \pi/2$  would show a down shift from the  $Z$ -component of the plasma flow,  $V_Z$ . A plot at  $\phi = \pi$  would show an inward shift and  $\phi = 3\pi/2$  would show an upward shift, thus displaying the Fourier mode,  $n = 1$  signature of the 1/1 kink.

Nonlinear simulations are necessary to actually observe the dynamics of the kink in a NIMROD simulation. This includes the actual sawtooth behavior with electron thermal energy being ejected from inside the  $q_s = 1$  surface. Although the amplitudes are arbitrary (since we could continue to evolve the linearly growing eigenfunction), a comparison of the values between polynomial degree 1, 2, and 4 (polynomial degree 2 calculations not shown) indicates that polynomial degree 1 is under-resolved, although they do resemble the polynomial degree 4 cases in Fig. 5.5 and the polynomial degree 2 and 4 cases agree quite nicely with each other. We now present the results for the hybrid fluid/kinetic-PIC simulations that aim to show increased stabilization using a slowing down distribution

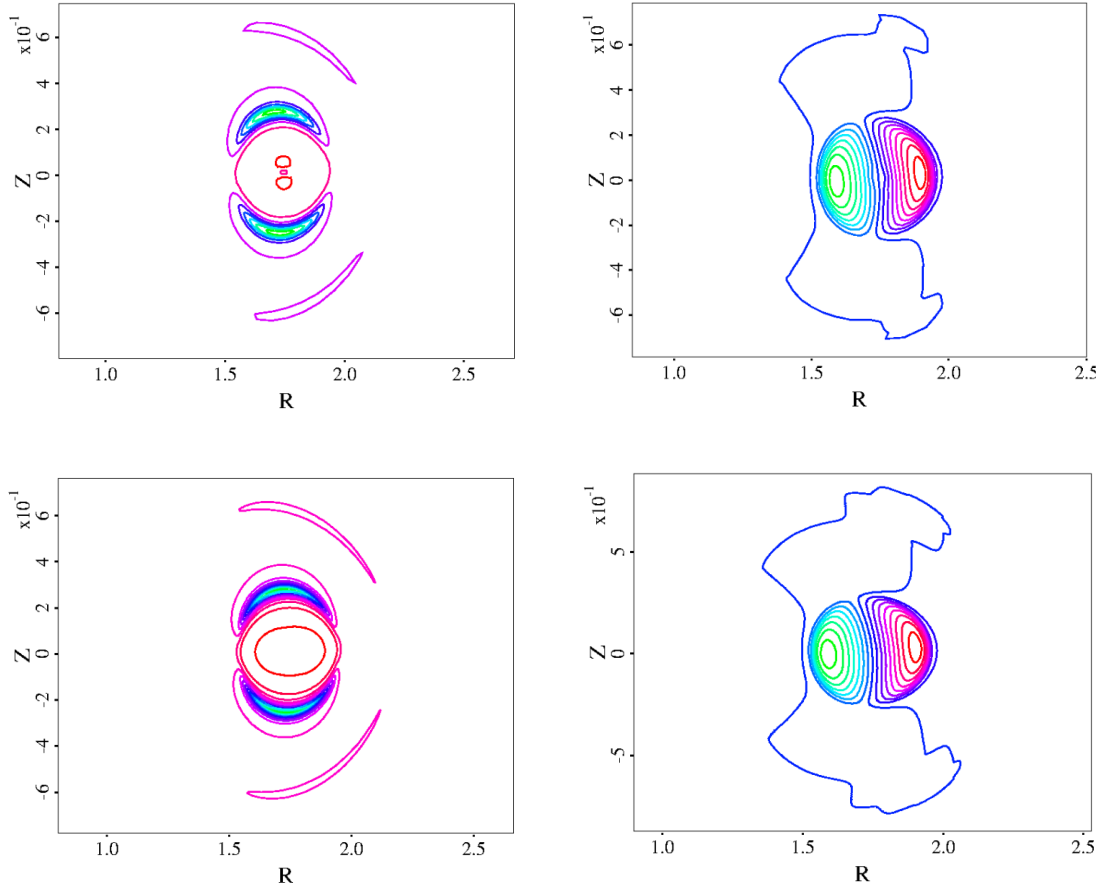


**Figure 5.5:** (Top left) Contour plot of  $V_R$  for polynomial degree 1 case. (Top right) Contour plot of  $T_e$  for polynomial degree 1 case. (Bottom left) Contour plot of  $V_R$  for polynomial degree 4 case. (Bottom right) Contour plot of  $T_e$  for polynomial degree 4 case.

as  $\beta_{\text{frac}} = \beta_{\text{hot}}/\beta_{\text{MHD}}$  is increased from 0 to 0.6. First, calculations with  $\beta_{\text{frac}} = 0.2$  were performed with different number of particles (see Fig. 5.6). The plasma is stabilized by using a slowing down distribution function for the energetic ion population. Particle simulations are inherently noisy (as an example, compare the pure fluid calculation to the rest of the traces in Fig. 5.6), but by introducing more particles we can decrease the noise. Here the sequence for the number of particles is  $8 \times 10^4$  (green),  $8 \times 10^5$  (blue), and  $8 \times 10^6$  (purple).

In Chapter 4, we gave runtime results for the load-balanced and the not load-balanced cases (see Fig. 4.15). Figure 5.7 shows the results of particles per processor for load-balanced (left) and not load-balanced (right) where 8 million particles were used for the simulation.

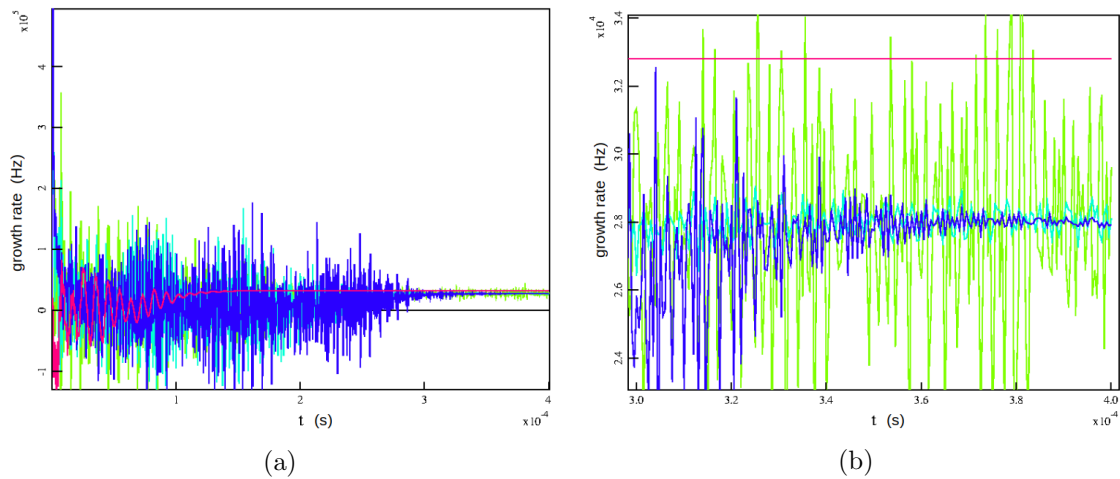


**Figure 5.6:** Figure (a) shows the growth rate of four different calculations. Figure (b) shows the blow up of the converged part of the growth rate plot. The fluid only calculation (pink) is given as a reference to show that with energetic particles present the growth rate is slightly lower. This shows increased stabilization using a slowing down distribution with  $\beta_{\text{frac}} = 0.20$ . Note that with increasing particle number for the simulation the noise of the particle simulation goes down (blue, green, and teal).

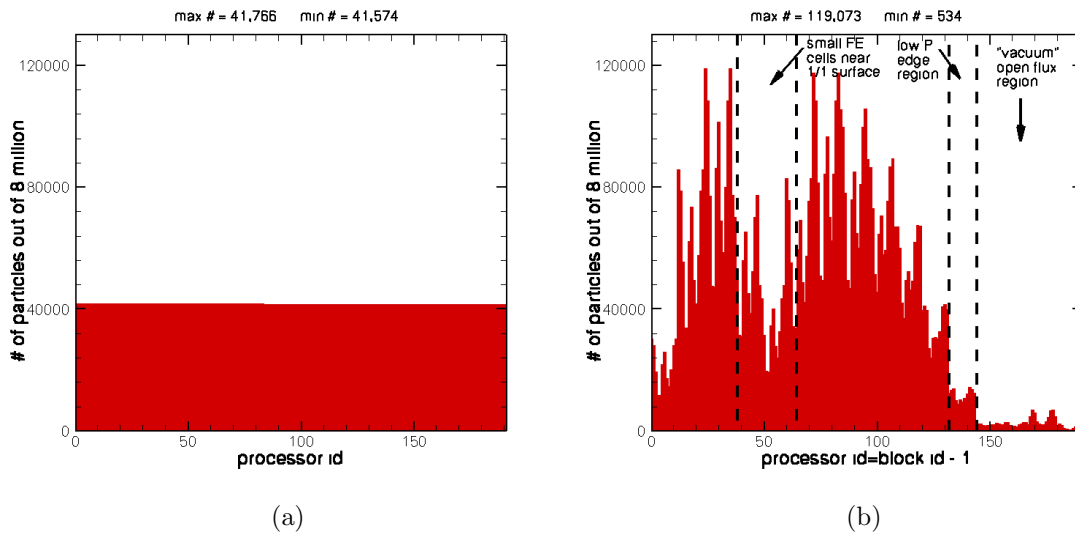


**Figure 5.7:** Figure (a) shows the load-balanced case. Particle distribution among processors is uniform where the processor with the maximum number of particles has 41,766 and the processor with the minimum number of particles has 41,574. Figure (b) shows the not load-balanced case. We can see that the outer, low pressure region has very few particles while the core with the highest pressure has the most particle per processor. At the 1/1 surface, the particle per processor amount drops due to the smaller finite element cells used combined with the technique of importance sampling. For both cases 8 million particles were used.

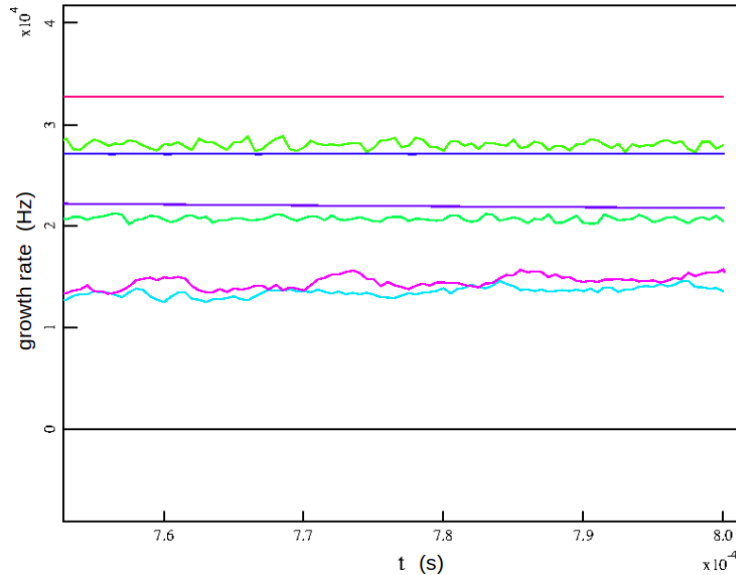


**Figure 5.8:** Compares the growth rates for the PiC and newpart routines. The top most pink line (above 30,000 Hz) is the growth rate for fluid only calculation. The two calculations right below 30,000 Hz are the growth rates for PiC (green) and newpart (blue) for  $\beta_{\text{frac}} = 0.2$ . The two calculations right above 20,000 Hz are the growth rates for PiC (green) and newpart (purple) for  $\beta_{\text{frac}} = 0.4$ . Finally, the two calculations right above 10,000 Hz are the growth rates for PiC (teal) and newpart (magenta) for  $\beta_{\text{frac}} = 0.6$ .

We can see that the load-balanced case gives us a uniform distribution of particles for each processor, which ultimately helps in runtime.

On the other hand, the not load-balanced case leads to a very uneven distribution of particles on various processors. Due to how the particles are initially sampled, the low pressure regime of the tokamak has very few particles while the processors handling the core have a large load. Also, notice that near the 1/1 surface, fewer particles are loaded since the finite element cells there are smaller due to the fact that we want higher spatial resolution near the 1/1 surface in order to better resolve the eigenfunction. Lastly, even though load-balancing leads to evenly distributed particles, it requires global field and  $(R, Z)$  data for the particle push and find throughout the computational domain as discussed in Chapter 4. This results in additional structures and storage in the code (see Fig.4.14).

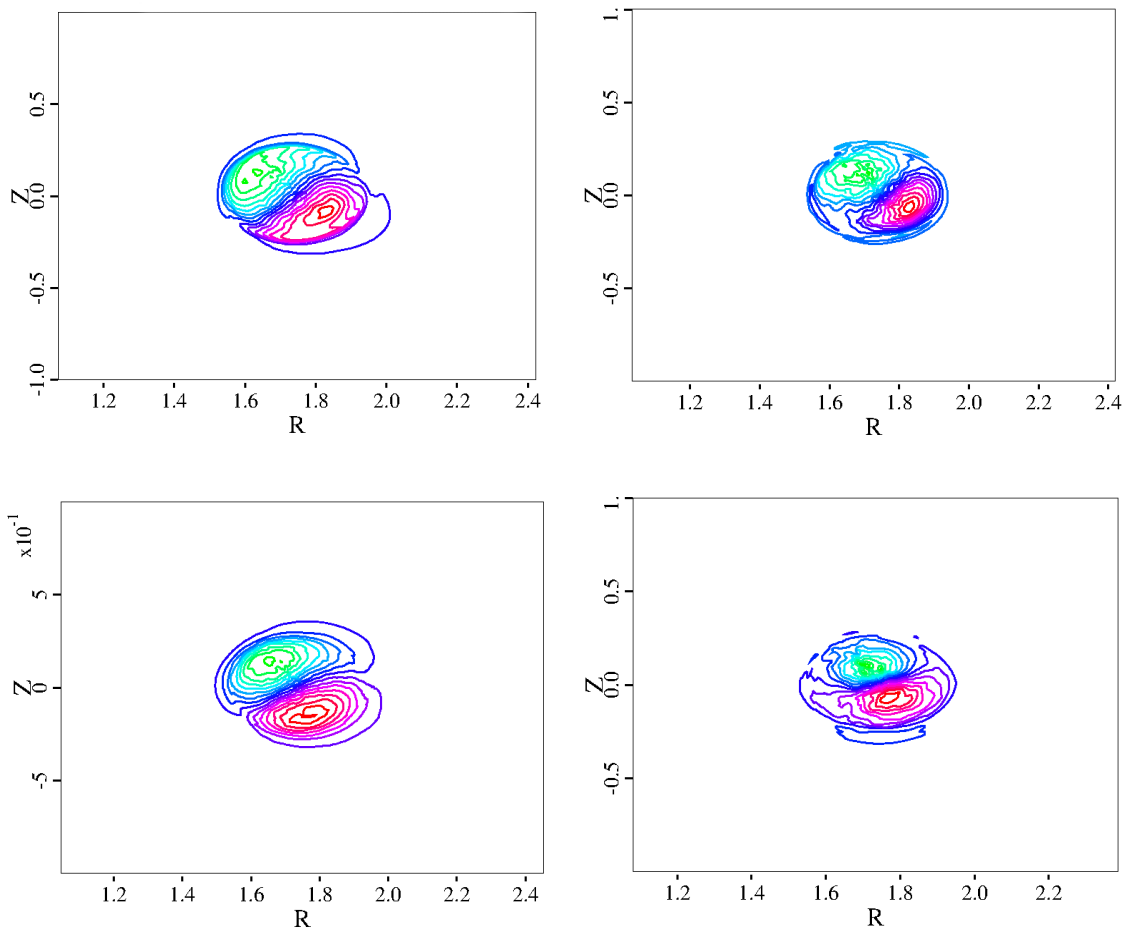


**Figure 5.9:** Pressure contour plots for the newpart using a representation in the push (evaluation of fields) and find (mapping from real to logical coordinates). (Top left) Contour plot of  $\delta P_{\perp}$  for newpart bilinear. (Top right) Contour plot of  $\delta P_{\text{ani}}$  for newpart bilinear. (Bottom left) Contour plot of  $\delta P_{\perp}$  for PiC bilinear. (Bottom right) Contour plot of  $\delta P_{\text{ani}}$  for PiC bilinear. The contour plots were taken at 4000 time steps and show similar structure.

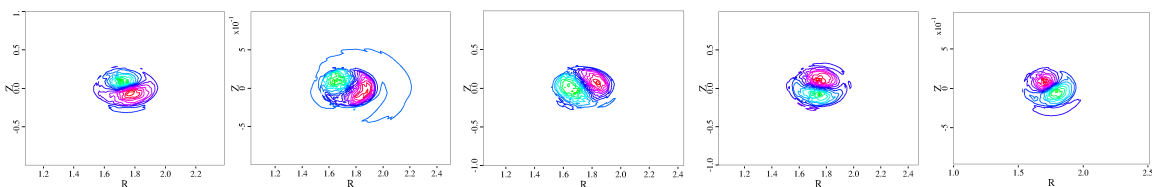


**Figure 5.10:** Contour plots of the anisotropic part of the pressure tensor,  $\delta P_{\text{ani}}$ , 4000, 5000, 6000, 7000, and 8000 time steps indicate a propagating mode with the anisotropic pressure contours rotating in a counter-clockwise direction in the poloidal plane.



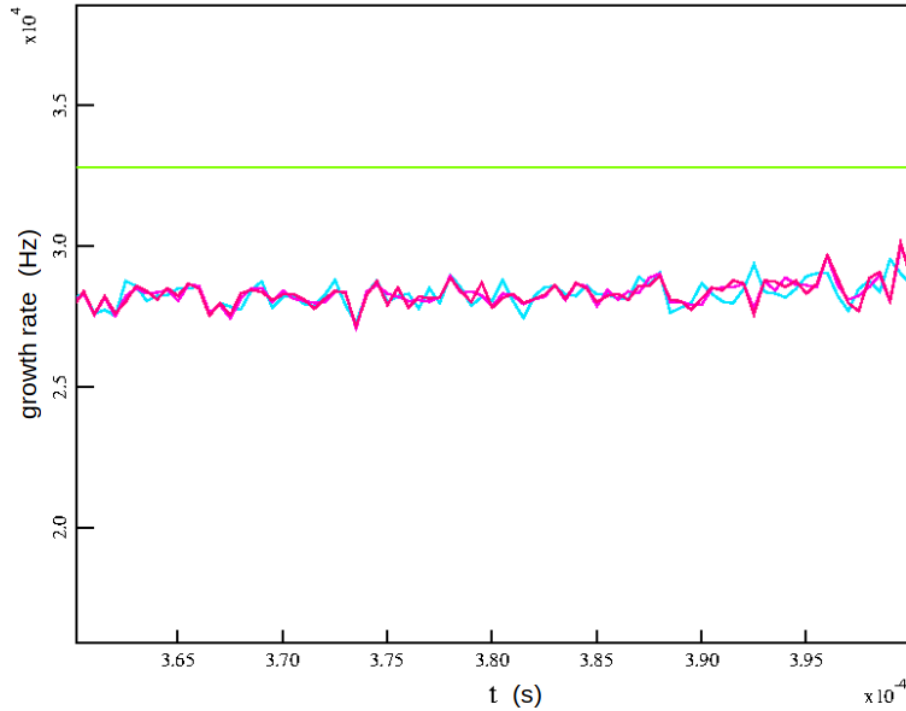


**Figure 5.11:** Shows the blow up of the growth rate for fluid only (green), bilinear (purple), biquadratic (magenta), and complete biquartic (teal). The higher-order bases do not have an effect on the 1/1 internal kink mode.

We now present results from NIMROD’s PIC routine, as presented in [Kim \(2008\)](#) (which we will call PiC), and NIMROD’s PIC routine with the load-balancing capability and the Serendipity basis function implementation (which we will call newpart). [Figure 5.8](#) compares the growth rates between newpart and PiC where  $\beta_{\text{frac}} = 0$ , *i.e.* fluid only calculation (top most line that is red), is given as a reference to show the stabilizing effect of energetic ions on the ideal, kink 1/1 growth rate. We see that the results between PiC and newpart are similar and the scan in  $\beta_{\text{frac}}$  shows that the linear growth rate decreases with the introduction of an energetic ion slowing down distribution function.

Further analysis using the contour plots of  $\delta P_{\perp}$  and  $\delta P_{\text{ani}} = \delta P_{\parallel} - \delta P_{\perp}$ , again verify that bilinear newpart and PiC are getting very similar answers (values at the top and structure of the contours), where  $\delta P_{\text{ani}}$ , (see [Fig. 5.9](#)). The anisotropic part of the pressure modifies the stability from just having an isotropic pressure from an energetic ion population. If one does the linear theory ([Fu et al., 2006](#)), one finds that not only is  $\delta P_{\text{ani}}$  initially stabilizing

(reduces the growth rate), but it also leads to a real frequency, *i.e.* a propagating (rotating) mode (see Fig. 5.10). The ideal 1/1 kink with only MHD and isotropic pressure does not have a real frequency, thus the rotating mode is one of the interesting phenomenon that comes about because of the anisotropic part of the pressure tensor.

Finally, we compare growth rate calculations using a sequence of Serendipity basis function. The bilinear (biline), Serendipity biquadratic (biquad), and complete Serendipity biquartic (cmplt4) were considered for the comparison. Again, in Fig. 5.11 we show the fluid only growth rate as a reference. Unfortunately, the higher-order Serendipity basis sets have little effect on the growth rates. Perhaps the biggest reason for this is that a core mode like the 1/1 internal kink does not depend so much on improving the trajectories and reducing false particles losses. Hence, it does not effect core fluid modes. However, if we were to utilize the higher-order Serendipity basis for edge localized modes or for the ion orbit loss problem, perhaps improving the particle trajectories could have more of an effect. The bottom line is that a numerical method that may work in one study does not necessarily work for another. Proper methods must be carefully chosen to obtain meaningful results.

## CHAPTER 6

### CONCLUSION AND FUTURE WORK

Energetic particles interacting with magnetohydrodynamic (MHD) modes represents crucial physics that must be understood in magnetic fusion devices such as tokamaks. In these devices, a neutral beam is used to impart momentum and energy to the plasma and RF waves are used to further increase the energy of these energetic ions. Energetic ions can either stabilize or destabilize the plasma. Examples of such are the internal kink and the giant sawtooth modes. It is believed that the third adiabatic invariant is a stabilizing effect for the internal kink mode. Unfortunately, this stabilization can lead to giant sawteeth, even more violent internal kink modes. The single particle picture is an important physics that must be considered to understand the phenomenon of these instabilities.

Numerical studies of wave-particle interaction are challenging. Plasma as a whole consists of physics operating on varying orders of timescale such as collision, MHD, and particle transport to name a few. When we try to model such a system, we soon realize the difficulty in doing so. The hybrid kinetic-MHD model allows the particle physics to be evolved on the kinetic timescale of interest while evolving the MHD physics over the MHD timescale. This helps separate the physics, which means we can use a time step for the particle physics, for example a smaller, sub-cycled time step that pushes particles along their orbits, which is different from the timestep used in the MHD evolution.

In NIMROD, the hybrid kinetic-MHD approach is implemented in the form of  $\delta f$ -PIC and the  $\delta f$ -continuum. Both of these methods use the drift kinetic regime, where the characteristics of the equilibrium distribution function are given by guiding center motion. For both implementations, the energetic ions are coupled into the MHD equation via the energetic particle pressure tensor in the center of mass flow evolution equation. The main focus of this thesis was the  $\delta f$ -PIC. In the  $\delta f$ -PIC drift kinetic approach, the particles are pushed along the equilibrium fields.

Single particle motion was discussed in detail in Chapter 3. Understanding the physics behind the single particle picture and gyro-averaged guiding center motion is an important part of plasma physics since it plays a role in wave-particle interaction and particle transport. Numerical results for particle motion in equilibrium fields for an axisymmetric tokamak were provided. The analytical results were compared to the exact (up to numerical error) solutions that were obtained from the PIC simulation in NIMROD. These results showed decent agreement despite the assumptions made in the analytical formulation.

The Serendipity shape functions were introduced into the particle push in NIMROD's PIC algorithm. This was done in the hopes of obtaining higher accuracy in resolving the particle push, while still keeping the algorithm efficient. In Chapter 4, the results of the Serendipity functions compared to the 2D Lagrange polynomials implemented in NIMROD were compared. We saw that on average, the higher-order Serendipity sets were resolving the particle trajectories better than the bilinear case traditionally used in NIMROD's PIC routine. We also saw that the higher-order Serendipity sets had faster run time and less memory was used.

The load-balance scheme was also discussed and shown to help in cutting down runtime. In Chapter 5, a plot was shown of how the particles were distributed among the processors. The not load-balanced case was shown to have very uneven particle distribution among processors where the low pressure edge region had hardly any particles pushed by the processors operating there.

In Chapter 5, we also discussed the  $\delta f$ -PIC approach for the hybrid fluid/kinetic-PIC scheme. We formally presented the deposition process for which the energetic particle flow could be considered. Numerical results for NIMROD's PIC simulations were presented. Two PIC approaches were compared, one mentioned in [Kim \(2008\)](#) (which we called PiC) and the modified code with load-balancing capability with the Serendipity basis implementation (which we called newpart). We saw that both PiC and newpart gave similar results and that for both schemes the energetic ion population decreased the growth rates. It was unfortunate to see that the higher-order Serendipity basis seemed to have no effect on the

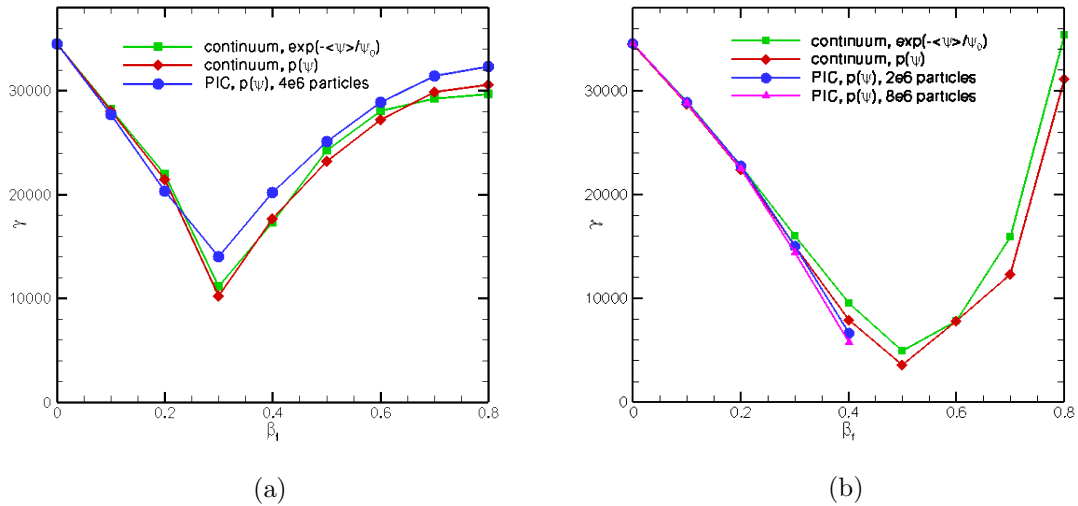


**Figure 6.1:** Figure (a) shows growth rates for NIMROD’s  $\delta f$ -continuum and  $\delta f$ -PIC approaches where  $E_{\text{crit}} = 50$  keV and  $E_{\text{inj}} = 80$  keV were used for the calculation. Figure (b) also shows growth rates for  $\delta f$ -continuum and  $\delta f$ -PIC approaches but with  $E_{\text{crit}} = 28$  keV and  $E_{\text{inj}} = 227$  keV. Need RF tail in NIMROD’s PIC routine to resolve the higher  $\beta$  cases.

growth rate for a core 1/1 internal kink mode.

In NIMROD’s PIC routines, the RF tail of the energetic particle population is not implemented, only the slowing down distribution part (see Fig. 5.2). Figure 6.1a shows the correct physics in terms of initial stabilization as  $\beta_{\text{frac}}$  is increased. But, the destabilization of the fishbone mode at higher  $\beta_{\text{frac}}$  is not correctly predicted. We are not sure why that is but both NIMROD’s PiC and newpart approaches show this incorrect trend at higher  $\beta_{\text{frac}}$ . This needs to be investigated further.

In Choi et al. (2007), the GATO code was used to show that at a window in  $\beta_{\text{frac}}$ , complete stabilization, *i.e.* no growth of an unstable mode, was observed. The goal was to do this with NIMROD as a linear, initial value problem solver; which is different from the GATO code which does an energy principle eigenmode analysis. Figure 6.1b shows that in going from  $E_{\text{inj}} = 80$  to 227 keV, an increased stabilization (lower growth rates) is observed and the trough moving toward  $\gamma = 0$ . It seems the high energy RF tail is needed in NIMROD’s  $\delta f$ -PIC. There are many improvements that can be made in the code and we list few of them here as potential future work.

- Optimize the existing algorithm for efficiency. By making the particle routines more efficient, this would greatly help in potential GPU implementation for subcycling. Subcycling will improve temporal accuracy in the trajectories.
- Adapt ACC compiler directives to push the particles off onto GPUs.
- Implement other projection techniques, such as the least squares approach, in the mapping between 2D Lagrange or non-uniformly spaced Gauss-Lobatto-Legendre bases and the Serendipity basis functions.
- Apply the Serendipity bases to the ion-orbit-loss problem. This was attempted but there were a few subtleties that needed to be considered and improved upon. One improvement is implementing the least squares approach in the mapping between bases.
- Implement the current coupling scheme and compare its predictions with the existing energetic particle pressure tensor scheme. Also, improve the existing pressure tensor scheme by incorporating a finite energetic particle flow, which was mentioned in the general deposition process in Chapter 5.
- Carry out the kink benchmark problem and compare with M3D-C1 ([Fu et al., 2006](#); [Liu et al., 2022b](#)) and NIMROD PiC ([Kim, 2008](#)).
- Implement a sampling of an energetic tail in the  $\delta f$ -PIC algorithm to handle extremely energetic ions driven by RF.
- Apply the  $\delta f$ -PIC to ITER simulations of  $\alpha$ -particles interacting with MHD. This would also require a different hybrid scheme than the one implemented since the  $\alpha$ -particle population is predicted to be significant in ITER.

## References

- Arnold, D. N. and Awanou, G. (2011). The serendipity family of finite elements. *Foundations of computational mathematics*, 11(3):337–344.
- Aydemir, A. Y. (1994). A unified monte carlo interpretation of particle simulations and applications to non-neutral plasmas. *Physics of Plasmas*, 1(4):822–831.
- Birdsall, C. K. and Langdon, A. B. (2018). *Plasma Physics via Computer Simulation*. CRC press.
- Boltzmann, L. (1970). *Weitere Studien über das Wärmegleichgewicht unter Gasmolekülen*, pages 115–225. Vieweg+Teubner Verlag, Wiesbaden.
- Brochard, G., Bao, J., Liu, C., Gorelenkov, N., Choi, G., Dong, G., Liu, P., Clenaghan, J. M., Nicolau, J., Wang, F., et al. (2022). Verification and validation of linear gyrokinetic and kinetic-mhd simulations for internal kink instability in diii-d tokamak. *Nuclear Fusion*, 62(3):036021.
- Cary, J. R. and Brizard, A. J. (2009). Hamiltonian theory of guiding-center motion. *Reviews of modern physics*, 81(2):693.
- Cheng, C. (1991). A kinetic-magnetohydrodynamic model for low-frequency phenomena. *Journal of Geophysical Research: Space Physics*, 96(A12):21159–21171.
- Cheng, C. and Johnson, J. R. (1999). A kinetic-fluid model. *Journal of Geophysical Research: Space Physics*, 104(A1):413–427.
- Chew, G., Goldberger, M., and Low, F. (1956). The boltzmann equation and the one-fluid hydromagnetic equations in the absence of particle collisions. *Proceedings of the Royal Society of London. Series A. Mathematical and Physical Sciences*, 236(1204):112–118.
- Choi, M., Turnbull, A., Chan, V., Chu, M., Lao, L., Jeon, Y., Li, G., Ren, Q., and Pinsker, R. (2007). Sawtooth control using beam ions accelerated by fast waves in the DIII-D tokamak. *Physics of Plasmas*, 14(11):112517.
- Floater, M. S. and Gillette, A. (2017). Nodal bases for the serendipity family of finite elements. *Foundations of Computational Mathematics*, 17(4):879–893.
- Freidberg, J. P. (2014). *Ideal MHD*. Cambridge University Press.
- Fu, G., Park, W., Strauss, H., Breslau, J., Chen, J., Jardin, S., and Sugiyama, L. (2006). Global hybrid simulations of energetic particle effects on the  $n=1$  mode in tokamaks: Internal kink and fishbone instability. *Physics of Plasmas*, 13(5):052517.
- Gurnett, D. A. and Bhattacharjee, A. (2017). *Introduction to Plasma Physics: With Space, Laboratory and Astrophysical Applications, Second Edition*. Cambridge University Press.
- Hammersley, J. M. and Handscomb, D. C. (1964). *Monte Carlo Methods*. Springer.

- Harris, S. (2004). *An Introduction to the Theory of the Boltzmann Equation*. Courier Corporation.
- Hazeltine, R. D. and Meiss, J. D. (2003). *Plasma Confinement*. Courier Corporation.
- Heidbrink, W., Fredrickson, E., Mau, T., Petty, C., Pinsker, R., Porkolab, M., and Rice, B. (1999). High harmonic ion cyclotron heating in diiii-d: Beam ion absorption and sawtooth stabilization. *Nuclear Fusion*, 39(10):1369.
- Heidbrink, W. and White, R. (2020). Mechanisms of energetic-particle transport in magnetically confined plasmas. *Physics of Plasmas*, 27(3):030901.
- Helander, P. and Sigmar, D. J. (2005). *Collisional Transport in Magnetized Plasmas*, volume 4. Cambridge university press.
- Held, E., Kruger, S., Ji, J.-Y., Belli, E., and Lyons, B. (2015). Verification of continuum drift kinetic equation solvers in nimrod. *Physics of Plasmas*, 22(3):032511.
- Hopf, C., Starnella, G., den Harder, N., and Fantz, U. (2021). Neutral beam injection for fusion reactors: technological constraints versus functional requirements. *Nuclear Fusion*, 61(10):106032.
- Karniadakis, G. E., Karniadakis, G., and Sherwin, S. (2005). *Spectral/hp Element Methods for Computational Fluid Dynamics*. Oxford University Press on Demand.
- Kim, C. C. (2008). Impact of velocity space distribution on hybrid kinetic-magnetohydrodynamic simulation of the (1,1) mode. *Physics of Plasmas*, 15(7):072507.
- Kim, C. C., Sovinec, C. R., Parker, S. E., Team, N., et al. (2004). Hybrid kinetic-mhd simulations in general geometry. *Computer physics communications*, 164(1-3):448–455.
- Landau, L. D. and Lifshitz, E. M. (1976). *Mechanics: Course of Theoretical Physics, Third Edition*, volume 1. Elsevier.
- Liu, C., Jardin, S. C., Bao, J., Gorelenkov, N., Brennan, D. P., Yang, J., and Podesta, M. (2022a). Thermal ion kinetic effects and landau damping in fishbone modes. *arXiv preprint arXiv:2206.03648*.
- Liu, C., Jardin, S. C., Qin, H., Xiao, J., Ferraro, N. M., and Breslau, J. (2022b). Hybrid simulation of energetic particles interacting with magnetohydrodynamics using a slow manifold algorithm and gpu acceleration. *Computer Physics Communications*, 275:108313.
- Luxon, J., Simonen, T., Stambaugh, R., and Team, D.-D. (2005). Overview of the diiii-d fusion science program. *Fusion Science and Technology*, 48(2):807–827.
- Luxon, J. L. (2002). A design retrospective of the diiii-d tokamak. *Nuclear Fusion*, 42(5):614.
- McQuarrie, D. A. (2000). *Statistical Mechanics*. Sterling Publishing Company.
- Ongena, J., Koch, R., Wolf, R., and Zohm, H. (2016). Magnetic-confinement fusion. *Nature Physics*, 12(5):398–410.



- Parker, S. and Lee, W. (1993). A fully nonlinear characteristic method for gyrokinetic simulation. *Physics of Fluids B: Plasma Physics*, 5(1):77–86.
- Putvinski, S. (1998). Physics of energetic particles in iter. *Nuclear fusion*, 38(9):1275.
- Sovinec, C., Glasser, A., Gianakon, T., Barnes, D., Nebel, R., Kruger, S., Schnack, D., Plimpton, S., Tarditi, A., Chu, M., et al. (2004). Nonlinear magnetohydrodynamics simulation using high-order finite elements. *Journal of Computational Physics*, 195(1):355–386.
- Stix, T. H. (1972). Heating of toroidal plasmas by neutral injection. *Plasma Physics*, 14(4):367.
- Stix, T. H. (1975). Fast-wave heating of a two-component plasma. *Nuclear Fusion*, 15(5):737.
- Tronci, C., Tassi, E., Camporeale, E., and Morrison, P. J. (2014). Hybrid vlasov-mhd models: Hamiltonian vs. non-hamiltonian. *Plasma Physics and Controlled Fusion*, 56(9):095008.
- White, R. B. (2013). *Theory Of Toroidally Confined Plasmas*. World Scientific Publishing Company.
- Zienkiewicz, O. C., Taylor, R. L., and Zhu, J. Z. (2005). *The Finite Element Method: Its Basis and Fundamentals*. Elsevier.

APPENDICES

## APPENDIX A

## The Dirac Delta Function in Curvilinear Coordinates

The Dirac delta function in Cylindrical coordinates was used when deriving the finite element coefficients of the energetic ion pressure tensor. The Dirac delta function was used for the point particle representation of the distribution function. Here we give a brief overview with few examples.

The Dirac delta function can be defined by the property

$$\int_{\mathcal{V}} f(\mathbf{x}) \delta^n(\mathbf{x} - \mathbf{x}') d^3x = \begin{cases} f(\mathbf{x}') & \text{if } \mathcal{P}(x', y', z') \text{ is in } \mathcal{V} \\ 0 & \text{if } \mathcal{P}(x', y', z') \text{ is not in } \mathcal{V} \end{cases}. \quad (\text{A.1})$$

There is no restriction on the number of dimensions involved and  $f(\mathbf{x})$  can be a scalar function or a vector function. However, the function  $f(\mathbf{x})$  must be defined at the point  $\mathcal{P}(x', y', z')$ . The Dirac delta function is normalized and the integral of it over the coordinates involved is unity.

Consider a three dimensional orthogonal curvilinear coordinate system with coordinates  $(\xi_1, \xi_2, \xi_3)$  and the scale factors

$$h_i = \sqrt{\left(\frac{\partial x}{\partial \xi_i}\right)^2 + \left(\frac{\partial y}{\partial \xi_i}\right)^2 + \left(\frac{\partial z}{\partial \xi_i}\right)^2}, \quad (\text{A.2})$$

then one can express the Dirac delta function  $\delta^3(\mathbf{x} - \mathbf{x}_0)$  as

$$\delta^3(\mathbf{x} - \mathbf{x}') \rightarrow \frac{\delta(\xi_1 - \xi_1')}{h_1} \frac{\delta(\xi_2 - \xi_2')}{h_2} \frac{\delta(\xi_3 - \xi_3')}{h_3}. \quad (\text{A.3})$$

In spherical coordinates we have:  $\xi_1 = r$ ,  $\xi_2 = \theta$ ,  $\xi_3 = \varphi$ , where the mapping between the Cartesian and the spherical coordinates are  $x = r \sin \theta \cos \varphi$ ,  $y = r \sin \theta \sin \varphi$ ,  $z = r \cos \theta$ . This mapping gives the scale factors  $h_1 = 1$ ,  $h_2 = r$ ,  $h_3 = r \sin \theta$ , which results in the

volume element  $d^3x = r^2 \sin \theta dr d\theta d\varphi$ . Therefore, the corresponding Dirac delta function is

$$\delta^3(\mathbf{x} - \mathbf{x}') = \frac{1}{r^2 \sin \theta} \delta(r - r') \delta(\theta - \theta') \delta(\varphi - \varphi') . \quad (\text{A.4})$$

If one considers azimuthal symmetry, then the  $\varphi$ -integral must be projected out

$$\int_0^{2\pi} r^2 \sin \theta d\varphi = 2\pi r^2 \sin \theta .$$

Therefore, the Dirac delta function becomes

$$\delta^3(\mathbf{x} - \mathbf{x}') = \frac{1}{2\pi r^2 \sin \theta} \delta(r - r') \delta(\theta - \theta') . \quad (\text{A.5})$$

If the problem involves further symmetry and now there is symmetry in both  $\theta$  and  $\varphi$ , we now must project out both of these coordinates

$$\int_0^\pi \int_0^{2\pi} r^2 \sin \theta d\varphi d\theta = 4\pi r^2 .$$

Thus giving the Dirac delta function

$$\delta^3(\mathbf{x} - \mathbf{x}') = \frac{1}{4\pi r^2} \delta(r - r') . \quad (\text{A.6})$$

Similarly, in cylindrical coordinate, were we have  $\xi_1 = \rho$ ,  $\xi_2 = \varphi$ ,  $\xi_3 = z$ . The mapping between the Cartesian and the cylindrical coordinates is accomplished by  $x = r \cos \varphi$ ,  $y = r \sin \varphi$ ,  $z = z$ . This gives the scale factors  $h_1 = 1$ ,  $h_2 = r$ ,  $h_3 = 1$ , which gives, for the volume element,  $d^3x = r dr d\theta dz$ . Therefore, the corresponding Dirac delta function in cylindrical coordinate is

$$\delta^3(\mathbf{x} - \mathbf{x}') = \frac{1}{r} \delta(r - r') \delta(\varphi - \varphi') \delta(z - z') . \quad (\text{A.7})$$

Similar to the spherical case, if we have symmetry in  $\varphi$  we get

$$\delta^3(\mathbf{x} - \mathbf{x}') = \frac{1}{2\pi r} \delta(r - r') \delta(z - z') . \quad (\text{A.8})$$

## APPENDIX B

### Particle in Magnetic Field: Non-canonical Variables

When using non-canonical variables, we need to find the symplectic form, which will then allow us to find the equations of motion in those variables (recall Eq. (2.25))

$$\frac{dz^\alpha}{dt} = \omega^{\alpha\beta} \left( \frac{\partial H}{\partial z^\beta} + \frac{\partial \mathcal{P}^i}{\partial t} \frac{\partial q_i}{\partial z^\beta} - \frac{\partial \mathcal{P}^i}{\partial z^\beta} \frac{\partial q_i}{\partial t} \right) .$$

Here we show the steps to obtain the equations of motion from the non-canonical formulation. First, we rewrite the Hamiltonian in terms of the non-canonical variables  $z^\alpha = (x^i, p^i)$  (see Eq. (2.13) ) to get

$$H(x^i, p^i, t) = \frac{1}{2m} p^i p_i + e\phi , \quad (\text{B.1})$$

where the expression for the canonical momentum (see Eq. (2.11)) was used. We now calculate the symplectic form (see Eq. (2.24)) by first considering the  $\alpha = i$  and  $\beta = j$  terms

$$\begin{aligned} \omega_{ij} &= \frac{\partial \mathcal{P}^k}{\partial z^i} \frac{\partial q_k}{\partial z^j} - \frac{\partial \mathcal{P}^k}{\partial z^j} \frac{\partial q_k}{\partial z^i} \\ &= \frac{\partial \mathcal{P}^k}{\partial x^i} \eta_{k\ell} \frac{\partial q^\ell}{\partial x^j} - \frac{\partial \mathcal{P}^k}{\partial x^j} \eta_{k\ell} \frac{\partial q^\ell}{\partial x^i} \\ &= e \frac{\partial A^k}{\partial x^i} \eta_{k\ell} \delta_j^\ell - e \frac{\partial A^k}{\partial x^j} \eta_{k\ell} \delta_i^\ell \\ &= e \left( \frac{\partial A_j}{\partial x^i} - \frac{\partial A_i}{\partial x^j} \right) \\ &= eF_{ij} , \end{aligned}$$

where note that  $A^k \eta_{k\ell} \delta_j^\ell = A^k \eta_{kj} = A_j$ . Now for the  $\alpha = i$  and  $\beta = j'$  terms, we perform similar calculation to get

$$\begin{aligned} \omega_{ij'} &= \frac{\partial \mathcal{P}^k}{\partial z^i} \frac{\partial q_k}{\partial z^{j'}} - \frac{\partial \mathcal{P}^k}{\partial z^{j'}} \frac{\partial q_k}{\partial z^i} \\ &= \frac{\partial \mathcal{P}^k}{\partial x^i} \eta_{k\ell} \frac{\partial q^\ell}{\partial p^{j'}} - \frac{\partial \mathcal{P}^k}{\partial p^{j'}} \eta_{k\ell} \frac{\partial q^\ell}{\partial x^i} \\ &= -\delta_j^k \eta_{k\ell} \delta_i^\ell \\ &= -\eta_{ij} . \end{aligned}$$

Next, for the  $\alpha = i'$  and  $\beta = j$  terms

$$\begin{aligned} \omega_{i'j} &= \frac{\partial \mathcal{P}^k}{\partial z^{i'}} \frac{\partial q_k}{\partial z^j} - \frac{\partial \mathcal{P}^k}{\partial z^j} \frac{\partial q_k}{\partial z^{i'}} \\ &= \frac{\partial \mathcal{P}^k}{\partial p^i} \eta_{k\ell} \frac{\partial q^\ell}{\partial x^j} - \frac{\partial \mathcal{P}^k}{\partial x^j} \eta_{k\ell} \frac{\partial q^\ell}{\partial p^i} \\ &= \eta_{ij} . \end{aligned}$$

Finally, for the  $\alpha = i'$  and  $\beta = j'$  terms

$$\begin{aligned} \omega_{i'j'} &= \frac{\partial \mathcal{P}^k}{\partial z^{i'}} \frac{\partial q_k}{\partial z^{j'}} - \frac{\partial \mathcal{P}^k}{\partial z^{j'}} \frac{\partial q_k}{\partial z^{i'}} \\ &= \frac{\partial \mathcal{P}^k}{\partial p^i} \eta_{k\ell} \frac{\partial q^\ell}{\partial p^{j'}} - \frac{\partial \mathcal{P}^k}{\partial p^{j'}} \eta_{k\ell} \frac{\partial q^\ell}{\partial p^i} \\ &= 0 . \end{aligned}$$

Therefore, the symplectic form comes out to be

$$\omega_{\alpha\beta} = \begin{pmatrix} eF_{ij} & -\eta_{ij} \\ \eta_{ij} & 0 \end{pmatrix} . \quad (\text{B.2})$$

We now calculate the  $\partial H/\partial z^\beta$  terms in Eq. (2.25), where for  $\beta = j$  we have

$$\begin{aligned}\frac{\partial H}{\partial z^j} &= \frac{\partial}{\partial x^j} \left( \frac{1}{2m} (\mathcal{P}^i - eA^i) (\mathcal{P}_i - eA_i) + e\phi \right) \\ &= \frac{\partial}{\partial x^j} \left( \frac{1}{2m} p^i p_i + e\phi \right) \\ &= e \frac{\partial \phi}{\partial x^j} .\end{aligned}$$

Note that the Hamiltonian was rewritten in terms of the independent variable  $p^i$ . Next, for the  $\beta = j'$  we have

$$\begin{aligned}\frac{\partial H}{\partial z^{j'}} &= \frac{\partial}{\partial p^{j'}} \left( \frac{1}{2m} (\mathcal{P}^i - eA^i) (\mathcal{P}_i - eA_i) + e\phi \right) \\ &= \frac{1}{2m} \left[ \left( \frac{\partial \mathcal{P}^i}{\partial p^{j'}} \right) (\mathcal{P}_i - eA_i) + (\mathcal{P}^i - eA^i) \left( \frac{\partial \mathcal{P}_i}{\partial p^{j'}} \right) \right] \\ &= \frac{1}{2m} \left[ \delta_j^i (\mathcal{P}_i - eA_i) + (\mathcal{P}^i - eA^i) (\eta_{i\ell} \delta_j^\ell) \right] \\ &= \frac{p_j}{m} ,\end{aligned}$$

where note that this gives the same result as the Hamilton's equation  $\partial H/\partial \mathcal{P}^i = \dot{q}^i$  since the new independent variable  $x^i$  is the same as the old one. The term  $\partial q_k/\partial t$  is simply

$$\frac{\partial q_k}{\partial t} = \eta_{k\ell} \frac{\partial x^\ell}{\partial t} = 0$$

since  $x^\ell$  is our non-canonical independent variable, and has no explicit time dependence.

The term  $\partial \mathcal{P}^k/\partial t$  also simply comes out to be

$$\frac{\partial \mathcal{P}^k}{\partial t} = \frac{\partial}{\partial t} (p^k + eA^k) = e \frac{\partial A^k}{\partial t} .$$

We will now consider only the  $\alpha = i'$  terms, which the equation of motion for the non-canonical variables comes from

$$\begin{aligned}
\frac{dz^{i'}}{dt} &= \omega^{i'\beta} \left( \frac{\partial H}{\partial z^\beta} + \frac{\partial \mathcal{P}^k}{\partial t} \frac{\partial q_k}{\partial z^\beta} - \frac{\partial \mathcal{P}^k}{\partial z^\beta} \frac{\partial q_k}{\partial t} \right) \\
\frac{dp^i}{dt} &= \omega^{i'j} \left( \frac{\partial H}{\partial z^j} + \frac{\partial \mathcal{P}^k}{\partial t} \frac{\partial q_k}{\partial z^j} - \frac{\partial \mathcal{P}^k}{\partial z^j} \frac{\partial q_k}{\partial t} \right) + \omega^{i'j'} \left( \frac{\partial H}{\partial z^{j'}} + \frac{\partial \mathcal{P}^k}{\partial t} \frac{\partial q_k}{\partial z^{j'}} - \frac{\partial \mathcal{P}^k}{\partial z^{j'}} \frac{\partial q_k}{\partial t} \right) \\
&= -\eta^{ij} \left( \frac{\partial H}{\partial x^j} + \frac{\partial \mathcal{P}^k}{\partial t} \frac{\partial q_k}{\partial x^j} - \frac{\partial \mathcal{P}^k}{\partial x^j} \frac{\partial q_k}{\partial t} \right) + eF^{ij} \left( \frac{\partial H}{\partial p^j} + \frac{\partial \mathcal{P}^k}{\partial t} \frac{\partial q_k}{\partial p^j} - \frac{\partial \mathcal{P}^k}{\partial p^j} \frac{\partial q_k}{\partial t} \right) \\
&= -\eta^{ij} \left( \frac{\partial H}{\partial x^j} + e \frac{\partial A^k}{\partial t} \frac{\partial q_k}{\partial x^j} \right) + eF^{ij} \left( \frac{\partial H}{\partial p^j} \right) \\
&= -\eta^{ij} \left( e \frac{\partial \phi}{\partial x^j} + e \frac{\partial A^k}{\partial t} \eta_{k\ell} \delta_j^\ell \right) + eF^{ij} \left( \frac{p_j}{m} \right) \\
&= e \left( -\eta^{ij} \frac{\partial \phi}{\partial x^j} - \eta^{ij} \frac{\partial A_j}{\partial t} \right) + e\varepsilon^{ijk} \dot{x}_j B_k \\
&= e \left( -\frac{\partial \phi}{\partial x_i} - \frac{\partial A^i}{\partial t} \right) + e\varepsilon^{ijk} \dot{x}_j B_k \\
&= e \left( E^i + \varepsilon^{ijk} \dot{x}_j B_k \right) ,
\end{aligned}$$

which gives the Lorentz force. Note that we used the Lorenz gauge

$$E^i = -\frac{\partial \phi}{\partial x_i} - \frac{\partial A^i}{\partial t} , \quad (\text{B.3})$$

where  $\partial/\partial x_i$  is the gradient in Cartesian coordinates. The gradient can also be expressed as

$$\nabla^i = \frac{\partial}{\partial x_i} = \eta^{ij} \partial_j , \quad (\text{B.4})$$

where the scale factors would be included for curvilinear coordinates similar to the vector components indicated by  $v^i = \eta^{ij} v_j$ . Note that  $v_j$  and  $\partial_j$  are contravariant components. Therefore, we get

$$\frac{dp^i}{dt} = e \left( E^i + \varepsilon^{ijk} \dot{x}_j B_k \right) \quad (\text{B.5})$$

or in vector form

$$\frac{d\mathbf{p}}{dt} = e (\mathbf{E} + \dot{\mathbf{x}} \times \mathbf{B}) . \quad (\text{B.6})$$



## APPENDIX C

## Derivation of Guiding Center Velocity

The guiding center velocity  $\dot{\mathbf{X}}$  is obtained by taking the total time derivative of the guiding center position  $\mathbf{X} = \mathbf{x} - \boldsymbol{\rho}$  (recall Eq. (3.8)), which comes out to be

$$\begin{aligned} \frac{d\mathbf{X}}{dt} &= \frac{d\mathbf{x}}{dt} + \frac{d}{dt} \left( \frac{\mathbf{v} \times \mathbf{b}}{\Omega} \right) \\ &= \mathbf{v} + \frac{d}{dt} \left( \frac{1}{\Omega} \right) \mathbf{v} \times \mathbf{b} + \frac{1}{\Omega} \frac{d\mathbf{v}}{dt} \times \mathbf{b} + \frac{1}{\Omega} \mathbf{v} \times \frac{d\mathbf{b}}{dt} . \end{aligned} \quad (\text{C.1})$$

We further expand the above expression, where the acceleration  $d\mathbf{v}/dt$  is expressed in terms of the Lorentz force and the total time derivative of the fields are expanded according to  $d/dt = \partial/\partial t + \mathbf{v} \cdot \nabla$ ; therefore, we get

$$\dot{\mathbf{X}} = \mathbf{v} - \frac{\dot{B}}{B} \frac{\mathbf{v} \times \mathbf{b}}{\Omega} + \frac{q}{m\Omega} \mathbf{E} \times \mathbf{b} + (\mathbf{v} \times \mathbf{B}) \times \mathbf{b} + \frac{1}{\Omega} \mathbf{v} \times \left( \frac{\partial \mathbf{b}}{\partial t} + \mathbf{v} \cdot \nabla \mathbf{b} \right) , \quad (\text{C.2})$$

where the time derivative of  $\Omega$  is  $\dot{\Omega}^{-1} = -\dot{B}/\Omega B$ . Now the above expression is gyro-averaged

$$\langle \dot{\mathbf{X}} \rangle = \langle \mathbf{v} \rangle - \left\langle \frac{\dot{B}}{B} \frac{\mathbf{v} \times \mathbf{b}}{\Omega} \right\rangle + \left\langle \frac{q}{m\Omega} \mathbf{E} \times \mathbf{b} \right\rangle + \left\langle (\mathbf{v} \times \mathbf{B}) \times \mathbf{b} \right\rangle + \left\langle \frac{1}{\Omega} \mathbf{v} \times \left( \frac{\partial \mathbf{b}}{\partial t} + \mathbf{v} \cdot \nabla \mathbf{b} \right) \right\rangle ,$$

which we expand out to get

$$\begin{aligned} \langle \dot{\mathbf{X}} \rangle &= \mathbf{v}_{\parallel} - \left\langle \frac{1}{B} \left( \frac{\partial B}{\partial t} + \mathbf{v} \cdot \nabla B \right) \frac{\mathbf{v} \times \mathbf{b}}{\Omega} \right\rangle + \frac{q}{m\Omega} \mathbf{E} \times \mathbf{b} \\ &\quad + \langle (\mathbf{v} \times \mathbf{B}) \times \mathbf{b} \rangle + \frac{1}{\Omega} \langle \mathbf{v} \rangle \times \frac{\partial \mathbf{b}}{\partial t} + \frac{1}{\Omega} \langle \mathbf{v} \times (\mathbf{v} \cdot \nabla \mathbf{b}) \rangle . \end{aligned} \quad (\text{C.3})$$

First, note that any term with  $\langle \mathbf{v} \rangle \times \mathbf{b} = \mathbf{v}_{\parallel} \times \mathbf{b} = 0$ , vanishes. Next, let us consider the third term above, which simplifies to

$$\langle (\mathbf{v} \cdot \nabla B) \mathbf{v} \times \mathbf{b} \rangle = \langle (\nabla B) \cdot \mathbf{v} \mathbf{v} \times \mathbf{b} \rangle = \nabla B \cdot \langle \mathbf{v} \mathbf{v} \rangle \times \mathbf{b} , \quad (\text{C.4})$$

where one can show  $\langle \mathbf{v}\mathbf{v} \rangle = v_{\parallel}^2 \mathbf{b}\mathbf{b} + \frac{1}{2}v_{\perp}^2 (1 - \mathbf{b}\mathbf{b})$ , which allows us to further simplify

$$\begin{aligned} \nabla B \cdot \langle \mathbf{v}\mathbf{v} \rangle \times \mathbf{b} &= \nabla B \cdot \left( v_{\parallel}^2 \mathbf{b}\mathbf{b} + \frac{1}{2}v_{\perp}^2 (1 - \mathbf{b}\mathbf{b}) \right) \times \mathbf{b} \\ &= \frac{v_{\perp}^2}{2} \nabla B \cdot \mathbf{l} \times \mathbf{b} \\ &= -\frac{v_{\perp}^2}{2} \mathbf{b} \times \nabla B . \end{aligned} \quad (\text{C.5})$$

Hence, we have the magnetic gradient drift from the third term. The other term that needs careful consideration is the last term, which when expanded yields

$$\langle \mathbf{v} \times (\mathbf{v}) \cdot \nabla \mathbf{b} \rangle = v_{\parallel}^2 \mathbf{b} \times (\mathbf{b} \cdot \nabla \mathbf{b}) + \frac{1}{2}v_{\perp}^2 (\mathbf{e}_{\alpha} \times (\mathbf{e}_{\alpha} \cdot \nabla \mathbf{b}) - \mathbf{b} \times (\mathbf{b} \cdot \nabla \mathbf{b})) . \quad (\text{C.6})$$

We used the relation

$$\langle \mathbf{v} \star \mathbf{v} \rangle = v_{\parallel}^2 \mathbf{b} \star \mathbf{b} + \frac{1}{2}v_{\perp}^2 (\mathbf{e}_{\alpha} \star \mathbf{e}_{\alpha} - \mathbf{b} \star \mathbf{b}) , \quad (\text{C.7})$$

where  $\star$  indicate any vector multiplication, *i.e.* dot, cross, or outer product. Note that summation is implied for repeating indices. We can further simplify this term by considering the following

$$\mathbf{e}_{\alpha} \times (\mathbf{e}_{\alpha} \cdot \nabla \mathbf{b}) = \mathbf{e}_{\alpha} \times (\partial_{\alpha} \mathbf{b}) = \nabla \times \mathbf{b} = \frac{\mu_0 \mathbf{J}}{B} , \quad (\text{C.8})$$

where the pre-Maxwell form of Ampere's law was used for the last expression. We also note that the magnetic curvature vector has the form

$$\boldsymbol{\kappa} = -\mathbf{b} \times (\nabla \times \mathbf{b}) = \mathbf{b} \cdot \nabla \mathbf{b} . \quad (\text{C.9})$$

Therefore, combining these results we get for the last expression of the guiding center velocity

$$\begin{aligned}
\langle \mathbf{v} \times (\mathbf{v} \cdot \nabla \mathbf{b}) \rangle &= v_{\parallel}^2 \mathbf{b} \times (\mathbf{b} \cdot \nabla \mathbf{b}) + \frac{1}{2} v_{\perp}^2 \left( \frac{\mu_0 \mathbf{J}}{B} + \mathbf{b} \times (\mathbf{b} \times (\nabla \times \mathbf{b})) \right) \\
&= v_{\parallel}^2 \mathbf{b} \times \boldsymbol{\kappa} + \frac{1}{2} v_{\perp}^2 \left( \frac{\mu_0 \mathbf{J}}{B} + \mathbf{b} \times \left( \mathbf{b} \times \left( \frac{\mu_0 \mathbf{J}}{B} \right) \right) \right) \\
&= v_{\parallel}^2 \mathbf{b} \times \boldsymbol{\kappa} + \frac{\mu_0 v_{\perp}^2}{2B} (\mathbf{J} - \mathbf{J}_{\perp}) \\
&= v_{\parallel}^2 \mathbf{b} \times \boldsymbol{\kappa} + \frac{\mu_0 v_{\perp}^2}{2B} \mathbf{J}_{\parallel}, \tag{C.10}
\end{aligned}$$

where for any vector  $\mathbf{b} \times (\mathbf{b} \times \mathbf{A}) = A_{\parallel} \mathbf{b} - \mathbf{A} = -\mathbf{A}_{\perp}$ . Plugging these back into the guiding center velocity gives the final result

$$\langle \dot{\mathbf{X}} \rangle = v_{\parallel} \mathbf{b} + \frac{\mathbf{E} \times \mathbf{B}}{B^2} + \frac{1}{\Omega} \mathbf{b} \times \left( v_{\parallel} \frac{\partial \mathbf{b}}{\partial t} + v_{\parallel}^2 \boldsymbol{\kappa} + \frac{v_{\perp}^2}{2} \frac{\nabla B}{B} \right) + \frac{\mu_0 \mu}{qB} \mathbf{J}_{\parallel}. \tag{C.11}$$

## APPENDIX D

### Trapped/Passing Particle: Orbit Period

The integral for the particle orbit period (recall Eq. (3.66)) is carefully considered here. Both the passing and the trapped particle results are derived. We present the integral here for convenience

$$\tau_b = \frac{q_s R}{v \sqrt{2\epsilon\lambda}} \oint \frac{d\theta}{\sigma \sqrt{k^2 - \sin^2(\theta/2)}}. \tag{D.1}$$

First, we consider the passing particle, where  $k > 1$ ; thus, the quantity in the square root is always positive, which gives us a real value for the integral. Since a passing particle never bounces,  $\sigma$  does not change sign (here we use  $\sigma = 1$ ). For a passing particle, we need to integrate from  $-\pi$  to  $\pi$ . After some simplification we get the expression

$$\tau_b = \frac{2q_s R}{v \sqrt{2\epsilon\lambda}} \int_0^{\pi} \frac{d\theta}{k \sqrt{1 - k^{-2} \sin^2(\theta/2)}} = \frac{4q_s R}{v \sqrt{2\epsilon\lambda}} \frac{1}{k} \int_0^{\pi/2} \frac{dy}{\sqrt{1 - k^{-2} \sin^2 y}},$$

where  $y = \theta/2$ . Note that the integral in the last expression is an elliptic integral that is defined on the interval  $0 \leq x < \pi/2$

$$K(k) = \int_0^{\pi/2} \frac{dx}{\sqrt{1 - k^2 \sin^2 x}}. \quad (\text{D.2})$$

Thus, for a passing particle, the period of one orbit comes out to be

$$\tau_b = \frac{4q_s R}{v\sqrt{2\epsilon\lambda}} \frac{K(k^{-1})}{k}. \quad (\text{D.3})$$

Now for the trapped particle where  $0 < k < 1$ , we have  $\lambda \sim 1$  due to the trapped condition (see Eq. (3.48)). For the trapped particle, the parallel velocity changes sign. When the particle trajectory is integrated along  $+d\theta$  we have  $+\sigma$  and once the particle bounces we now integrate along  $-d\theta$  where  $-\sigma$ ; thus breaking up the integral into two parts gives

$$\begin{aligned} \tau_b &= \frac{q_s R}{v\sqrt{2\epsilon}} \left[ \int_{-\theta_b}^{\theta_b} \frac{d\theta}{\sigma\sqrt{k^2 - \sin^2(\theta/2)}} + \int_{-\theta_b}^{\theta_b} \frac{-d\theta}{-\sigma\sqrt{k^2 - \sin^2(\theta/2)}} \right] \\ &= \frac{2q_s R}{v\sqrt{2\epsilon}} \int_{-\theta_b}^{\theta_b} \frac{d\theta}{\sqrt{k^2 - \sin^2(\theta/2)}}. \end{aligned}$$

The trapped particle case is similar to the pendulum system with large angle, where small angle approximation cannot be used, *i.e.* we cannot use  $\sin \theta \approx \theta$ . In the pendulum case  $k = \sin(\theta_{\max}/2)$ , where  $\theta_{\max}$  is the maximum angle the pendulum reaches. Therefore, for the trapped particle case, this maximum angle is the bounce angle  $\theta_b$ , hence  $k = \sin(\theta_b/2)$ . Note that, from the last integral expression above, the term in the square root is not negative since  $k < 1$ ; like before, we will express the integral for trapped particles in terms of elliptic integrals. Let  $k \sin x = \sin y$  (which means  $k \cos x dx = \cos y dy$ ), where  $y = \theta/2$  like before. Using these new variables we get for the above integral

$$I = \int_{-\theta_b}^{\theta_b} \frac{d\theta}{\sqrt{k^2 - \sin^2(\theta/2)}} = 2 \int_0^{\theta_b} \frac{d\theta}{\sqrt{k^2 - \sin^2(\theta/2)}} = 4 \int_0^{\theta_b/2} \frac{dy}{\sqrt{k^2 - \sin^2(y)}},$$

which further simplifies to

$$I = 4 \int_0^{\theta_b/2} \frac{dy}{k \sqrt{1 - k^{-2} \sin^2(y)}} = 4 \int_0^{\theta_b/2} \frac{(k \cos x / \cos y) dx}{k \sqrt{1 - \sin^2 x}} = 4 \int_0^{\theta_b/2} \frac{(\cos x / \cos y) dx}{\sqrt{1 - \sin^2 x}} .$$

Note that since for trapped particles  $k = \sin(\theta_b/2)$ , the limits of integration in the new variable becomes

$$\sin x = k^{-1} \sin(\theta_b/2) = 1 \quad \implies \quad x = \sin^{-1}(1) = \frac{\pi}{2} .$$

Using the identity  $\cos \alpha = \sqrt{1 - \sin^2 \alpha}$  and the new limits of integration gives

$$I = 4 \int_0^{\pi/2} \frac{dx}{\sqrt{1 - \sin^2 y}} = 4 \int_0^{\pi/2} \frac{dx}{\sqrt{1 - k^2 \sin^2 x}} ,$$

where for the last term  $k \sin x = \sin y$  was used. Now that we have the elliptic integral for the passing case, we get the final expression

$$\tau_b = \frac{8q_s R}{v \sqrt{2\epsilon}} \int_0^{\pi/2} \frac{dx}{\sqrt{1 - k^2 \sin^2 x}} = \frac{8q_s R}{v \sqrt{2\epsilon}} K(k) . \quad (\text{D.4})$$

## APPENDIX E

### Serendipity Shape Functions

The explicit forms for the complete Serendipity shape functions used for computation are given here. Serendipity shape functions up to third-order can be found in textbooks, *e.g.* [Zienkiewicz et al. \(2005\)](#), while the fourth-order is harder to find. The reduced (incomplete) Serendipity shape functions are not given here, but can be easily built using the method given in Chapter 4.

**Bilinear Shape Functions**

$$\begin{aligned}
S_1^1 &= \frac{1}{4} (1 - \xi) (1 - \eta) & S_2^1 &= \frac{1}{4} (1 + \xi) (1 - \eta) \\
S_3^1 &= \frac{1}{4} (1 + \xi) (1 + \eta) & S_4^1 &= \frac{1}{4} (1 - \xi) (1 + \eta)
\end{aligned}$$

**Biquadratic Shape Functions**

$$\begin{aligned}
S_1^2 &= -\frac{1}{4} (1 - \xi) (1 - \eta) (1 + \xi + \eta) & S_2^2 &= -\frac{1}{4} (1 + \xi) (1 - \eta) (1 - \xi + \eta) \\
S_3^2 &= -\frac{1}{4} (1 + \xi) (1 + \eta) (1 - \xi - \eta) & S_4^2 &= -\frac{1}{4} (1 - \xi) (1 + \eta) (1 + \xi - \eta) \\
S_5^2 &= \frac{1}{2} (1 - \xi^2) (1 - \eta) & S_6^2 &= \frac{1}{2} (1 + \xi) (1 - \eta^2) \\
S_7^2 &= \frac{1}{2} (1 - \xi^2) (1 + \eta) & S_8^2 &= \frac{1}{2} (1 - \xi) (1 - \eta^2)
\end{aligned}$$

**Bicubic Shape Functions**

$$\begin{aligned}
S_1^3 &= \frac{1}{32} (1 - \xi) (1 - \eta) [9 (\xi^2 + \eta^2) - 10] & S_2^3 &= \frac{1}{32} (1 + \xi) (1 - \eta) [9 (\xi^2 + \eta^2) - 10] \\
S_3^3 &= \frac{1}{32} (1 + \xi) (1 + \eta) [9 (\xi^2 + \eta^2) - 10] & S_4^3 &= \frac{1}{32} (1 - \xi) (1 + \eta) [9 (\xi^2 + \eta^2) - 10] \\
S_5^3 &= \frac{9}{32} (1 - 3\xi) (1 - \xi^2) (1 - \eta) & S_6^3 &= \frac{9}{32} (1 + 3\xi) (1 - \xi^2) (1 - \eta) \\
S_7^3 &= \frac{9}{32} (1 + \xi) (1 - 3\eta) (1 - \eta^2) & S_8^3 &= \frac{9}{32} (1 + \xi) (1 + 3\eta) (1 - \eta^2) \\
S_9^3 &= \frac{9}{32} (1 + 3\xi) (1 - \xi^2) (1 + \eta) & S_{10}^3 &= \frac{9}{32} (1 - 3\xi) (1 - \xi^2) (1 + \eta) \\
S_{11}^3 &= \frac{9}{32} (1 - \xi) (1 + 3\eta) (1 - \eta^2) & S_{12}^3 &= \frac{9}{32} (1 - \xi) (1 - 3\eta) (1 - \eta^2)
\end{aligned}$$

### Biquartic Shape Functions

$$\begin{aligned}
S_1^4 &= -\frac{1}{12} (1 - \xi) (1 - \eta) (4\xi^3 + 4\eta^3 - 3\xi\eta - 4\xi - 4\eta) \\
S_2^4 &= \frac{1}{12} (1 + \xi) (1 - \eta) (4\xi^3 - 4\eta^3 - 3\xi\eta - 4\xi + 4\eta) \\
S_3^4 &= \frac{1}{12} (1 + \xi) (1 + \eta) (4\xi^3 + 4\eta^3 + 3\xi\eta - 4\xi - 4\eta) \\
S_4^4 &= -\frac{1}{12} (1 - \xi) (1 + \eta) (4\xi^3 - 4\eta^3 + 3\xi\eta - 4\xi + 4\eta) \\
S_5^4 &= -\frac{2}{3} \xi (1 - 2\xi) (1 - \xi^2) (1 - \eta) & S_6^4 &= -\frac{1}{2} (1 + \xi) (1 - \xi) (1 - \eta) (4\xi^2 + \eta) \\
S_7^4 &= \frac{2}{3} \xi (1 + 2\xi) (1 - \xi^2) (1 - \eta) & S_8^4 &= -\frac{2}{3} (1 + \xi) \eta (1 - 2\eta) (1 - \eta^2) \\
S_9^4 &= -\frac{1}{2} (1 + \xi) (1 + \eta) (1 - \eta) (4\eta^2 - \xi) & S_{10}^4 &= \frac{2}{3} (1 + \xi) \eta (1 + 2\eta) (1 - \eta^2) \\
S_{11}^4 &= \frac{2}{3} \xi (1 + 2\xi) (1 - \xi^2) (1 + \eta) & S_{12}^4 &= -\frac{1}{2} (1 + \xi) (1 - \xi) (1 + \eta) (4\xi^2 - \eta) \\
S_{13}^4 &= -\frac{2}{3} \xi (1 - 2\xi) (1 - \xi^2) (1 + \eta) & S_{14}^4 &= \frac{2}{3} (1 - \xi) \eta (1 + 2\eta) (1 - \eta^2) \\
S_{15}^4 &= -\frac{1}{2} (1 - \xi) (1 + \eta) (1 - \eta) (4\eta^2 + \xi) & S_{16}^4 &= -\frac{2}{3} (1 - \xi) \eta (1 - 2\eta) (1 - \eta^2) \\
S_{17}^4 &= (1 - \xi^2) (1 - \eta^2)
\end{aligned}$$

CURRICULUM VITAE



# Trevor V. Taylor

1300 E 1600 N – North Logan, 84341 – Utah

☎ (435) 265-8880 • ✉ vincent.taylor77@yahoo.com

Doctoral candidate studying theoretical and computational plasma physics with a passion for science and learning. A strong desire to advance the world's understanding of plasma physics. Adept at tackling complicated problems and solving them. Excellent cross-cultural communication skills developed through life-long experience living in different cultures and languages.

## Education

---

### Doctor of Philosophy in Physics

Utah State University, Logan, Utah

October 2022

### Bachelor of Science in Physics

University of Utah, Salt Lake City, Utah

May 2016

### Associate of Science in Engineering

Snow College, Ephraim, Utah

May 2012

## Research Experience

---

### Graduate Research Assistant: Theoretical/Computational Plasma Physics

Department of Physics, Utah State University

Sep 2016 - Present

Advisor: Eric D. Held, Ph.D

- Numerical modeling of energetic particles in tokamak plasmas
- Expanded NIMROD's Finite Element and PIC methods for plasma physics modeling
- Run-time and data storage optimization of PIC algorithm for energetic particle modeling

### Undergraduate Research Assistant: Experimental Condensed Matter Physics

Department of Physics, University of Utah

May 2015 - May 2016

Supervisor: Shanti Deemyad, Ph.D

- Constructed optical path for spectroscopy using an Argon-ion laser
- Investigated the effects of extreme conditions of pressure and temperature on simple matter
- Analyzed diffraction data of Lithium isotopes to understand their response to extreme conditions

### Undergraduate Research Assistant: Theoretical Condensed Matter Physics

Department of Physics, University of Utah

Oct 2014 - May 2015

Supervisor: Dmytro Pesin, Ph.D

- Investigated transport in quantum systems using both analytical and numerical approaches

### Visiting Undergraduate Research Assistant

Material Science and Applied Physics Lab, Tsukuba University, Japan

May 2013 - Aug 2013

Supervisor: Kazuo Kadowaki, Sc.D

- Manufactured superconductors and topological insulators for testing and investigation
- Tested resistivity and Quantum Hall effect in topological insulators

## Teaching Experience

---

### Graduate Teaching Assistant

Department of Physics, Utah State University

Sep 2016 - Present

- Taught undergraduate classical mechanics, electrodynamics, quantum mechanics, and more
- Primary instructor for physics labs

### Undergraduate Teaching Assistant

Department of Physics, University of Utah

Sep 2014 - May 2016

- Taught and tutored students in introductory physics courses
- Primary instructor for physics labs

## Technical Skills

---

- **Programming:** FORTRAN 90, Python, MPI, SVN, Linux
- **Scientific Computing:** NIMROD, Maple, Tecplot, Mathematica, massively parallel computing architectures
- **Others:** L<sup>A</sup>T<sub>E</sub>X, LYX, Microsoft Office

## Languages

---

- **English:** Native
- **Japanese:** Native
- **Thai:** Conversational

## Honors

---

### Blood Taylor Scholarship

*Department of Physics, Utah State University*  
An endowed scholarship for academic merit

May 2021

### Farrell and Ann Edwards Endowment

*Department of Physics, Utah State University*  
Strong commitment to research and teaching in physics

Dec 2017

### Outstanding Teaching Assistant Scholarship

*Department of Physics, University of Utah*  
An endowment for excellence in teaching

Apr 2015

## Paper, Talks, and Posters

---

### Serendipity Shape Functions in NIMROD's $\delta f$ -PIC Approach to Energetic Particle Physics

*Talk/Poster: Sherwood Conference in Santa Rose, CA*  
Trevor V. Taylor and Eric D. Held, and J. Andrew Spencer

Apr 2022

### Update on serendipity shape functions in NIMROD's $\delta f$ PIC

*Talk/Poster: APS-DPP Conference in Fort Lauderdale, FL*  
Trevor V. Taylor and Eric D. Held, J. Andrew Spencer, and S.E. Kruger

Oct 2019

### Serendipity shape functions in NIMROD's $\delta f$ PIC approach

*Talk: NIMROD team meeting in Madison, WI*  
Trevor V. Taylor and Eric D. Held, J. Andrew Spencer, and S.E. Kruger

Aug 2019

### Higher-order shape functions for $\delta f$ PIC in NIMROD

*Talk/Poster: Sherwood Conference in Princeton, NJ*  
Trevor V. Taylor and Eric D. Held, J. Andrew Spencer, and S.E. Kruger

Apr 2019

### What are Monte Carlo Methods and How to Utilize Them?

*Talk/Report: Candidacy presentation at Utah State University, UT*  
Trevor V. Taylor

Mar 2019

### A comparison of NIMROD's continuum and $\delta f$ PIC approach to energetic particle physics

*Poster: APS-DPP Conference in Portland, OR*  
Trevor V. Taylor and Eric D. Held

Nov 2018

### Linearized drift kinetic equations in NIMROD

*Poster: Sherwood Conference in Auburn, AL*  
E.D. Held, J. Andrew Spencer, Trevor V. Taylor, and D.B. Hansen

Apr 2018

### Deuterium Isotope Effects in Polymerization of Benzene under Pressure

*Paper: The Journal of Physical Chemistry Letter*  
Weizhao Cai, Mihindra Dunuwille, Jiangang He, Trevor V. Taylor, Jasmine K. Hinton, Mary C. MacLean, Jamie J. Molaison, Antonio M. Dos Santos, Stanislav Sinogeikin, and Shanti Deemyad. J. Phys. Chem. Lett. 2017, 8, 1856-1864

## Personal Interests

---

Cooking, kayaking, paddle boarding, playing piano, rock climbing, swimming, weight training

## References

---

**Eric D. Held, Ph.D**

*Professor, Department of Physics, Utah State University*  
(435) 797-7166, eric.held@usu.edu

**Oscar Varela, Ph.D**

*Assistant Professor, Department of Physics, Utah State University*  
(435) 797-8425, oscar.varela@usu.edu

**Jeong-Young Ji, Ph.D**

*Research Professor, Department of Physics, Utah State University, USA*  
(435) 797-8118, j.ji@usu.edu

**Andrew Spencer, Ph.D**

*Research Scientist, Department of Physics, Utah State University*  
andy.spencer@usu.edu